# Intelligent Battery Management System for Electric Vehicles

**YAN Jingyu**

A Thesis Submitted in Partial Fulfilment
of the Requirements for the Degree of
Doctor of Philosophy
in
Mechanical and Automation Engineering

The Chinese University of Hong Kong
September 2010





ProQuest LLC.
789 East Eisenhower Parkway
P.O. Box 1346
Ann Arbor, MI 48106 - 1346

Thesis /Assessment Committee

Professor Wei-Hsin Liao (Chair)

Professor Yangsheng Xu (Thesis Supervisor)

Professor Changling Wang (Committee Member)

Professor Lilong Cai (External Examiner)

論文評審委員會

廖維新教授（主席）

徐揚生教授（論文導師）

王昌凌教授（委員）

蔡李隆教授（校外委員）

# Abstract

The automotive industry has experienced a significant boom in recent years, accelerating the problems of energy shortage and environmental disruption around the world. To solve the two problems, electric vehicles (EVs), including battery electric vehicles (BEV), hybrid electric vehicles (HEV), and fuel-cell electric vehicles (FEV), have been proposed and studied in recent years. Despite the efforts devoted to the development of EVs by both the scientific research and industrial communities, there are still many obstacles hindering the mass commercialization of EVs. Among these obstacles, the battery system, the new energy storage component in EVs, is one of the most important yet most difficult parts of EV design, and the battery management system (BMS) is recognized as the single most important technical issue in the successful commercialization of EVs.

A vehicular battery must consist of a large number of cells to provide the necessary energy and power. Management only at the level of the battery pack causes out-of-investigation cells and lack of cell equalization ability. Therefore, in the smart module concept, cells are first grouped into modules, which are then connected to the battery pack. Each module is an independent unit with a controller to investigate and control cells. Based on this

concept, the work in this thesis redistributes tasks among module controllers and a central controller, applies a self-power design to enhance module independence, and selects the newly developed automotive ICs and sensors. Finally, a prototype of the BMS has been developed and successfully applied in a series of HEVs.

State of charge (SoC) is a battery state indicating its residual capacity. It is the fundamental state of the battery and is the basis for other battery operations. However, SoC is not a directly measurable state and has to be obtained by estimation techniques. Aiming to enhance the anti-noise ability of SoC estimation in a real vehicle environment, we propose a SoC estimation framework consisting of an adaptive nonlinear diffusion filter to reduce the noise of current measurement, a self-learning mechanism to remove its zero-drift, an open loop coulomb counting estimator and a model based closed loop filter to estimate SoC, and a data fusion unit to reach the final estimation result. In a simulation study, the closed loop filter is implemented based on an RC model and $H_\infty$ filter. In experiments and application, we modify the enhanced self-correcting model to model a type of LiFePO4 battery and apply an extended Kalman filter to estimate SoC. The framework has been demonstrated to improve accuracy and anti-noise ability, and achieves the technique upgrading goal recently published by the Chinese government.

Cell equalization is a crucial technique to balance the cells inside a battery pack, with the ability to maximize pack capacity and protect cells from damage. For the bi-directional Cuk equalizing circuit, we propose a SoC based, instead of voltage based, fuzzy controller to intelligently determine the equalizing current, with the aim of reducing equalizing duration, enhanc-

ing equalizing efficiency, and protecting cells. The inputs to the controller are specially designed as the difference in SoC, the average SoC, and the total internal resistance. Because of the lack of theoretical analysis on equalizing current in the electrochemistry field, we utilize a fuzzy controller to incorporate the experience and knowledge of experts. Simulations and experiments verify its availability and efficacy. Especially for a LiFePO4 battery, a large SoC difference may lead to only a small difference in voltage and cause the failure of a traditional voltage based equalizer. The SoC based method successfully avoids this problem and obtains good performance in equalizing LiFePO4 cells.

Fast charge is intended to charge a battery as fast as possible, without any damage and with high energy efficiency, thus helping to reduce vehicle out-of-service time and promote the commercialization of EVs. Battery safety and charging efficiency are partially reflected by the increase in temperature during the charging process. Therefore, the aims of this thesis were to accelerate charging speed and reduce the temperature increase. We introduce a model predictive control framework to control the charging process. An RC model and the modified enhanced self-correcting model are employed to predict the future SoC in simulations and experiments respectively. A single-node lumped-parameter thermal model and a neural network trained by real experimental data are also applied respectively. In addition, a genetic algorithm is applied to optimize the charging current under multiple objectives and constraints. Simulation and experimental results strongly demonstrate that the Pareto front of the proposed algorithm dominates that of the popular constant current constant voltage charge method.

# 論文摘要

汽車工業在最近幾十年得到了迅速的發展，然而，也加速了全球性的能源危機和環境惡化。近年來，為了能夠同時解決這兩個問題，電動汽車，包括純電動汽車、混合動力汽車和燃料電池汽車，作為新一代交通工具得到了大規模的研發。盡管科技界和產業界均投入了大量的努力，但目前仍然存在不少障礙，阻礙了電動汽車的大規模商品化。其中，電動汽車的新增儲能系統，即電池系統，是電動汽車研發中最重要也最困難的零部件之一。電池管理系統甚至被認為是電動汽車成功商業化過程中最為重要的單個技術。

為了提供足夠的能量和功率，車載電池包必須由大量的電池單體構成。對電池包整體進行管理，不能對單體進行監測和均衡。因此，在智能模塊概念中，首先由單體構成模塊，然後再將模塊連接成電池包。每個模塊是一個完全獨立的單元並采用一個微處理器對模塊內的單體進行監測和控制。基於此概念，本文重新定義了模塊控制器和中央控制的任務分配，采用模塊自供電設計增強了模塊的獨立性，並選用了新型的電動汽車專用芯片和傳感器，最終開發出一款電池管理系統，並成功地應用於一輛串聯式混合動力汽車。

荷電狀態是衡量電池剩余能量的指標，它是電池中最基本的狀態，為其它電池的操作和管理提供了根據。然而，荷電狀態是一個不可直接測量的量，必須采用估計手段來獲取。為提高在實際車輛行駛環境中核電狀態估計的抗幹擾能力，本文提出了一個荷電狀態估計框架，包含一個自適應非線性擴散濾波器以降低電流測量噪聲，一個自學習機制以去除電流測量的零點漂移，一個開環電流積分估計器以及一個基於模型的闭環估計器分別對荷電狀態進行估計，最後再利用一個數據融合單元，對上述兩個結果

進行融合。在仿真實驗中，闭環估計器基於RC模型和$H_\infty$濾波器進行了實現。在實際應用中，本文修改了增強型自校正模型，對一款磷酸鐵鋰電池進行了建模，並采用擴展卡爾曼濾波器對荷電狀態進行闭環估計。仿真、實驗和實際應用結果表明，本文提出的算法能有效提高荷電狀態估計的抗幹擾能力，達到了中國最近頒布的技術進步目標。

單體均衡是平衡電池包內各個單體核電狀態的技術，有助於最大化電池包容量，並防止單體濫用。基於Cuk均衡電路，本文提出了一種基於荷電狀態，而非電池端電壓，的模糊控制器來自動控制均衡電流的大小。控制的輸入設計為荷電狀態差、平均荷電狀態和總內阻，分別代表了單體的不均衡性，平均放電能力和內阻損耗。因均衡問題缺乏電化學的理論研究，我們採用模糊控制器來實現專家的經驗和知識，建立隸屬度函數和知識庫。仿真和實驗結果都證明了本文提出方法的有效性和實用性。尤其是對於磷酸鐵鋰電池，由於其荷電狀態與開環電壓的曲線十分平坦，不均衡性往往僅導致微小的電壓差，使得基於電壓的均衡方法無法工作。基於荷電狀態的方法能有效避免此問題，在磷酸鐵鋰電池上獲得了良好的實際均衡效果。

快速充電是指對電池不造成損害的同時，快速地、高效地對電池進行充電。它有助於減少充電時間，并推廣電動汽車的商業化。電池的安全性和充電效率可部分地體現為充電過程中的發熱，因此，本文以減少充電時間和降低溫度上升為目標，採用模型預測控制的框架對充電過程進行控制。對核電狀態的預測，在仿真和實驗中分別采用RC模型和修改後的增強型自校正模型；對溫度的預測，分別采用單節點集中參數熱學模型和神經網絡模型。在提出的性能指标下，採用遺傳算法對未來的充電序列進行優化。仿真和實驗均證明，基於模型預測控制所得到的帕累托前沿主導目前所常采用的恒流恒壓充電。

# Acknowledgement

This thesis has been accomplished with a lot of help, suggestions and support from others. In these acknowledgements, I express my gratitude to those who have had the most profound influence on this thesis and without whom the thesis would have been impossible to finish.

Firstly, I thank my advisor Prof. Yangsheng Xu, who led me to research in the electric vehicle field, especially focusing on battery management systems. His rigorous academic attitude has affected me deeply and his wise comments always set me on the right track. Without his enthusiastic and enlightening advice and guidance, I would never have been able to complete this thesis. It is impossible to express sufficient gratitude to him.

I would like to thank Prof. Guoqing Xu. He has provided many suggestions and pointed out the potential problems during my Ph.D study. His intensive knowledge of vehicle engineering greatly helped me in developing the practicable battery management system.

I also thank Prof. Wei-Hsin Liao, Prof. Changling Wang, and Prof. Lilong Cai, who were my thesis committee and provided me with valuable comments.

I am indebted to many of my colleagues and friends for supporting me,

including Mr. Chenggang Xia, Mr. Huihuan Qian, Mr. Tin-lun Lam, Dr. Zhancheng Wang, Dr. Jia Liu, Mr. Zhu Cheng, and all the others. They shared their professional knowledge and took time for valuable discussion with me.

Finally, I thank my parents who have given me support and encouragement throughout my life. Their love has sustained me in my growing years, and still does so today. I also greatly appreciate the understanding and support from my girlfriend, Miss Yaya Wu, who accompanied me in experiencing both the joyful and difficult periods.

# Contents

# List of Figures

# List of Tables

# Chapter 1

# Introduction

## 1.1 Motivation

The automotive industry has experienced a significant boom in recent years. As the number of all types of automobiles is increasing, energy shortages and environmental disruption have become the most serious worldwide problems. In America, for example, road vehicles are one of the most important pollution sources, emitting 18% of suspended particulates, 27% of volatile organic compounds, 28% of Pb, 32% of nitrogen oxides, 62% of CO and 25% of $CO_2$ [1]. Meanwhile, America's petroleum consumption for transportation accounts for 71% of total petroleum consumption and 95% of total transportation demand, as shown in Fig. 1.1 [2]. It is undoubtedly time, therefore, to change the propulsion source of the traditional internal combustion engine vehicle (ICEV).

Electric vehicles (EVs), including battery electric vehicles (BEV), hybrid electric vehicles (HEV) and fuel-cell electric vehicles (FEV), are recognized

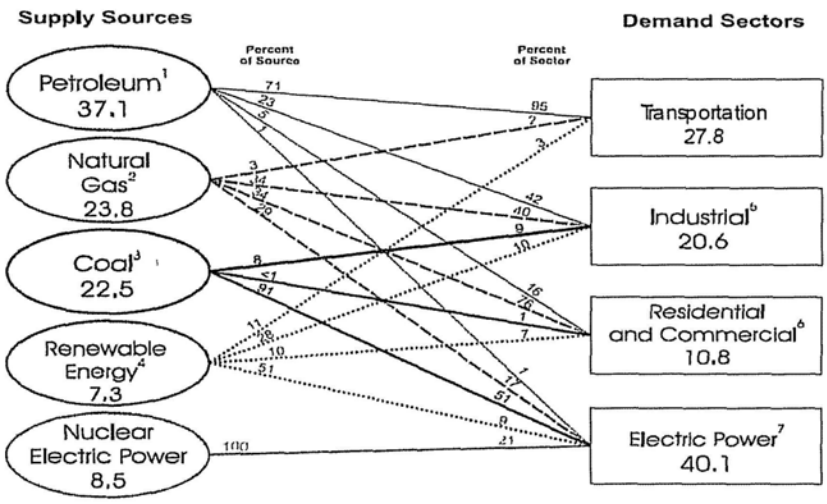


Figure 1.1: U.S. primary energy consumption by source and sector (Quadrillion Btu), 2008.

as the most accessible way of replacing traditional-fuel vehicles, with the promising ability to reduce energy consumption and emissions simultaneously. Although both scientific research and industry have devoted considerable effort to the development of EVs, there are still many obstacles hindering their mass commercialization. Among these obstacles, battery systems, the new energy storage component in EVs, are one of the most important and most difficult aspects of EV design [3].

Battery systems consist of two parts. The battery, which is made by connecting tens or even hundreds of cells in series and/or parallel, converts chemical energy to electrical energy when it discharges and reverses this conversion when charging. The battery management system (BMS) monitors the static and dynamic states of the battery package; it controls its charge and discharge operations to prolong its life, enhance the efficiency of the whole powertrain, guarantee the safety of passengers, and cooperate with

the upper controller, or vehicle management system (VMS).

In fact, existing battery techniques cannot produce batteries that perfectly satisfy the requirements for their application in EVs, especially the consistency of cells in the battery package and their safety in conditions of high-current or high-power charge and discharge. The currently unavoidable defects of batteries and the strict demands of EVs require a multi-functional, reliable, intelligent and safe BMS. *Dickinson et al.* even highlighted the BMS as probably the single most important technical issue in the successful commercialization of EVs [4].

## 1.2 Configurations of Electric Vehicles

To facilitate illustration of battery behavior in EVs and explain the dynamic properties of the charge/discharge currents determined by generators/motors in vehicles, it is first necessary to provide a brief introduction to the configurations of EVs.

Books [5] and [6] comprehensively review the fundamentals, theories, and designs of EVs. Generally, EVs are classified into three categories: BEV, HEV, and FEV [3]. The main difference between the first two types is that BEVs are driven only by an electric power source, the battery, while HEVs usually integrate the power sources from an internal combustion engine (ICE) and a battery. The reason a FEV is treated as a separate type is that the battery in a FEV is made up of fuel cells rather than traditional electrochemical cells. Since the fuel cell has totally different principles and characteristics from electrochemical cells, it is beyond the scope of this thesis and we will

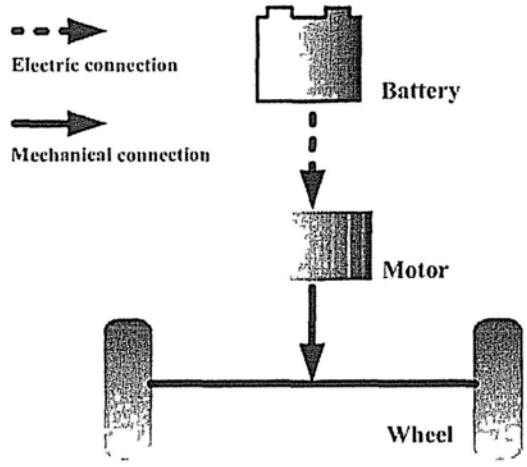


Figure 1.2: The typical configuration of battery electric vehicle

not discuss it in detail.

### 1.2.1 Battery Electric Vehicles

A battery electric vehicle, also known as a pure electric vehicle or zero emission vehicle, has the simplest configuration. It replaces the fuel tank and ICE of an ICEV with a battery and electric motor, as shown in Fig.1.2. The energy flow of a BEV initiates from the chemical energy stored in the battery. Chemical energy is first converted into electrical energy when discharged, and the electrical energy is then converted by an electric motor into kinetic energy to drive the wheels. Although a regenerative braking system can retrieve some energy to recharge the battery, the battery is gradually depleted and has to be charged by external charge sources, such as a specially designed charge station (fast charge) or the household electric grid (overnight charge), before it becomes over-discharged.

Compared with ICEs, electric motors have excellent energy efficiency to

provide adequate torque over a wide speed range. Meanwhile, the change of energy source not only provides an alternative propulsion method for vehicles, but also leads to some completely novel concepts in vehicle design, owing to the flexibility of energy transfer via electric wires instead of rigid mechanical connections.

### 1.2.2 Hybrid Electric Vehicles

Under the general definition of a HEV as a vehicle with more than one energy source, at least one of which can deliver electric energy, a HEV has many options for combining energy sources, such as gasoline ICE and battery, diesel ICE and battery, battery and capacitor, battery and flywheel, or battery and battery [7]. Nevertheless, in practice the most common configuration of HEVs is a combination of ICE and battery. According to the different ways of combining ICE and battery, HEVs also can be sub-categorized into series HEV, parallel HEV, series-parallel HEV and complex HEV [8, 9]. Plug-in HEVs are also a special type of HEV family [10].

#### Series HEV

As shown in Fig.1.3, a series HEV is driven only by the electric motor and fuel energy is totally converted into electric energy to charge the battery. This configuration can be regarded as a BEV equipped with an on-board charger (generator) and an extra energy source (ICE and fuel tank). Thus, the advantages of BEVs, such as flexible design and the high energy efficiency of the motor drive, are inherited by series HEVs.

Since the ICE only works to provide charging current to the battery, the

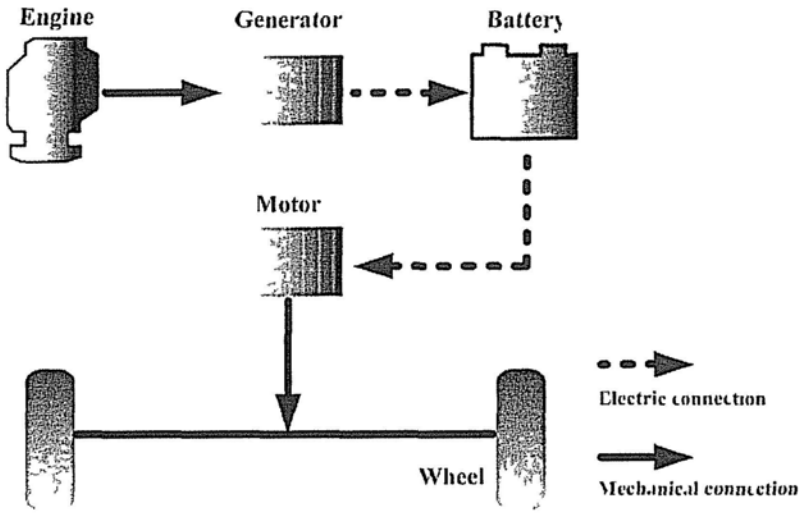


Figure 1.3 The typical configuration of series HEV.

required torque of the ICE changes in a smaller range compared with an ICEV, so that the ICE can be designed to work mostly at high-efficiency and low-consumption working points. However, this configuration involves two energy conversion stages, via the ICE and the electric motor. The indirect energy flow will cause some loss of energy.

### Parallel HEV

In a parallel configuration, as shown in Fig.1.4, the ICE and electric motor are both applied to drive the vehicle directly and their powers are composited through a torque coupler. The method of combining the two energy sources is determined by the torque supply from the ICE and the torque demand of the vehicle, since the battery always acts passively. When the ICE cannot provide enough torque to meet the demand from the vehicle, the battery will discharge and drive the electric motor to compensate. When the torque

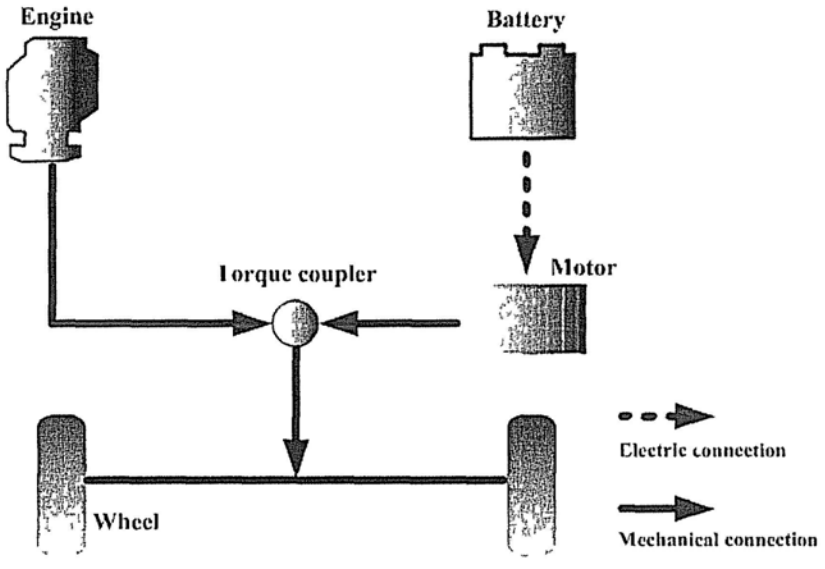


Figure 1.4: The typical configuration of parallel HEV.

provided by the ICE exceeds the demand from the vehicle, the electric motor will rotate in reverse and act as a generator to charge the battery.

One of the advantages of this configuration is that it increases the peak power of the total powertrain when the ICE and battery both release energy. Meanwhile, the ICE can purposely work in its high performance region, leaving the insufficient torque to battery or charging the battery by the extra energy, of cause, when the battery is allowed to discharge or charge. For example, when the vehicle is starting, the battery can provide all the torque that is required and shut off the ICE to avoid its lowest efficiency working point and reduce emissions. However, the flexible energy flow requires more complex management and control algorithms, which are implemented in the VMS and BMS.

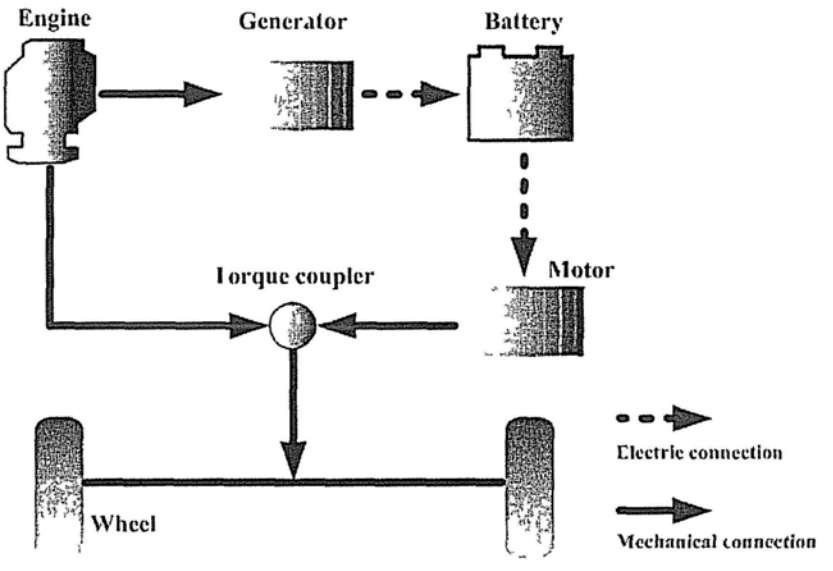


Figure 1.5: The typical configuration of series-parallel HEV

### Series-Parallel HEV

A series-parallel HEV is actually an integrated configuration of series HEV and parallel HEV, as shown in Fig.1.5. Compared with a series HEV, it provides another driving mechanism through an additional torque coupler and, compared with a parallel HEV, it provides an extra battery charge channel using an additional generator. A series-parallel HEV incorporates the benefits of both series and parallel HEVs, but at the cost of higher complexity and expense.

### Complex HEV

From its name, we know that a complex HEV refers to the kind of HEV which has more components, energy flow channels, and/or energy sources. In fact, any HEV that does not belong to the configurations mentioned above

is recognized as a complex HEV. This structure is still under investigation and is expected to realize further potential benefits.

#### Plug-in HEV

Besides the configuration-based classification of HEVs, plug-in HEVs are a special group, referring to an HEV with the ability to recharge its electrochemical energy storage with electricity from an off-board source (such as the electric utility grid) [11], no matter which configuration is used. Unlike other kinds of HEV, whose major power comes from petroleum, the plug-in HEV mainly consumes electric power stored in a large-capacity battery. Since the cost of electricity is lower than petroleum, plug-in HEVs have a clear price advantage. Even taking into consideration the vehicle purchase cost, the large petroleum reduction potential of plug-in HEVs provides strong justification for further development and commercialization [12].

## 1.3 Vehicular Batteries

A vehicular battery is equipped within a vehicle and propels it directly or indirectly. Compared with the batteries used in portable devices, such as laptops, shavers, and so on, a vehicular battery is required to provide much higher performance to satisfy the high maneuverability and powerful powertrain of a vehicle. Among existing batteries, nickel metal hydride (NiMH) batteries and lithium-ion (Li-ion) batteries, including liquid Li-ion and polymer Li-ion batteries, are currently the most practicable for meeting these strict requirements and have been successfully applied in some commercial

Table 1.1: Performance indexes of typical batteries.

| Indexes | | Lead Acid | NiMH | Li-ion |
|---|---|---|---|---|
| Cell voltage | [V] | 2.1 | 1.2 | 3.6 |
| Energy density | [Wh/l] | 50-70 | 200 | 150-250 |
| | [Wh/kg] | 20-40 | 40-60 | 100-200 |
| Power density | [W/kg] | 300 | 1300-500 | 3000-800 |
| Self-discharge | [%/month] | 4-8 | 20 | 1-5 |
| Cycle life | (@80% DoD) | 200 | >2500 | <2500 |
| Cost estimation | [$/kWh] | 150 | 500 | 800 |
| | [$/kW] | 10 | 20 | 50-75 |

Data source: Tab. 2 in [16], 2006.

EVs.

### 1.3.1 Requirements

Although the requirements for vehicular batteries may be different for different vehicle configurations or performance goals, for example the test manuals [13–15] specify the battery requirements in some typical EVs, the general requirements for EVs are listed below.

#### Large Capacity

The capacity of a battery is a measure of the total electric energy that can be drawn from the fully-charged battery in ampere-hours [Ah] (a current of one ampere for one hour is equal to 1Ah). HEVs usually require batteries to hold the capacity for around 10Ah or more, while the batteries in BEVs must have tens (for a sedan) or even hundreds (for a bus) of ampere-hours.

### High Charge/Discharge Rate

The charge/discharge rate refers to the measurement of the charge/discharge current as expressed by the ratio of current to the capacity in C-rate [C]. For example, given a battery with a capacity of 2.3Ah, a 2C discharge means the battery is discharged using a current of 4.6A, and a 0.5C charge means the battery is charged using a current of 1.15A.

Since vehicles demand a high discharge current when accelerating, and feed the energy back to the battery with a high charge current using a regenerative braking system or fast charge station, the batteries need to release or accept the current up to 300A [15], or around $\pm 20C$ (for HEVs) or $\pm 5C$ (for BEVs) [17].

### High Energy Density and Power Density

The energy density includes gravimetric energy density, which is defined as the energy contained per kilogram of battery [Wh/kg], and volumetric energy, which refers to the energy contained per litre [Wh/l]. Similarly, the power density includes gravimetric power density [W/kg] and volumetric power density [W/l].

On the one hand, vehicular batteries must contain sufficient energy and provide enough power to keep vehicles moving fast and over long distances. On the other hand, they are expected to be lightweight and small in volume to reduce unnecessary load and save vehicle space. The solution is to select batteries with high energy and power density. As shown in Tab. 1.1, compared with lead-acid batteries, NiMH and Li-ion have clear performance advantages, which partially explains why these batteries are used in commer-

cialized EVs.

### Long Cycle Life

The cycle life refers to the number of cycles a battery can provide from its birth to inutility, where a cycle stands for a process consisting of a single charge and discharge, usually in the range from 100% to 20% of full capacity, i.e. 80% depth of discharge (80%DoD). As shown in Tab. 1.1, the approximately 2500 cycle life of NiMH and Li-ion batteries are much longer than the 200 cycle life of lead-acid [16], which is the second reason for the popularity of NiMH and Li-ion batteries in EVs.

### Slow Self-discharge

Due to internal leakage between the anode and cathode, cells lose charge even in an open-circuit situation. The self-discharge rate is used to measure the speed of self-discharge as expressed by the ratio of lost charge to the capacity per month as a percentage [%/month]. As shown in Tab. 1.1, Li-ion batteries have an excellent ability to retain energy while NiMH batteries possess the weakest performance in this field.

### Safety

Battery safety takes performance under extreme conditions into consideration, such as nail penetration, external short circuit, overcharging, overheating, and so on [18–20]. Li-ion needs to be most carefully investigated and controlled because there is a risk of it catching fire or even exploding under hazardous conditions, such as short circuiting, overcharging, and thermal

runaway [21–23].

The safety issue becomes much more serious in a vehicular battery containing a large number of cells. Due to the inconsistency of cells, management of the whole battery cannot assure the safety of each individual cell. For example, one cell may already be full while the battery as a whole is still lacking energy. Continuous charge to the battery will inevitably cause overcharging of the outstanding cell and the discharge situation is similar. In addition, performance of the whole battery can suffer from a single damaged cell, i.e. the cask effect, so that it is necessary to detect any defective cell. Therefore, a BMS is recommended to investigate every cell, especially for the Li-ion type [24].

#### Low Cost

The cost of the battery is a crucial factor in the promotion of EVs, which accounts for a large part of the vehicle purchase and maintenance fee. The goal is to reduce the battery manufacturing cost to $100/kWh or less, similar to the current cost of lead-acid batteries [25]. From Tab. 1.1, it can be seen that NiMH and Li-ion batteries are still far away from the target costs. At this stage, many countries have to provide high government subsidies to buyers to stimulate consumption of EVs and to support research and production.

### 1.3.2 Battery Types

Since the scope of this thesis focuses on EV application, the batteries of interest are NiMH and Li-ion. This subsection will briefly introduce the

fundamentals of the electrochemistry of both batteries.

### NiMH Battery

The NiMH battery, the successor of the nickel-cadmium cell, is a type of secondary electrochemical cell with an environmentally friendly hydrogen-absorbing alloy for the negative electrode instead of cadmium. The electrochemical reactions occurring in a NiMH cell are expressed as:

Negative electrode

$$H_2O + M + e^- \underset{\text{discharge}}{\overset{\text{charge}}{\rightleftharpoons}} OH^- + MH \tag{1.1}$$

Positive electrode

$$Ni(OH)_2 + OH^- \underset{\text{discharge}}{\overset{\text{charge}}{\rightleftharpoons}} NiO(OH) + H_2O + e^- \tag{1.2}$$

Overall reaction

$$Ni(OH)_2 + M \underset{\text{discharge}}{\overset{\text{charge}}{\rightleftharpoons}} NiO(OH) + MH \tag{1.3}$$

The "metal" M in the negative electrode of a NiMH cell is actually an intermetallic compound. The most common compound is $AB_5$, where A stands for mischmetal, lanthanum, cerium, or titanium, and B stands for nickel, cobalt, manganese, and/or aluminium [26].

### Li-ion Batteries

Li-ion is a type of rechargeable battery in which the movement of lithium ions produces current. During discharge, lithium ions move from the negative electrode to the positive one, and the process is reversed during charge.

Depending on the type of electrolyte, a battery can be categorized as a liquid Li-ion battery, in which the lithium-salt is held in an organic solvent, or a polymer Li-ion battery, in which the lithium-salt is held in a solid polymer composite such as polyethylene oxide or polyacrylonitrile. In addition, using different cathode materials, it can be realized by $LiCoO_2$, $LiMn_2O_4$, $LiNiO_2$, $LiCo_{1/3}Ni_{1/3}Mn_{1/3}O_2$, $LiFeO_4$, and so forth. Among them, $LiFeO_4$ is generally recognized as one of the most available and suitable types for EV applications. In this thesis, we will use $LiFeO_4$ as the example of a Li-ion battery.

The electrochemical reactions in $LiFeO_4$ are expressed by:

Negative electrode

$$6C + xLi^+ + xe^- \underset{\text{discharge}}{\overset{\text{charge}}{\rightleftharpoons}} Li_xC_6 \tag{1.4}$$

Positive electrode

$$LiFePO_4 \underset{\text{discharge}}{\overset{\text{charge}}{\rightleftharpoons}} Li_{1-x}FePO_4 + xLi^+ + xe^- \tag{1.5}$$

Overall reaction

$$LiFePO_4 + 6C \underset{\text{discharge}}{\overset{\text{charge}}{\rightleftharpoons}} Li_{1-x}FePO4 + Li_xC6 \tag{1.6}$$

In fact, the battery charge and discharge are Li-ion intercalation and deintercalation processes.

## 1.4 Battery Management System

A vehicular battery faces a severe working environment. On the one hand, it consists of a large number of cells to provide the necessary driving power. The voltage and current of the battery pack are both much higher than in other electronic devices, such as shavers or mp3 players. On the other hand, vibration, electromagnetic interference, uneven temperature fields and other negative conditions cannot be avoided in vehicles, leading to damage and danger to the battery. In addition, the cost of the battery accounts for a large part of the whole vehicle cost, especially for BEVs, in which it represents approximately half the cost. To reduce the cost of electric vehicles, it is necessary to protect the battery and prolong its life cycle.

The battery, as a passive component, has no ability to protect itself. Therefore, a BMS, a newly proposed vehicle controller, takes responsibility for managing the battery system and communicating with the VMS to report the state of the battery system.

### 1.4.1 Functions

In [16], a BMS is defined as a system for monitoring the correct battery pack operation and performing the appropriate safety steps in case of hazardous situations. Besides the monitoring and protection functions, [24] suggests the BMS should control and balance the battery package. [27] also adds

state estimation and communication functions.

In summary, Tab.1.2 lists the general functions of BMS and their details are described in the following.

Table 1.2: Functions of battery management system.

| | |
|---|---|
| **Monitoring** | Cell voltage |
| | Battery pack voltage |
| | Battery pack current |
| | Battery temperature field |
| **Protection** | Overcurrent |
| | Overvoltage |
| | Leakage of electricity (Insulation) |
| | Overcharge |
| | Overdischarge |
| **Estimation** | State of charge |
| | State of health |
| **Control** | Charge control |
| | Cell equalization control |
| | Thermal control |
| | Pre-power control |
| **Communication** | SPI in module |
| | CAN in vehicle |
| | COM between BMS and PC |

### Monitoring

Monitoring a battery involves sampling the relevant data from the battery at a sampling frequency. Although complex electrochemical reactions occur inside a battery, only the terminal voltage, bus current, and cell surface temperature can be directly measured. The following estimation, protection,

and control functions have to be realized based on these limited data. Therefore, monitoring is the basis of the BMS and it should obtain information as accurately as possible.

Cell voltage measurement is usually implemented through isolation operation amplifiers or special chips, such as AD7280 produced by Analog Devices, Inc., and LTC6802 produced by Linear Technology. Current measurement is usually implemented through current shunt and isolation operation amplifiers or current sensors. Temperature measurement can be realized using a thermocouple, thermistor and so on, typically a negative temperature coefficient thermistor (NTC).

### Protection

To prolong life cycle, equally to reduce the cost of EVs, and guarantee the safety of the whole vehicle system, especially the driver and passengers inside the vehicle, automatic detection of abnormal situations is necessary.

At the battery pack level, the BMS is concerned with four abnormalities. First, if the current is larger than the charging or discharging ability of the battery, known as over-current, it will cause permanent damage to the cells and the risk of firing or exploding. Secondly, if the charging voltage is higher than the float voltage of the battery, known as over-voltage, it has the potential to breakdown the electrodes and cause an internal short-circuit. To guarantee the safety of passengers, it is also necessary to make sure the battery system is absolutely insulated from the vehicle body and no leakage of electricity can occur.

At the cell level, the main protection is to avoid overcharge and overdis-

charge. These functions are implemented based on the detection of the full charge and empty states, as indicated by the SoC.

### Estimation

The battery is typically a less-information system, inside which some crucial states are not directly measurable, such as state of charge (SoC) and state of health (SoH). These hidden states have to be estimated based on the limited data obtained by monitoring.

In EV applications, SoC, defined as the ratio of residual charges in a battery to its capacity, is the most important state of the battery, indicating the capacity left in the cell. For BEVs, SoC is used to determine the range, while for HEVs it determines when the engine is switched on and off. In addition, SoC is the basis for preventing cells from overcharge and overdischarge. Furthermore, in charge control and equalization control, SoC is also a critical input to the controller to calculate the control variables.

The SoH is another important state of the battery, which indicates the cell's ability to deliver the specified performance compared with a fresh battery. Simply speaking, it reflects the aging of the cell. Since many battery parameters have a close relationship with the SoH, a change in these parameters would be used as an indicator of the SoH. Meanwhile, the number of charge-discharge cycles is usually a measure of the SoH if no extreme abuse of the battery occurs. Therefore, a log-book of battery usage is helpful to estimate the SoH.

### Control

Charge control is an essential feature of a BMS. Statistical data show that inappropriate charging is the primary cause of damage to batteries. Thus, the basic requirement of charge control is to assure the protection of the battery. In addition, unlike the overnight charge in most portable electronic devices, EVs require the battery to charge quickly so that the out-of-service time can be reduced to an acceptable level. In this sense, charge control is an important factor determining the commercialization of EVs.

A vehicular battery is made up of multiple cells. Due to the inconsistency of cells, an imbalance of cells is impossible to avoid. Cell imbalance negatively affects the performance of the battery for two reasons. Firstly, there is the risk of overcharging the strongest cell and discharging the weakest cell. Secondly, it greatly reduces the usable capacity of the whole battery pack - its discharge ability is determined by the weakest cell and its charge ability is limited by the strongest. Therefore, equalization control is also an essential function of the BMS.

Thermal control is needed to keep the temperature of the battery pack within a safe range and to balance the temperature field. Thermal management usually has two steps. The first step is the design of the layout inside the battery pack based on thermo analysis methods, for example finite element analysis, aimed at establishing a naturally uniform temperature field. Strictly speaking, this step is not involved in BMS design. The second step is online control of the battery temperature. The actuators, such as fans, are simply controlled to be on or off.

Pre-power control works only at the moment the vehicle starts. Its goal is

to limit the initial current within a safe range by series-connecting a resistor. This function allows a soft start behavior, which is beneficial to the motor. After self-diagnosis of the whole vehicle system, the resistor will be switched off and the battery system switches to its normal service period.

#### Communication

Communication in the BMS exists on three levels. Communication inside the battery module is implemented by a serial peripheral interface (SPI). The communication between the BMS and other vehicular components occurs through the standard controller area network (CAN) bus. The serial communication interface (SCI) port is additionally realized to facilitate fault diagnosis and testing via computers.

### 1.4.2 Research Issues and Challenges

In this thesis, besides the realization of a practicable BMS that has been assessed using testing equipment and applied in a real electric vehicle, some novel methodologies and solutions are also proposed to solve the challenging research issues in BMSs.

#### State of Charge Estimation

SoC is the crucial state in battery, based on which BMS and VMS can determine whether to charge or discharge, what is C-rate, whether battery cells are in balance, and how to equalize them. Unfortunately, SoC can not be measured directly so that the estimation of SoC becomes to one of the most important issues in BMS design.

The SoC is the crucial state of the battery, based on which the BMS and VMS can determine whether to charge or discharge, what the C-rate is, whether the battery cells are in balance, and how to equalize them. Unfortunately, the SoC cannot be measured directly so estimation of the SoC becomes one of the most important issues in BMS design.

The difficulties of SoC estimation for vehicular batteries arise mainly from three issues. Firstly, measurement of the battery current is inaccurate due to a large measuring range and various sources of interference. Secondly, a battery is a typical time-variant plant, a linear model with fixed parameters that are difficult to determine accurately. Thirdly, the approximate true value of the SoC is only available after the vehicle stops. No correction can be made during the running process.

For the LiFePO4 battery, SoC estimation becomes more difficult because there is a very flat relationship between SoC and OCV, so that changes of state inside the battery are not obviously reflected in the outside measurable states. Therefore, it is necessary to develop highly accurate measurements and advanced estimation models and algorithms.

### Cell Equalization Control

Cell equalization consists of two parts, the equalization circuit and the equalization algorithm. Previous research on cell equalization mainly focuses on the first, and various circuits have been proposed. Depending on whether the equalizing current can be controlled online, these circuits can be divided into two categories. The uncontrollable circuit usually has a simple structure, but the equalizing current is either fixed to a constant or is passively changed

along with cell voltages.

Cell equalization has a number of goals, such as safety and prevention of damage, short equalization duration, and high energy efficiency. To realize the multiple objectives of equalization, it is necessary to tune the equalizing current according to the state of the battery. Therefore, in this thesis, we select a controllable circuit as the basis for studying the equalization algorithm.

Unlike equalization circuit design, equalization algorithms to determine the equalizing current have not been comprehensively and intensively investigated yet. One major difficulty is that no model or theory has been established to map the battery state to a best equalizing current. Furthermore, the inputs of the equalizing controller to determine the equalizing current is still under exploration. Based on the fact that battery equalization is essential to equalize SoC rather than voltage, we propose a set of control inputs in this thesis. To incorporate human experience and knowledge of equalization, a fuzzy controller based on SoC has also been proposed.

### Fast Charge Control

Charge control has three similar goals: safety and prevention of damage, short charging duration, and high energy efficiency. Therefore, it is naturally a multi-objective control problem. In addition, due to the time-variant property of battery, a pre-determined charging profile may not be always suitable along with the changes in battery states. Open-loop control manners have difficulties in solving this problem. Meanwhile, performance evaluation of the charging process should be based on the whole period. Good performance

over a short time is insufficient to indicate a good overall performance. A charge controller is required to take future charging behavior into consideration when calculating the present charging current.

Modeling of batteries has been comprehensively studied in recent years. Available battery models establish the basis for applying a model predictive control (MPC) framework to solve the charge control problem. Three advantages of MPC explain the rationale. Firstly, it has the ability to predict future battery states under a possible future charging sequence and hence evaluate charging performance over a comparatively long period. Secondly, it calculates the best charging sequence using an optimization method, which can solve multi-objective problems. Thirdly, since it utilizes a receding horizon strategy and only applies the first element of the best charging sequence at each control moment, prediction error caused by model inaccuracy will not accumulate because instantaneous measurements correctly update each initial prediction value.

## 1.5 Thesis Organization

The contents of this thesis are organized as follows.

Chapter 2 illustrates the system structure and hardware design of our BMS prototype. First, we discuss the need to investigate each cell of the Li-ion battery and propose solutions for improving the system framework. We then illustrate the details of the circuit design. Finally, the simulations, experiments and application platforms are introduced.

Chapter 3 focuses on the robust SoC estimation framework. We propose

an adaptive-$\kappa$ nonlinear diffusion filter to reduce noise, and a self-learning mechanism to remove zero-drift in the measurement of current. Then an $H_\infty$ filter is utilized to realize the robust estimation using a fixed model in simulation, while an extended Kalman filter, based on a modified enhanced self-correcting model, is used in the experiments and real application. Simulations, experiments and real application in a HEV all demonstrate the availability and efficacy of the proposed framework.

Chapter 4 proposes a SoC based fuzzy controller to equalize cells. Since a large difference in SoC results in a small difference in voltage for the LiFePO4 battery, the traditional voltage based equalizer has difficulty balancing the cells. We apply the bi-directional Cuk circuit as the equalization basis and select three inputs to the fuzzy controller, each of which represents a relevant issue during equalization. Then, a fuzzy controller is established based on experts' experience and knowledge. Both the simulations and experiments are designed to test the performance of the proposed method.

Chapter 5 proposes a fast charge framework based on model predictive control, with the aim of simultaneously reducing charge duration, which represents the out-of-service time of vehicles, and temperature increase, which represents safety and energy efficiency during the charge process. Given a future charge sequence, we apply the battery models to predict future SoC and temperature. A genetic algorithm is then applied to find the best charge sequence under a specified fitness function. Both simulations and experiments demonstrate that the Pareto front of the proposed method dominates that of the most popular CCCV method.

Chapter 6 concludes with the contributions of the thesis and highlights

future research.

---

□ **End of chapter.**

# Chapter 2

# System Structure and Hardware Design

## 2.1 Introduction

A vehicular battery pack must consist of a large number of cells to provide the necessary energy and power to drive EVs. Unlike portable devices, it is impossible to manage the vehicular battery only at the pack level, which leads to two problems: out-of-investigation cells and lack of cell equalization ability.

Firstly, the state of cells cannot simply be calculated according to the state of the pack. Cell imbalance causes the state of some cells to be far away from the average, especially when there are a large number of cells. These abnormal cells, which should be closely supervised, are out of the range of investigation and hence risk abuse and even damage, such as overcharging, overdischarging, and so forth. Furthermore, if one cell is broken, the pack

manager cannot identify it; the whole pack has to be replaced and then repaired off-line.

Secondly, management at pack level cannot equalize the cells. This disadvantage not only intensifies the first problem, but also limits the performance of the whole pack. A battery is a typical system with a cask effect, in which the weakest cell determines the discharge ability of the pack, while the strongest determines its charge ability. For example, given the extreme case in which one cell's SoC is 1 while another's is 0, how should the battery pack operate? Charging will cause overcharge damage to the full cell, while discharging cannot avoid overdischarge damage to the empty one. Without cell equalization, the battery pack is unserviceable even though the pack still contains a large number of charges.

The above analysis reveals that a BMS for vehicular batteries must have a specially designed system structure and must manage the pack as well as the individual cells.

The first option is a centralized structure. In this structure, the pack and all cells are managed by a single micro-programmed control unit (MCU) [28, 29]. Due to the large number of cells, the MCU has to measure and control cells in turn, using selective circuits. Obviously, this design cannot investigate cells in real time. In addition, it is very hard to estimate the SoC of each cell in a single MCU.

A hierarchical structure (also known as a modular BMS) is therefore a more reasonable design, in which cells are first grouped into modules managed by modular controllers, and then modules are incorporated into a pack managed by a central controller. Design considerations for a modular BMS

include the following:

1. how to distribute tasks to modular and central controllers;
2. how to communicate with each other;
3. how to measure and control cells and the pack;
4. how to provide power supply for controllers.

Stuart *et al.* presented a complete prototype of a modular BMS [24]. The modular controller takes responsibility for cell voltage measurement, temperature measurement, and cell equalization control. The tasks of the central controller include current measurement, data collection, synchronization and processing, battery SoC determination, safety features, module on/off control, system monitoring during sleep mode, and battery maintenance equipment control. The communication between the modules and the central controller is via a CAN bus with speed and reliability advantages. Cell voltage is measured using an operational transconductance amplifier and then sent to a local controller via a switch and voltage transfer circuit in turn. The power supply for the central controller comes from two sources: the 12V vehicle battery when the system is in sleep mode, or the propulsive battery pack via a DC/DC converter otherwise. The local controllers are powered by the central controller.

This modular BMS prototype establishes a good example to the followers, and some modifications have been made in the following years.

While this modular BMS prototype established a good example, some modifications have been made subsequently. Chatzakis *et al.*, aiming to

provide fault-tolerant capability and protection, equipped each modular controller with a current sensor to determine if any current leakage occurred in the battery string and also to estimate battery states [30]. However, in this study, the total error in cell voltage measurement was too large to estimate SoC (50mV voltage error corresponds to about 25% change in SoC). Meanwhile, accuracy of current measurement was also unsatisfactory (about 0.7A in the range of 15A or 4.7% of the range). These problems highlight the significance and difficulty of measurement in BMS.

Chen *et al.* proposed a new communication method between modules and the central controller [31]. A module communicates with its adjacent counterparts to transfer data and commands. Only the furthest module communicates with the central controller directly. This design is known as daisy chain and has been adopted in commercial BMS chips AD7280 [32] and LTC6802 [33].

Most recently, Stuart *et al.* concluded that "modular BMS provides a relatively simple yet accurate means of managing the large Li-ion packs such as those found on commercial electric vehicles or aerospace applications" [34].

## 2.2 System Structure

The system structure of the BMS in this thesis also follows the modular concept and its implementation proposed in [24]; however, it includes some modifications to improve accuracy, modularization, and intelligence.

### 2.2.1 Considerations of Modification

#### Task Distribution

SoC estimation has been treated as the pack-level task in [24] and implemented in the central controller. The purpose of this idea may be understood in two ways.

Firstly, it may imply that the central controller only estimates the SoC of the pack using the pack's voltage, current, and other related data, as applied in [29]. However, the SoC of the pack is a meaningless term in practice. For example, what is the SoC of the pack in which the SoC of one cell is 0 and another is 1? Cell imbalance causes overcharge and overdischarge of cells when control is based on the SoC of the pack.

Secondly, the central controller may estimate the SoC of each cell. In this case, the large number of cells results in a heavy computing load to the central controller. In addition, each module controller has to report the voltage of each cell to the central controller, leading to a very busy CAN bus.

Therefore, no matter which implementation is applied, it is not feasible to assign the SoC estimation task to the central controller. This provides a strong rationale for distributing the cell SoC estimation task to module controllers. Besides the obvious benefits, such as considerable load reductions on the central controller and CAN bus, it also allows the module controller to equalize cells based on cell SoC rather than voltage.

### Communication

There are two options for communication between modules and the central controller: daisy chain and CAN bus.

Although daisy chain has been adopted in some BMS chips, it has two disadvantages. The first is that communicating data or commands to one module requires transmission through all the modules between it and the central controller. This results in a heavy transmission load and hence may cause delays and errors. The second is that, if one module is broken, subsequent modules can no longer communicate with the central controller. This leads to the failure of the whole pack. One solution is redundant design, which establishes two parallel daisy chains, but at double the cost.

CAN bus, the vehicle bus standard designed to allow communication among controllers and devices within a vehicle, is a message-based protocol which has been successfully applied in automotive engineering for many years. It has three features: (1) a multi-master hierarchy in which the communication network is still able to operate even when one node is defective, (2) broadcast communication, which guarantees data integrity as all devices in the system use the same information, and (3) sophisticated error detecting mechanisms and re-transmission of faulty messages.

Therefore, we follow the CAN bus design used in previous work and establish a communication system with dual CAN buses in our BMS, one for communication inside the BMS, and the other for communication among BMS and other vehicular controllers, such as the VMS.

### Measurement

Cell voltage measurement is crucial to estimate cell states and hence protect the cells and battery pack. Most past designs measure voltages using an operational amplifier and convert them to digital signals via the AD ports of a MCU. However, measurement accuracy is not satisfactory. For example, the voltage measurement error in [30] is 50mV (roughly corresponding to 25% SoC error), maximum 9mV for a 3.5V cell (4.5% SoC) in [24], and at least 4mV for a 4V cell (2% SoC) in [34]. To enhance accuracy, we apply the IC AD7280 to measure cell voltage. Its typical accuracy is 0.07% (-40°C to 85°C), equal to 2.8mV for a 4V cell (1.4% SoC). In addition, six cells can be measured by a single AD7280. Conversion time for each channel is only 1us so that voltage sampling frequency is fast enough to be treated as realtime measurement.

Current measurement is another critical factor. The current of a vehicular battery is much more dynamic than in portable devices. Its range usually covers -300A to 300A [15]. The large range causes difficulty in achieving accurate current measurement. In this thesis, we select the HTFS200-P/SP2 current sensor to measure pack current [35]. It is a hall-effect sensor linearly converting ±300A current to 2.5±1.875V voltage. Its accuracy excluding offset is around ±1%, which causes error of several amperes in the higher range. It is clearly very hard to improve the accuracy of current measurement by hardware design alone. Therefore, in chapter 3, we propose a filtration method and a zero-drift removal algorithm to enhance accuracy in a soft manner.

#### Power Supply

How the controllers are powered is closely related to modularization. Good modularization should reduce the dependence between each module. In the existing design, the module controllers are usually powered by the central controller. Although this design allows the central controller to easily shut power down to the module controllers, it has two disadvantages. First, modules cannot work independently so it is impossible to conduct self-test and self-diagnosis before assembly. Second, malfunction or even danger in one module may affect the whole pack. For example, a short circuit in the power circuit of one module will lead to a high short circuit current on the central board and short out other modules.

In this thesis, therefore, the module controller is powered by the cells inside. In this way, a module can work independently. Any module can be easily replaced if there is a problem, and the failure of the module will not affect any other parts.

### 2.2.2 Overview of the Proposed Structure

Based on the modular concept and consideration of the modifications discussed above, we have designed and implemented a new BMS. An overview of the proposed structure is shown in Fig. 2.1.

Each module contains 12 series connected cells, investigated and controlled by a module controller. The cells and module controller are encapsulated within a module pack, externally leaving only two power bus wires and two CAN bus wires. The module pack is a self-powered and self-organized

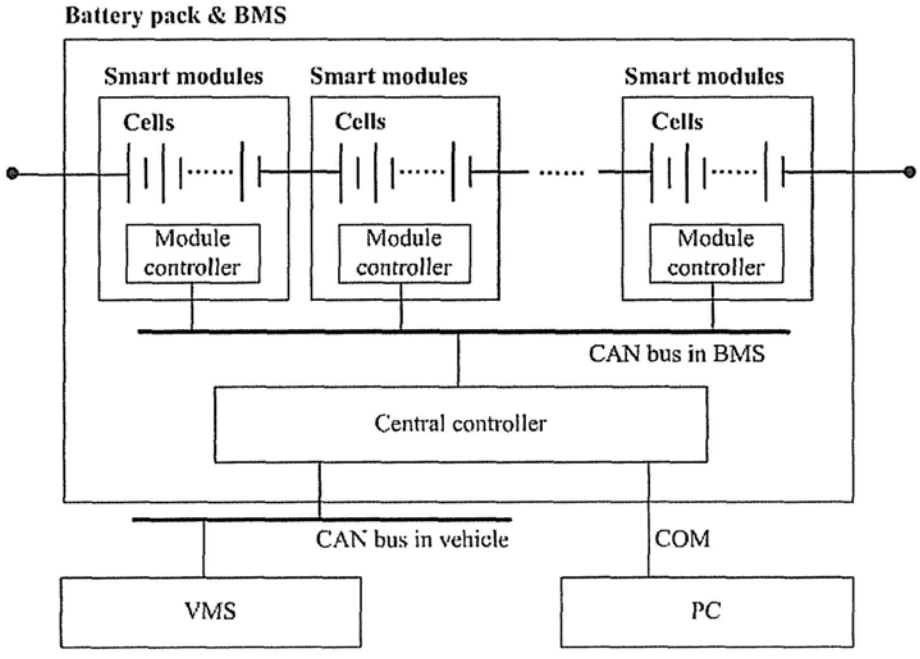


Figure 2.1: System framework structure of the proposed BMS.

system, called a smart module. Smart modules are series-connected to form the battery pack. A central controller is equipped within the pack and management takes place at pack level. The assignment of tasks to module controllers and the central controller are listed in Tab. 2.1. Communications are implemented on two levels, one for BMS internal communication and one for communication at vehicle level. The communication data are listed in Tab. 2.2.

## 2.3 Smart Module

A schematic diagram of a smart module is shown in Fig. 2.2. A smart module applies two AD7280 ICs to measure the voltages of 12 cells. Four temperature sensors are fixed in the module to roughly measure temperature.

Table 2.1: Assignment of tasks in the proposed modular BMS.

| **Smart Modules** |
|---|
| Cell voltage measurement |
| Module temperature measurement |
| Cell SoC estimation |
| Cell equalization |
| Cell overcharge and overdischarge detection |
| Communication with the central |
| **Central Controller** |
| Pack current measurement, overcurrent detection |
| Pack voltage measurement, overvoltage detection |
| Current leakage detection and protection |
| Lowest, average and highest cell SoC calculation |
| Pre-power control |
| Thermal control |
| Disconnect battery from vehicle in emergency |
| Communication with modules |
| Communication with VMS |

Table 2.2: Data communication on the CAN buses.

| | |
|---|---|
| CAN bus in BMS | **Smart Modules → Central Controller** |
| | Lowest, average and highest cell SoC |
| | Module temperature |
| | Error code if any |
| | **Central Controller → Smart Modules** |
| | Pack current |
| | Switch to sleep mode |
| CAN bus in vehicle | **Central Controller → VMS** |
| | Lowest, average and highest cell SoC in battery pack |
| | Error code if any |
| | **VMS → Central Controller** |
| | Switch to sleep mode |

All the data are sent to the module controller MC9S12XEP100MAL [36]. SoC estimation, overcharge and overdischarge detection, and equalization control are all implemented in the controller in a soft manner.

### 2.3.1 Power Supply

The cells inside the module provide the power source for the module controller. Since each module contains 12 cells, the voltage of the power supply may vary from 30V (2.5V cut-off voltage) to 50.4V (4.2V full voltage) for a li-ion battery, and from 12V (1V cut-off voltage) to 16.8V (1.4V cut-off voltage) for a NiMH battery. To develop a universal BMS, it is necessary to ensure the power supply is always stable with such a large variation. In this thesis, we select the IC TPS54160 for the power supply, as shown in Fig. 2.3 [37]. TPS5410 is a 60V, 1.5A, step down regulator with an integrated high side MOSFET. Its input voltage range is from 3.5V to 60V, which covers all possible types of vehicular battery. Its output voltage is set by a resistor divider from the output node to the VSENSE pin, as expressed by

$$Vcc = 0.8 \times \frac{R_1}{R_2} + 0.8V \tag{2.1}$$

where $R_1 = 53.6k\Omega$ and $R_2 = 10k\Omega$ in this thesis. Thus, power supply voltage of the module controller $Vcc = 5.088V$.

### 2.3.2 Cell Voltage Measurement

To realize a highly accurate and fast cell voltage measurement, we select the IC AD7280 to obtain cell voltage directly [32]. Since each chip has the abil-

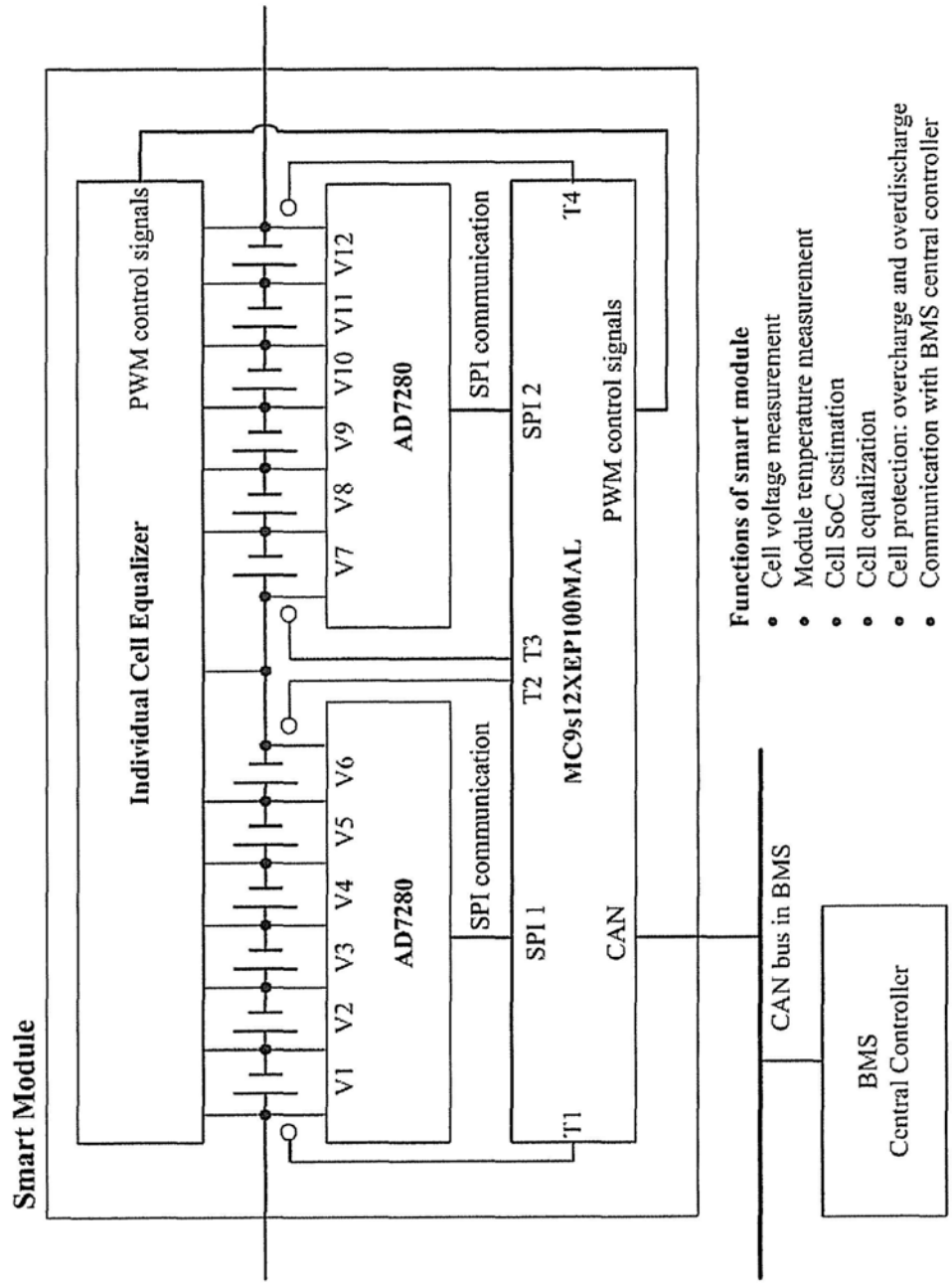


Figure 2.2: Structure and functions of smart module.

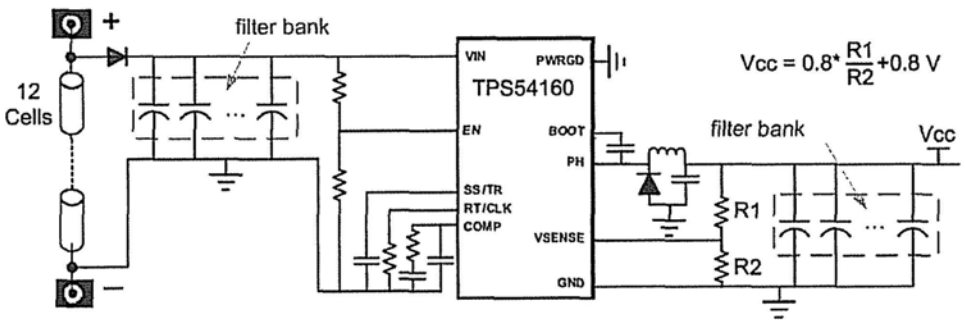


Figure 2.3: Schematic diagram of power supply for module controllers.

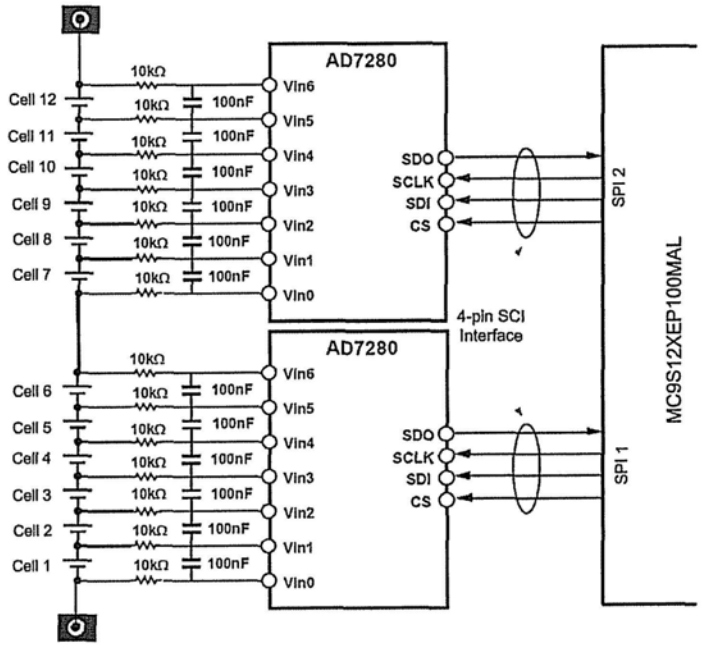


Figure 2.4: Schematic diagram of voltage measurement.

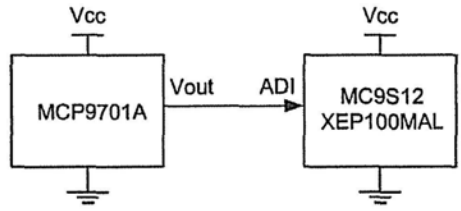


Figure 2.5: Schematic diagram of module temperature measurement.

ity to measure six cells, a module contains two chips, as shown in Fig. 2.4. To provide protection to the analog inputs in case of overvoltage or undervoltage of cells, for each channel a 10k$\Omega$ resistor is connected with a cell in series. In conjunction with the resistor, a 100nF capacitor across the pseudo differential inputs acts as a low pass filter, with a cut-off frequency of 318Hz. This external measurement configuration allows a combined acquisition and conversion time of 1$\mu$s, which is fast enough to be recognized as realtime measurement. To send the voltage measurement results, the two AD7280s both communicate with the MCU via SPI ports, rather than via daisy chain. Its typical accuracy is 0.07% (-40°C to 85°C), equal to 2.8mV for a 4V cell (1.4% SoC). It has the best performance for voltage measurement, as discussed in the previous section.

### 2.3.3 Temperature Measurement

We apply the IC MCP9701A to measure the temperature inside the module [38]. MCP9701A is the most accurate of the low-power linear active thermistors in the MCP9000 family. It has a very simple external circuit, as shown in Fig. 2.5. The output voltage $V_{out}$ has a linear relationship with the

ambient temperature $T_a$, as expressed by

$$V_{out} = T_c \times T_a + V_{0°C} \tag{2.2}$$

where the temperature coefficient $T_c = 19.5mV/°C$ and sensor output at $0°C$ $V_{0°C} = 400mV$.

The typical accuracy of MCP9701A is $\pm 1°C$ when $T_a = 0°C$ to $70°C$. It is noteworthy that the BMS is designed for vehicles in Hong Kong where the temperature is seldom lower than $0°C$. If the BMS is equipped within a vehicle used in colder areas, MCP9700A is more suitable because it can work at $-25°C$.

### 2.3.4 Cell Equalization

Cell equalization is implemented in two ways in this thesis.

The first method is the traditional discharging equalization, which discharges the cells with higher SoC through dissipative resistors. With the advantage that the interface for cell equalization is already integrated in the AD7280, the implementation of discharging equalization is quite simple, as shown in Fig. 2.6.

When the MCU detects one cell's SoC is higher than others, for example if it exceeds a threshold, the MCU will send the equalization command to AD7280, which will make the corresponding MOSFET discharge the cell through its bypass resistor. The resistances of R1 to R12 determine the discharging current of cells in equalization. Selection of the resistance should take two points into consideration. For discharging equalization, the equal-

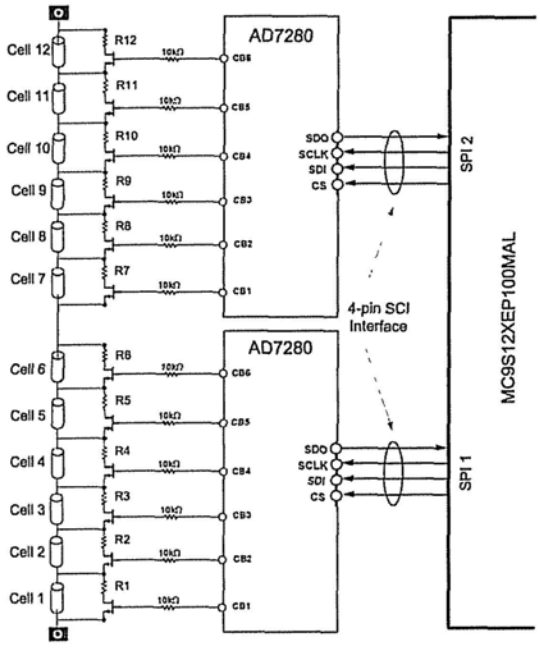


Figure 2.6: Schematic diagram of cell equalization.

izing current cannot be too large, typically 0.01C. Meanwhile, discharging power cannot exceed the bearing capacity of the circuit board. In this work, the resistances are set to 46Ω, corresponding to about 0.069A equalizing current for the 6.9Ah LiFePO4 cells in our application.

Although equalizing cells using this discharging method is quite simple, and it has been applied in many existing EVs, some disadvantages hinder its future promotion. First, it is a dissipative method causing energy loss on the resistors. Second, the heating of the resistors will cause problems for thermal management, especially for retaining a uniform thermal field. In addition, the discharging current is a constant determined by the discharging resistor and is usually designed to be small. This feature causes a long equalization period, especially when the imbalance is excessive.

Therefore, to improve the quality of equalization, it is necessary to develop an advanced equalization method. In Chapter 4, an intelligent transferring equalization approach has been proposed to study this issue further.

### 2.3.5 Microprogrammed Control Unit

Selection of the MCU in a BMS should consider cost, power consumption, EMC, code-size efficiency, communication ability, adaptability and reliability in the vehicle environment, and so forth. The freescale MC9S12XE-family delivers 32-bit performance with all the advantages and efficiencies of a 16 bit MCU [36]. It features an enhanced version of the performance-boosting XGATE co-processor. It is programmable in "C" language with an instruction set optimized for data movement, logic and bit manipulation instructions. It also has strong communication ability with external devices, including eight synchronous serial communications interfaces (SCI), three serial peripheral interfaces (SPI), two 16-channel, 12-bit analog-to-digital converters, one 8-channel pulse-width modulator (PWM), five CAN 2.0 A, B software compatible modules (MSCAN12), and so on.

Based on these features, we apply the MC9S12XEP100MAL as the MCU in both the module controller and central controller. Its block diagram is shown in Fig. 2.7. The green items stand for the ports used for communication with other components in this work.

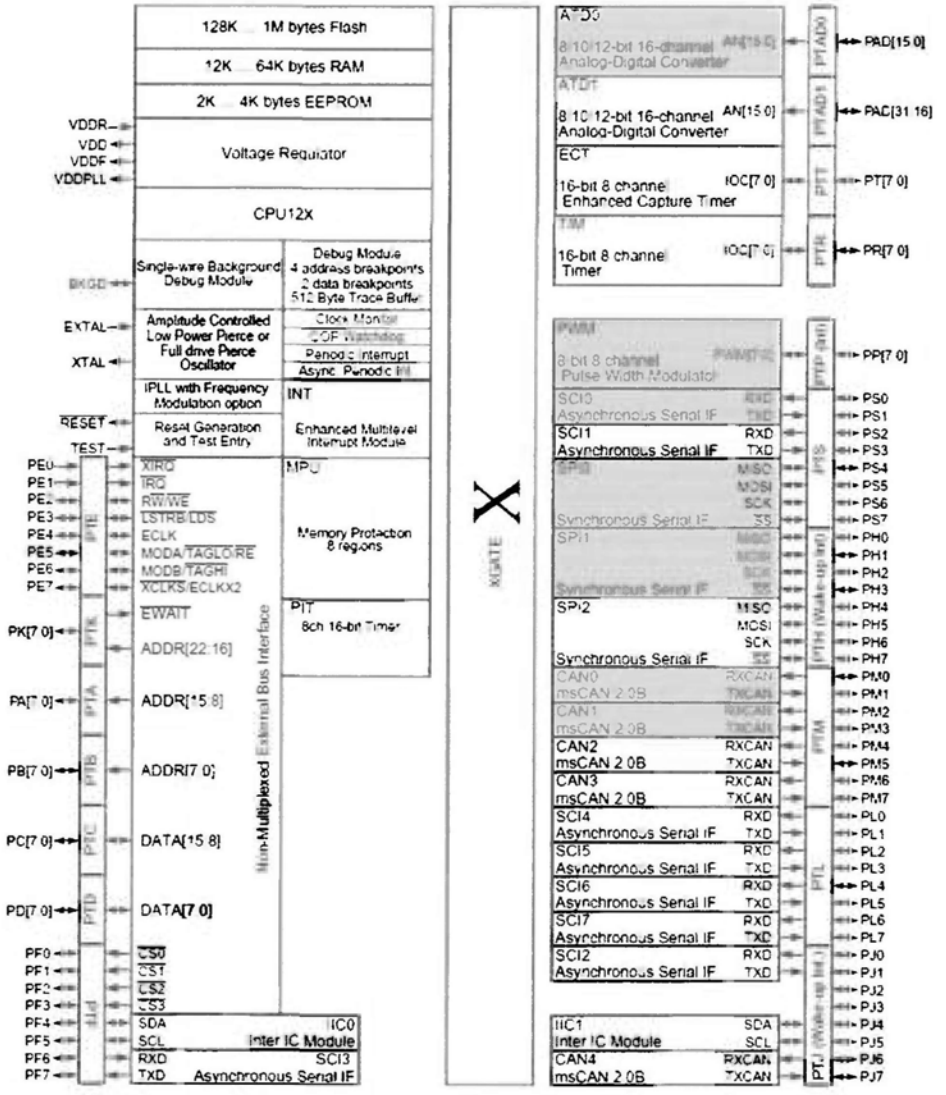


Figure 2.7: Block diagram of the applied MCU MC9S12XEP100MAL, in which the green items standard for the ports used for communication with external components in this work.

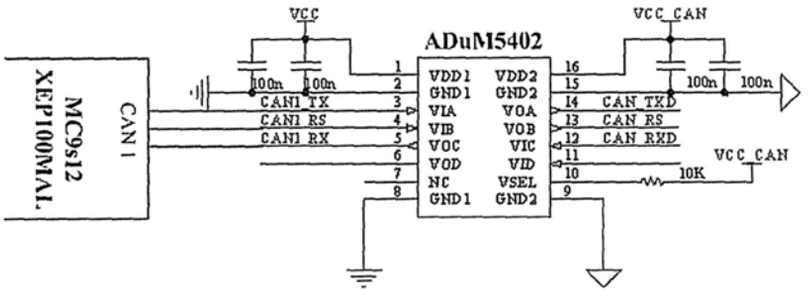


Figure 2.8: Schematic diagram of CAN isolation.

### 2.3.6 Controller Area Network

CAN bus communication is very important for automotive engineering. It is realized in two steps.

First, ADuM5402 is applied to isolate the signals in the controllers from the CAN bus, as shown in Fig. 2.8. The ADuM5402 isolator provides four independent isolation channels in a variety of channel configurations and data rates. The number of channels is sufficient to use a single chip to handle the isolation of CAN communication.

Next, the high speed CAN-transceiver TLE6250 is applied to work as an interface between the CAN protocol controller and the physical differential bus, as shown in Fig. 2.9 [39]. TLE6250 is optimized for high speed differential mode data transmission in automotive and industrial applications. Protection of electrostatic discharge (ESD) is implemented based on the dual line CAN bus protector NUP2105L [40]. To improve anti-EMI ability, B82793, the choke for data and signal lines, is also series connected with the CAN lines [41].

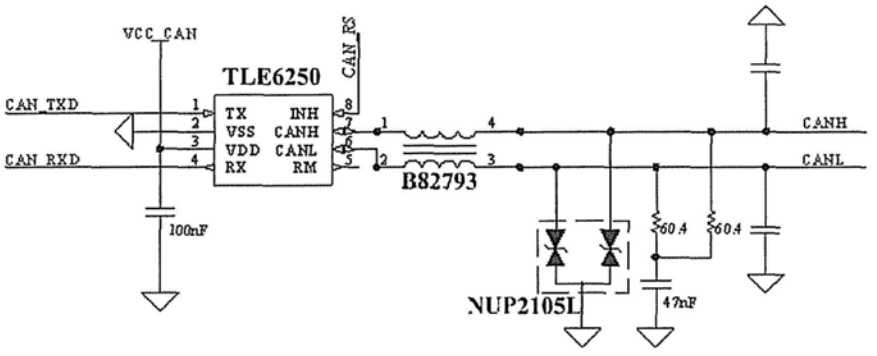


Figure 2.9: Schematic diagram of CAN transmission.

### 2.3.7 Implementation

Fig. 2.10 shows the photograph of the implemented module controller. Its size is 95mm*95mm*11.6mm, with four layers. The small size allows it to be fixed in a small volume.

## 2.4 Central Controller

The schematic diagram of the central controller is shown in Fig. 2.11. It mainly focuses on management at the pack level, including measurement of pack voltage, pack current, and current leakage of the pack. It also drives fans and contactors to control pack temperature and the opening/closing of the battery power bus.

### 2.4.1 Power Supply

The power supply of the central controller is the 12V vehicular battery rather than the high voltage propulsive battery pack, for two reasons. First, the power voltage on the controller board is 5V, while that of a propulsive battery

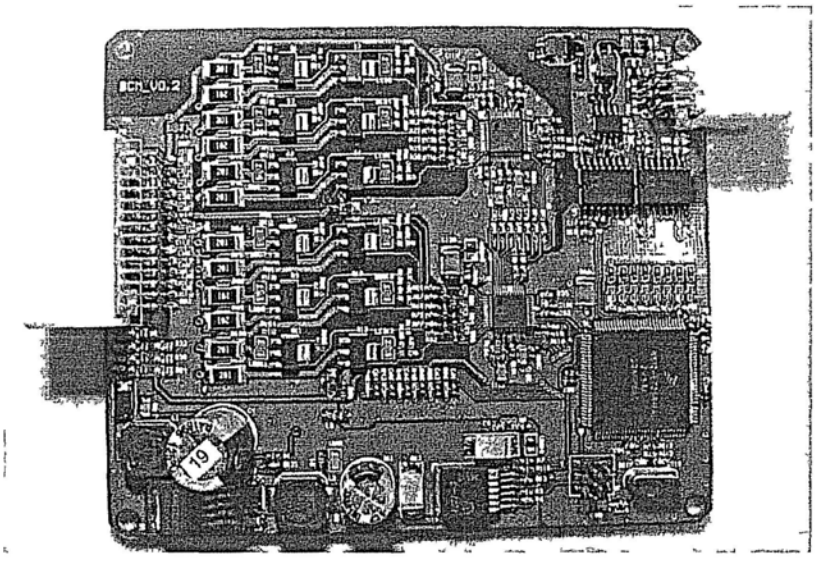

Figure 2.10 Photograph of the implemented module controller

pack usually is more than 300V. The large difference in voltage requires a complex and expensive DC/DC converter to provide a stable power supply. Second, the central controller works at the vehicle level, whereas most other units are powered by the 12V vehicular battery; for example, the VMS, motor controller, and engine control unit (ECU) Therefore, this design allows units to have common ground and facilitates control and communication among them As shown in Fig 2.12, we continue to use the TPS54160 to provide a stable power supply for the central controller

### 2.4.2 Battery Pack Voltage Measurement

As shown in Fig 2.13, to measure the high pack voltage, the first step is to use voltage dividers to linearly reduce the voltages of positive and negative battery poles below 5V It is noteworthy that the negative pole of the battery pack is not the ground of the central controller The two low voltages $V_{pos}$

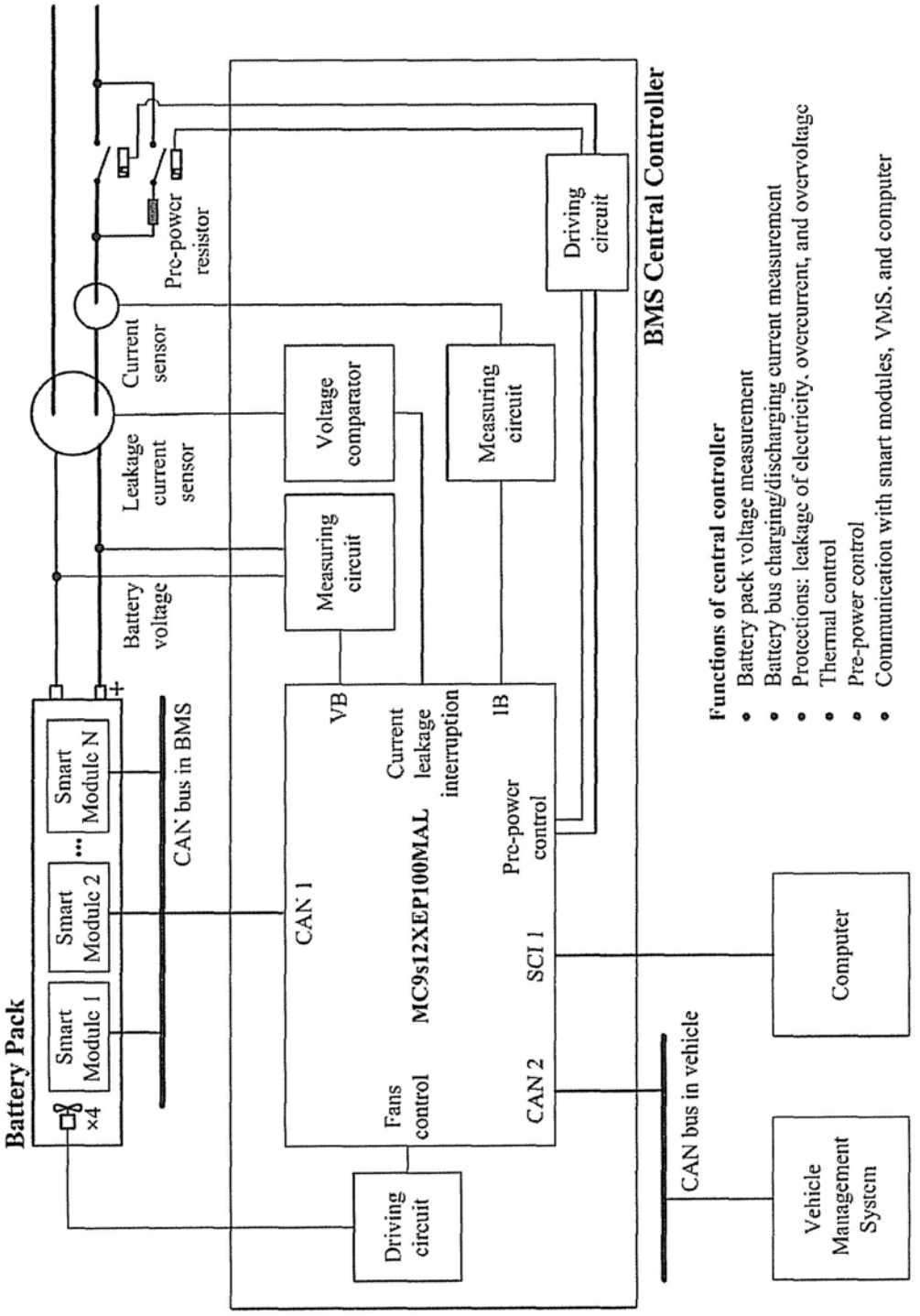


Figure 2.11: Structure and functions of central controller.

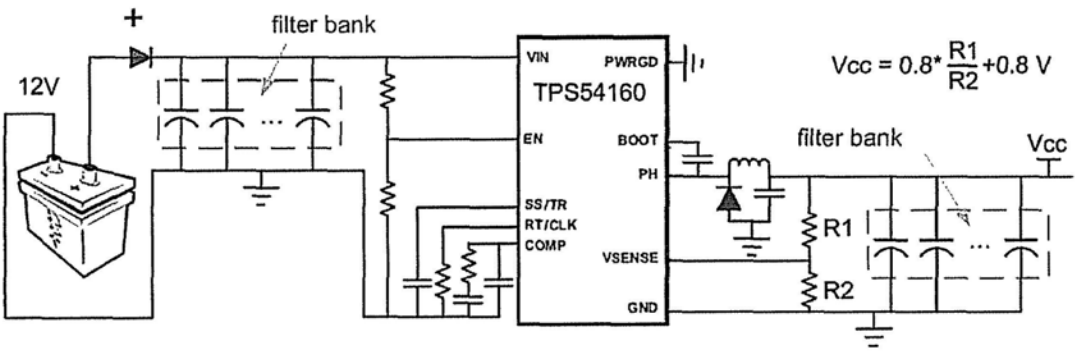


Figure 2.12: Schematic diagram of power supply for the central controller.

and $V_{neg}$ are respectively calculated as:

$$V_{pos} = \frac{R2}{R1+R2} \times V_{+} \qquad V_{neg} = \frac{R2}{R1+R2} \times V_{-} \tag{2.3}$$

where $V_{+}$ and $V_{-}$ are the voltages of the pack poles with respect to the ground of the controller. Then, a subtracter is applied to obtain the difference voltage $V_{pack}$ to be sent to the AD input port of the MCU, as expressed by:

$$V_{pack} = V_{pos} - V_{neg} = \frac{R2}{R1+R2} \times (V_{+} - V_{-}) \tag{2.4}$$

The selection of R1 and R2 depends on the voltage of the battery pack, making sure $V_{pack}$ is below 5V to avoid damage to the MCU.

### 2.4.3 Battery Pack Current Measurement

The hall effect current sensor HTFS200-P/SP2 [35] is applied to convert the current in ±300A to the voltage in $2.5 \pm 1.875$V, as expressed by

$$V_{out} = 2.5 + 1.25 \times \frac{I}{200} \quad (V) \tag{2.5}$$

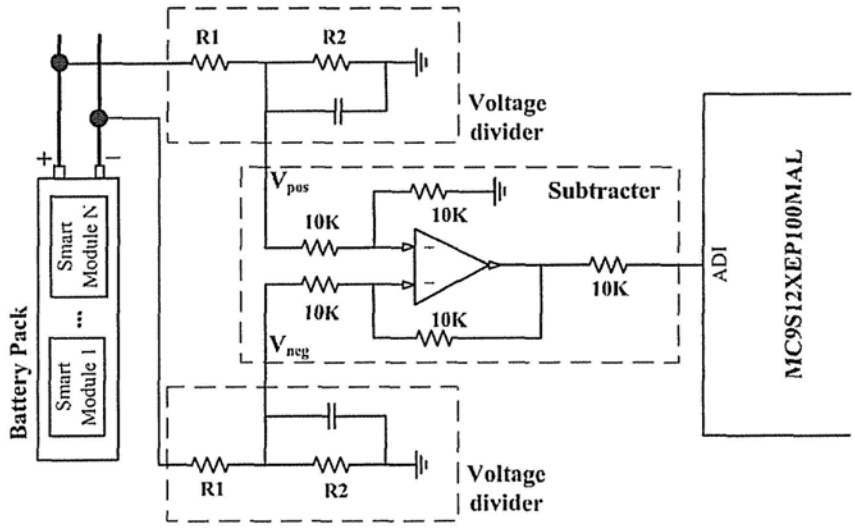


Figure 2.13: Schematic diagram of pack voltage measurement.

where $I$ is the pack current to be measured and $V_{out}$ is the output voltage.

To decrease output impedance and isolate the central controller from the sensor fixed on the power bus, $V_{out}$ is sent to the AD input port via a follower, as shown in Fig. 2.14.

### 2.4.4 Leakage Current Measurement

When current leakage occurs, a small amount of current goes to the vehicle body or the ground, making the current on the battery's positive pole different from that on the negative pole. Measurement of the small current difference allows detection of current leakage.

The CYCT04-M20B current sensor family is based on a magnetic modulation and compensation principle, and can be used for measurement of small DC current and leakage current, a current difference between two or more conductors [42]. Leakage current is bidirectional. The sensor linearly

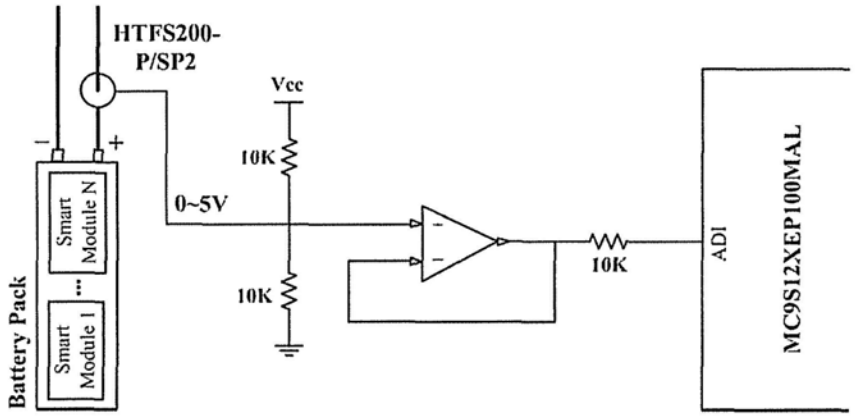


Figure 2.14: Schematic diagram of pack current measurement.

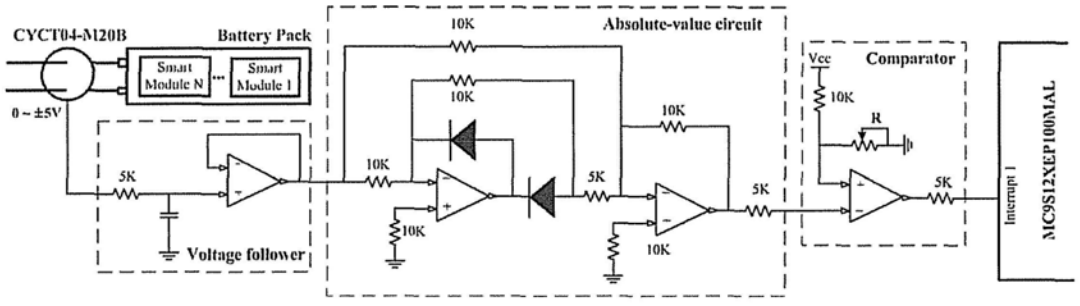


Figure 2.15: Schematic diagram of leakage current measurement.

converts the leakage current in $\pm 50mA$ to the output voltage $\pm 5V$.

As shown in Fig. 2.15, the output voltage of the sensor first goes through a voltage follower to decrease output impedance and isolate the central controller from the sensor. Then, an absolute-value circuit is applied to convert the voltage in $\pm 5V$ to 0-5V. This is because the current leakage is only related to the value, but not the direction, of the leakage current. Finally, a comparator is designed to produce an interruption signal if the measured voltage is higher than the reference voltage determined by the sliding resistor $R$. In this work, $R$ is selected to produce interruption if the value of the leakage current is greater than 30mA.

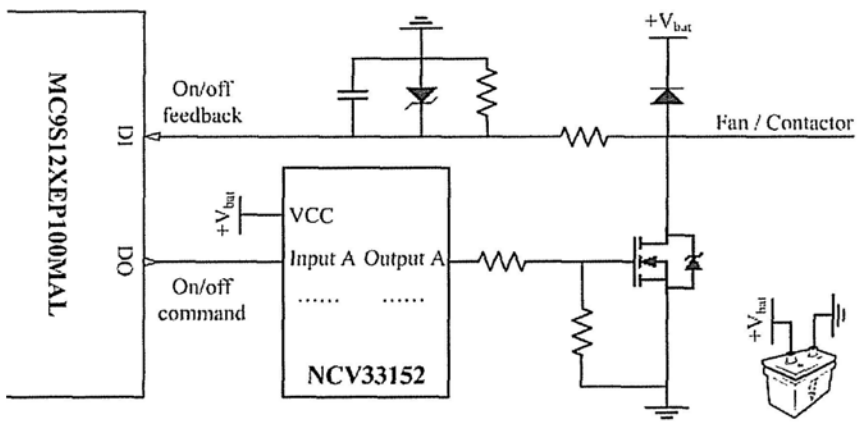


Figure 2.16: Schematic diagram of driving circuit of fans and contactors.

### 2.4.5 Driving Circuit of Fans and Contactors

Fans and contactors are applied to control the battery package temperature and the on/off of the power bus, respectively. To drive fans and contactors, the driving circuit shown in Fig. 2.16 is applied for each channel. NCV33125, the dual high speed MOSFET driver, is applied to drive an actuator via a MOSFET [43]. Since the power of fans and contactors is higher than the driving ability of the controller, we directly use the 12V vehicle battery for the power source. In addition, to measure the states of fans and contactors, each channel is also fed back to the MCU.

### 2.4.6 Implementation

Fig. 2.17 shows the photograph of the implemented central controller. Its size is 120mm*95mm*11.6mm, with four layers; as it is the same width and height as those of the modules, assembly is easy.

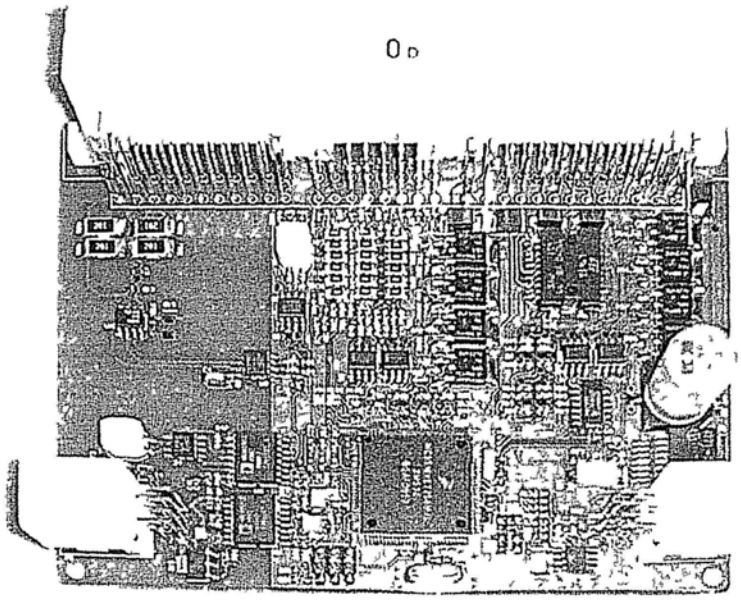

Figure 2.17 Photograph of the implemented central controller

## 2.5 Battery Pack with Battery Management System

To validate the feasibility of the proposed BMS and establish a platform to study the proposed SoC estimation, cell equalization, and fast charging algorithms in the following chapters, a battery pack with the BMS has been developed.

The pack consists of 2.3Ah LiFePO4 cells, which have ordinary performance including charge/discharge ability, internal resistance, cell consistency and so forth. The aim of selecting this pack is to demonstrate the efficiency of our proposed BMS and various algorithms under general conditions.

Extension of capacity and increase of voltage are usually two necessary requirements for establishing a vehicular battery. Extension of capacity is

implemented by connecting cells in parallel, while increase of voltage is implemented by connecting cells in series. In this case, two pack architectures are possible. The first approach, called a series cell module, builds the pack by firstly wiring the cells in series for increased voltage, and then connecting the high voltage strings in parallel for extension of capacity. In contrast, the second method, called a parallel cell module, creates the pack by first wiring cells in parallel and then connecting the large capacity strings in series. We follow the second approach in this work, with the advantage that the parallel-connected cells can be recognized as a new capacity-extended cell, and no further investigation and control are needed to manage the cells inside. The parallel cells will naturally have the same voltage, equal to an embedded cell equalization function based on voltage. In addition, the capacity-extended cell can be modeled as a whole, with larger capacity and smaller internal resistance than the individual cells.

As shown in Fig. 2.18, three cells are parallel-connected to form a new capacity-extended 6.9Ah cell, then eight new cells are series-connected to form a smart module managed by a module controller. In the module controller, each AD7280 investigates four new cells. Finally, two smart modules are series-connected to form the battery pack controlled by a central module. The capacity-extended cell and the final battery pack are shown in Fig. 2.19.

## 2.6 Test Platforms and Application

To test and demonstrate the availability of the implemented BMS system and verify the efficiency of the algorithms for SoC estimation, cell equaliza-

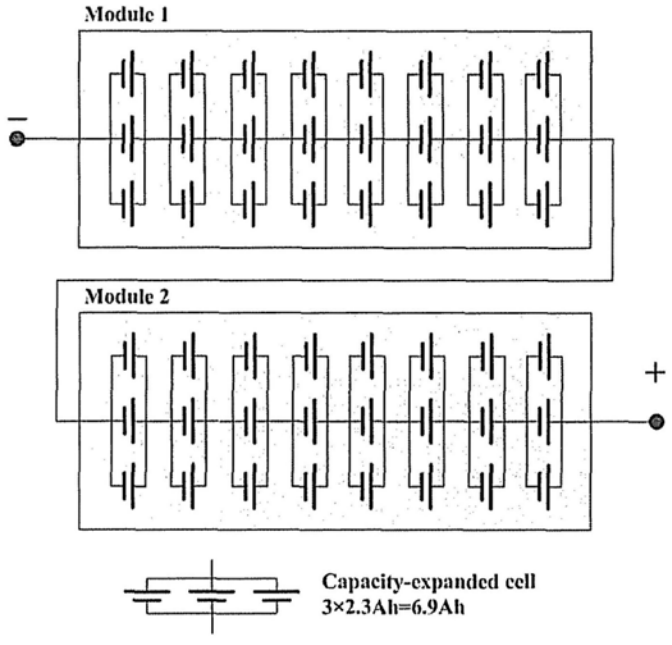


Figure 2.18: Grouping architecture of the applied battery pack.

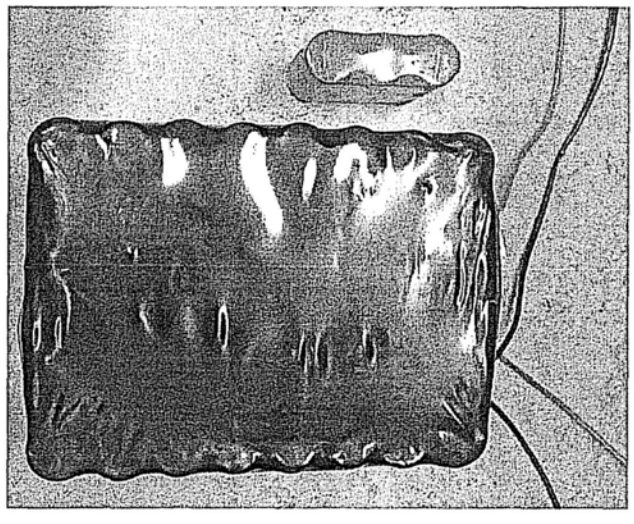

Figure 2.19: The capacity-extended cell and battery pack used in this work.

tion, and fast charge proposed in the following chapters, three platforms are applied in this thesis.

### 2.6.1 Simulation Platform: Advisor

The advanced vehicle simulator (Advisor), developed by scientists at the National Renewable Energy Laboratory (NREL), is a software portfolio based on the MATLAB/Simulink software environment for modeling various conventional, pure electric, hybrid electric powertrains, and for predicting their effects on user-specified vehicle configurations, such as economy and emissions.

As shown in Fig. 2.20, Advisor provides the simulation for almost every component used in electric vehicles, including the battery, engine, motor, generator, torque coupler and so on. Given a specified vehicle configuration, with correct setup of parameters, the simulator will automatically generate the charge and discharge current to the battery system, and hence lead to changes in variables such the terminal voltage of the battery, SoC, temperature, and so forth. In addition, the battery models in Advisor are based on real data tested by NREL, which makes the simulation of the battery system more reliable and realistic. In this thesis, all of the simulation studies are based on Advisor.

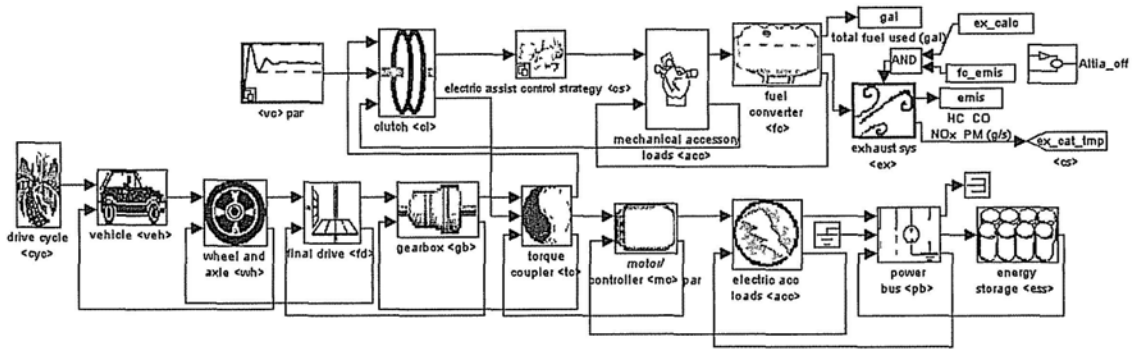


Figure 2.20: Simulation system in Advisor for a parallel HEV (Source: Advisor).

### 2.6.2 Experimental Platform: Programable Electric Loader and Charger

To further demonstrate the proposed methods, we establish an experiment based on a programmable electric loader and charger. The loader is IT8512C, with high performance and an affordable single channel DC electronic load. The high resolution voltage 1mV, current 0.1mA measurement system provides both accuracy and convenience for our battery testing [44]. The charger IT6154 is a single output programmable power supply with 0.1mV, 0.01mA high resolution, and high rise speed of 20ms [45].

Since the focus of our research is the estimation and investigation at cell level, the experimental platform is applied for modeling, testing, and verification of algorithms for the cells or extended cells. The experimental environment is shown in Fig. 2.21.

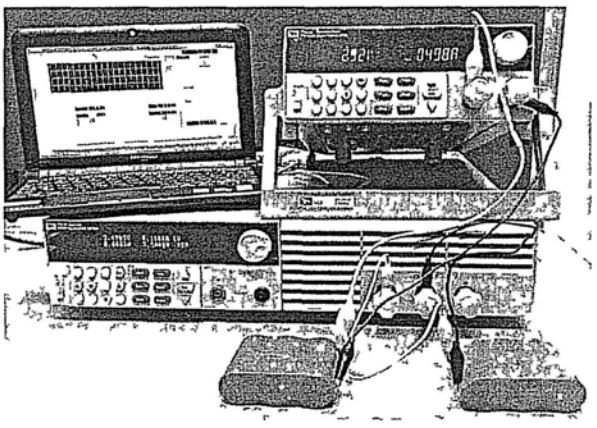

Figure 2 21 The experimental environment using programable electric loader and charger

Figure 2 22 The series hybrid electric vehicle developed by our lab

### 2.6.3 Application: Series Hybrid Electric Vehicle

To apply the battery pack with the proposed BMS in practice, the whole system is implemented in the series hybrid electric vehicle developed by our lab. A photograph is shown in Fig. 2.22.

This vehicle is equipped with an engine and a generator to supply electric power to the battery pack. Unlike traditional vehicles, this vehicle is driven by four in-wheel motors and steered by four independent steering motors. This design allows the functions of 4-wheel independent drive and 4-wheel independent steering. Since this thesis focuses on the BMS developed by myself, the details of this novel vehicle are not illustrated here. Interested readers can find a description in [7, 46, 47].

---

**□ End of chapter.**

# Chapter 3

# Robust State of Charge Estimation

## 3.1 Introduction

One of the fundamental vehicular states is the residual propulsive energy in vehicles, based on which drivers can estimate the left driving range. In conventional fuel-driven vehicles, the amount of gasoline or diesel residual in fuel tank is directly measured by a variable resistor which is connected to a floater. However, in electric vehicle, the propulsive energy becomes to be the charges residual inside battery pack. How to measure the left charges is a difficult problem in BMS design.

State of Charge (SoC), defined as the ratio of residual charge to the nominal full capacity, is the most fundamental state of a battery, working as the "fuel gauge" for conventional fuel-driven vehicles. Unfortunately, the crucial state is not directly measurable, essentially requiring a soft estimator to cal-

culate it. An accurate estimation result can indicate the amount of residual energy in a battery, inform users of the range available, and cooperate with the VMS to prolong the battery life cycle and achieve overall optimal energy efficiency. Therefore, SoC estimation has attracted wide coverage in both research and application in recent years, and has become one of the most significant but difficult issues in BMS design.

### 3.1.1 Literature Review

A comprehensive review of SoC estimation for general battery-powered applications has been studied by *Valer Pop et al.* [48]. However, limited by the special requirements for EV application, such as realtime estimation, avoidance of energy loss, and impossibility of injecting extra test signals during the vehicle in-service period, some typical, usually more accurate methods are impractical for estimating the battery SoC in EVs. These include, for example, Open Circuit Voltage (OCV) direct measurement, discharge test, measurement of electrolyte physical properties [49] and a.c. impedance spectroscopy [50, 51].

Coulomb counting (usually denoted as Ah method) is one of the most applicable SoC indicators, which simply accumulates the charge transferred in or out of the battery. Recently, some advanced techniques have been proposed to enhance its performance by on-line estimation of charge/discharge efficiencies [52, 53]. Essentially, coulomb counting is a type of open-loop estimator that requires accurate measurement of the battery current. It will accumulate current noise and has no ability to self-correct. If the mean of noise is non-zero, that is, if zero-drift is present, the estimation result reaches

divergence.

Model-based methods have also been well studied, aiming to establish a closed-loop estimation based on a battery model. Battery models usually apply current as a control input, terminal voltage as measured output, and SoC, State of Health (SoH) and/or equivalent OCV as hidden states [54–58]. An extended Kalman filter (EKF) was first utilized to estimate these hidden states according to realtime sampling data of the current and terminal voltage [59], and was then further improved by enhancement strategies such as reduced order EKF [60], augmented states EKF [61], adaptive EKF [62], and Sigma-point KF [63, 64]. These model-based methods require the battery model to be accurate., And it will be better that the model parameters have obvious physical meanings to facilitate identification of the parameters and analysis of the model's behavior. In addition, model-based methods are also sensitive to noise properties. Noise reduction is necessary before estimation. A sliding model observer was utilized to compensate the modeling errors and uncertainties [65, 66]. However, the selection of parameters in a sliding model observer, such as the boundaries of uncertainties and switching gains, still depends on a comprehensive understanding of battery dynamics. Moreover, a set of unsuitable parameters runs the risk of causing the chattering phenomena [66].

To avoid the difficulty of battery modeling and identification, machine learning strategies were also introduced to establish black-boxes mapping measurable data to SoC, including Neural Network (NN) [67], fuzzy NN [68, 69], evolutionary NN [70, 71] and support vector machine [72, 73]. These data-oriented methods inevitably suffer from intrinsic problems, such as large

numbers of train data covering the whole possible range of operation, the selection of a model structure, and the balance between under-fitting and over-fitting. Meanwhile, the estimation result is theoretically unpredictable when it suffers from noise.

In recent years, some hybrid or combined estimation frameworks have been proposed to integrate the advantages of individual estimators with different characters. A combination of the RC and hysteresis models was proposed to compensate for the deficiencies of the individual models [74]. Coulomb counting and EKF based estimation were integrated to achieve better performance [75–77]. A very accurate result, whereby estimation error was less than 1 min in time left or 1% in SoC, was also obtained under the combined contributions of direct measurement of the electro-motive force and a book-keeping algorithm [78], though it was not specifically designed for EV application. The inspiring results reveal that the establishment of SoC estimation frameworks, which rationally consist of types of estimators, is a potential way of achieving more accurate and robust performance.

### 3.1.2 Overview of Proposed Framework

The real vehicle driving environment often involves interference sources which cause signal measurement noise and even zero drift. Meanwhile, the strong time-variant properties of batteries makes it difficult to establish a sufficiently accurate linear model to estimate and predict batteries' dynamic behavior. In other words, the non-ideal working conditions make it hard to satisfy the prerequisites of most individual SoC estimators.

Therefore, to guarantee estimation accuracy in the real driving process,

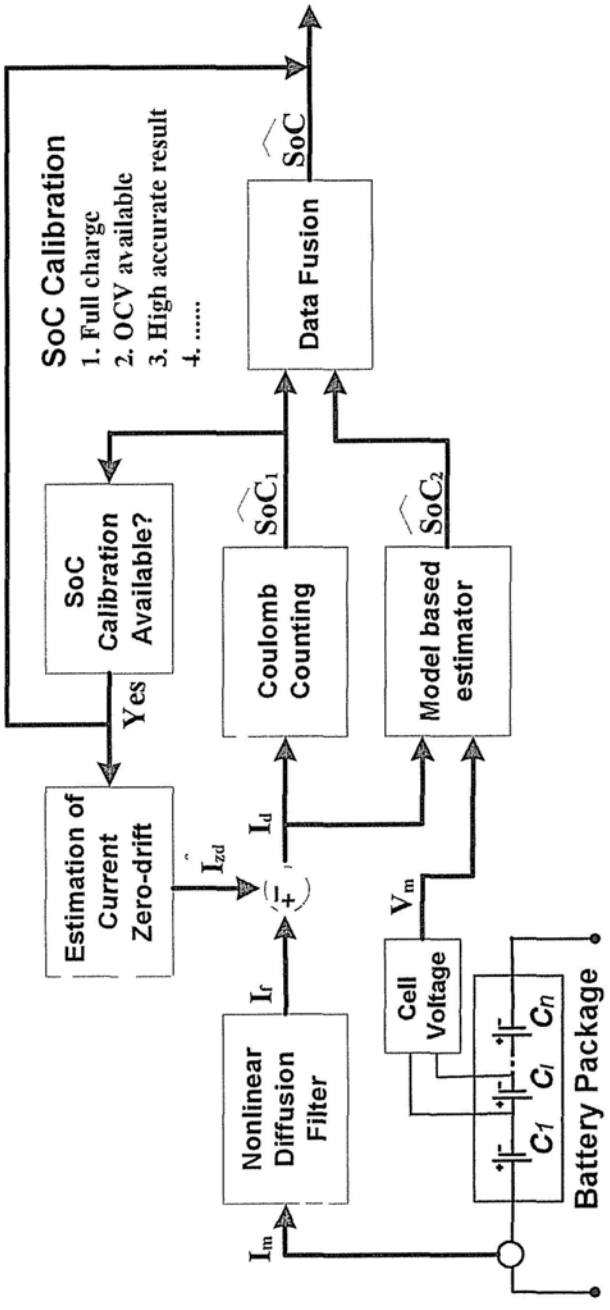


Figure 3 1 The proposed robust SoC estimation framework

it is necessary to improve the anti-noise abilities, or robustness, of SoC estimation techniques. In this paper, we have proposed a robust estimation framework, as shown in Fig.3.1, which consists of:

1. A nonlinear diffusion filter to reduce current measurement noise, where $I_m$ is the measured current and $I_f$ is the filtering result.

2. A current zero-drift estimator to remove the zero-drift, where $\widehat{I_{zd}}$ is the estimated zero-drift of current measurement and $I_d = I_f - \widehat{I_{zd}}$ is the denoised result.

3. A coulomb counting estimator to implement open-loop estimation $\widehat{SoC}_1$.

4. A model based estimator to realize closed-loop estimation, where $V_m$ is the measured terminal voltage and $\widehat{SoC}_2$ is the estimated result.

5. A data fusion component to achieve the final estimation $\widehat{SoC}$ by integrating $\widehat{SoC}_1$ and $\widehat{SoC}_2$.

Section 3.2 firstly analyzes the quasi-random property of battery current in driving process, and then applies nonlinear diffusion filter to achieve better noise reduction performance than linear digital filter and wavelet based filter. In Section 3.3, based on the estimation error of coulomb counting method obtained at each SoC calibration available time, a self-learning strategy is proposed to estimate the zero-drift of current measurement. In Section 3.4, we introduce $H_\infty$ filter to robustly estimate SoC and conduct simulations to compare performance with conventional EKF. In Section 3.5, the enhanced self-correction model has been modified to establish an accurate model for the

applied LiFePO4 battery and EKF is utilized to estimate SoC in experiments and application. Conclusions and future studies are outlined in Section 3.6.

## 3.2 Current Denoising Using Nonlinear Diffusion Filter

A battery is a typical less-information system, where a complex multi-parameter electrochemical reaction occurs inside, while only terminal voltage, bus current and surface temperature can be measured outside. SoC, one of the internal states, has to be estimated according to the limited external variables. Thus, the measurement accuracy of these variables is crucial for SoC estimation.

### 3.2.1 Property Analysis of Current Measurement

A vehicular battery pack usually consists of tens, even hundreds, of series/paralle connected cells to generate a large charge/discharge current varying in ±300A [15]. However the precision of commercialized current sensors is around ±1%, resulting in a maximum error of $\pm 3A$. The error is non-ignorable for SoC estimation. Moreover, although the peak current can reach 300A, the current is normally less than 100A, thus the $\pm 3A$ noise represents a comparatively large percentage.

Another distinct difficulty is that the current signal possesses a quasi-random property, which leads to the failure of traditional filters. Fig.3.2 illustrates a typical current profile of a Prius driving on a UDSS cycle, which

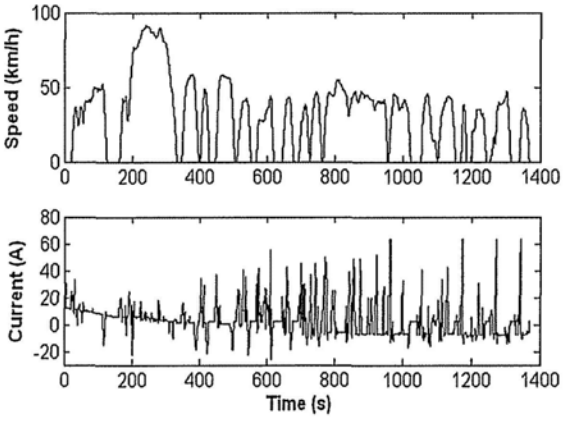


Figure 3.2: Current profile of Prius driving on cycle UDDS.

is simulated by Advisor. Battery current is determined by the demand from the motor and/or generator, and primarily depends on driving behavior. The way a vehicle is driven is limited by road conditions and may be disrupted by various unexpected events, such as traffic jams, braking to avoid pedestrians, sudden acceleration when overtaking, and so forth. Such erratic driving will inevitably result in quasi-random current on the power bus. Analysis of the frequency domain further depicts the property of the battery current, as shown in Fig.3.3. The current signal, with 100Hz sampling frequency, expands across the whole frequency domain and it is hard to determine a cut-off frequency that separates signal from noise.

Noise reduction essentially requires some kind of property difference between signal and noise. As discussed above, the similar frequency properties of current signal and noise causes difficulty in applying traditional filters, e.g. low-pass filters, to isolate noise.

The variation in real current signal is caused by driving behavior, which

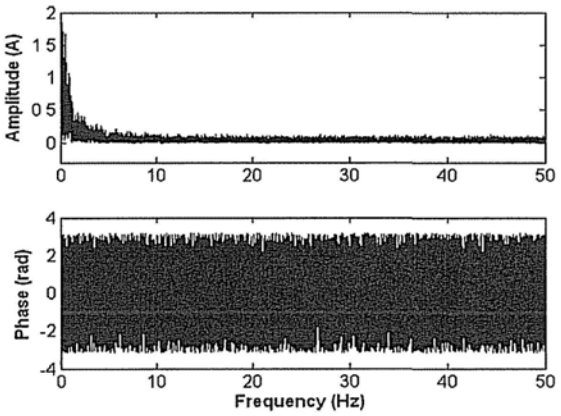


Figure 3.3: Frequency analysis of current profile of Prius driving on cycle UDDS.

usually leads to a comparatively large degree of change. However, current noise is often produced by the precision of measurement units, electromagnetic interference, vehicle vibrations and so on, which typically varies in a small range.

According to experiments, we find that the noise in current measurement is continues within a limited region. In addition, the noise is time-independent. Therefore, in this work, we assume the noise has Gaussian distribution with a fixed standard deviation and a nonzero mean.

Under this assumption, it is clear that large current variation caused by driving behavior possesses higher signal-noise-ratio (SNR). The filtering of current measurement is purposely designed to improve the measurement with low SNR and keep the measurement with high SNR. Based on the above analysis, we apply a nonlinear diffusion filter to reduce noise.

### 3.2.2 Nonlinear Diffusion Filter

Nonlinear Diffusion Filter (NDF) was firstly proposed in the image processing field to nonlinearly eliminate the oscillation in a small range while retaining the variation in a larger range [79].

Denoting $k$ and $i$ as the discrete time and iteration index, the iterative equation of the nonlinear diffusion filter is described as

$$\begin{aligned} I(k,i+1) = I(k,i) + \Delta t \times c_l(k,i) \times [I(k-1,i) - I(k,i)] \\ +\Delta t \times c_r(k,i) \times [I(k+1,i) - I(k,i)] \end{aligned} \tag{3.1}$$

where initial iteration $I(k,1)$ is set as the measured data sequence $I_m(k)$, the last iteration $I(k,N)$ is the filtering result $I_f(k)$, and $N$ is the iteration time.

As an iterative step, a large $\Delta t$ stands for a long diffusion period in each iteration, leading to smoother results, but with the risk of an unstable iteration process. In contrast, a too small $\Delta t$ causes a slow diffusion process, requiring more iterations to achieve a satisfactory result.

$c_l(k,i)$ and $c_r(k,i)$, generally denoted by $c(k,i)$, are the left and right diffusion coefficients respectively, which control the degree of smoothing for values between the $k$th datum and its left or right neighbor. The smaller $c(k,i)$ is, the harder it is to smooth. As discussed above, a large change in current has a high possibility of being with large SNR, while a small change usually possesses low SNR. Thus, we set $c(k,i)$ to be inversely proportioned to the signal difference, using the conventional equation:

$$c_l(k,i) = \frac{1}{1 + \left[\frac{I(k-1,i) - I(k,i)}{\kappa}\right]^2} \tag{3.2}$$

and

$$c_r(k,i) = \frac{1}{1+\left[\frac{I(k+1,i)-I(k,i)}{\kappa}\right]^2} \tag{3.3}$$

where $\kappa$ is the gradient modulus threshold that controls the conduction.

### 3.2.3 Adaptive-$\kappa$ Strategy

Equations (3.2) and (3.3) indicate that the performance of the nonlinear diffusion filter depends on the selection of $\kappa$. In general, a noisy signal with low Signal-Noise-Ratio (SNR) requires a large $\kappa$ to enhance the smoothing effect. However, the SNR of a noisy signal is an unknown value and has to be estimated indirectly. Based on the characteristics of battery current, an adaptive $\kappa$ selection method is proposed using the following steps.

1. Calculate the differential signal $\Delta I_m(k)$ of the original signal $I_m(k)$, where the duration between $k$ and $k+1$ is the sampling period.

$$\Delta I_m(k) = I_m(k+1) - I_m(k) \tag{3.4}$$

2. Establish the set $\Delta_s$ in which the absolute values of differential signal are smaller than 5A. The reason to remove higher differential data is that they are likely caused by driving behavior, i.e. the real current change.

$$\Delta_s = \{\Delta I_m(k) \mid |\Delta I_m(k)| < 5\} \tag{3.5}$$

3. Calculate the standard deviation $std(\Delta_s)$ of the elements in set $\Delta_s$. To some extent, $std(\Delta_s)$ is an indicator of the SNR of signal. The smaller

$std(\Delta_s)$ is, the larger SNR is.

4. Adaptively determine $\kappa$ according to $std(\Delta_s)$. In this study, we first fix the iteration time $N = 20 \times f_s$ ($f_s$ stands for sampling frequency) and the iterative step $\Delta t = 0.6$, then the relationship between $\kappa$ and $std(\Delta_s)$ is experimentally determined by the below piecewise function.

$$\kappa = \begin{cases} \min(std(\Delta_s)/10, 2) & std(\Delta_s) > 2.2 \\ \max(std(\Delta_s) \times 1.76 - 3.652, 0) & std(\Delta_s) < 2.2 \end{cases} \tag{3.6}$$

Remark: As the nonlinear diffusion filter requires the right neighbors (future data) to smooth the current datum, the filter has to delay for a period. In this work, the iteration time $N = 20 \times f_s$ will result in 20 seconds delay, which is short enough to be negligible because SoC changes slowly.

### 3.2.4 Performance Comparison

To demonstrate the efficacy of the nonlinear diffusion filter with adaptive-$\kappa$ strategy, performance is compared with the traditional lowpass filter and wavelet filter. The lowpass filter is implemented using the Butterworth method with cutoff frequency $f_{cut} = 0.9 \times (f_s/2)$ determined by trial-and-error. The wavelet filter uses level-dependent thresholds determined by the Birge-Massart strategy [80].

The current profiles are produced by Advisor. We select the well-developed "Prius_jpn" vehicle model and three typical driving cycles: the highway "HWFET", the suburban "WVUSUB", and the urban "MANHATTAN". The current signal is corrupted by white noise with SNR from 0dB to 20dB.

The performance index of the Reduced Root-Mean-Square of Errors (RRMSoE) is defined below.

$$RRMSoE[A] = rms(I, I_m) - rms(I, I_f) \tag{3.7}$$

and

$$RRMSoE[\%] = \frac{rms(I, I_m) - rms(I, I_f)}{rms(I, I_m)} \times 100\% \tag{3.8}$$

where

$$rms(I_1, I_2) = \sqrt{\frac{1}{L}\sum_{i=1}^{L}(I_1(i) - I_2(i))^2} \tag{3.9}$$

$I$, $I_m$ and $I_f$ are the real current, measured noisy current and filtering result respectively, $L$ is the length of data.

As an example, Fig 3.4 illustrates the HWFET case with 15dB SNR noise. The top subfigure describes the real current signal and noise signal. It is clear that the real signal has larger variance. Added noise appears as burrs. The errors of the filtering results are given in the bottom subfigure. Without doubt, the lowpass filter gives poor performance, even worse than the noisy signal, because it simultaneously removes the real signal in the high frequency zone. Basically, any frequency based filter will have difficulty handling this problem. The wavelet filter, focusing on both scale and time, performs better than the lowpass filter but still fails to keep the large variation in the real signal. The nonlinear diffusion filter successfully removes the noise appearing as burrs while keeping the real signal with large variation in morphology.

The total results are given in Tab. 3.1, where each value is the average of 100 independent random tests. It is clear that the adaptive-$\kappa$ strategy

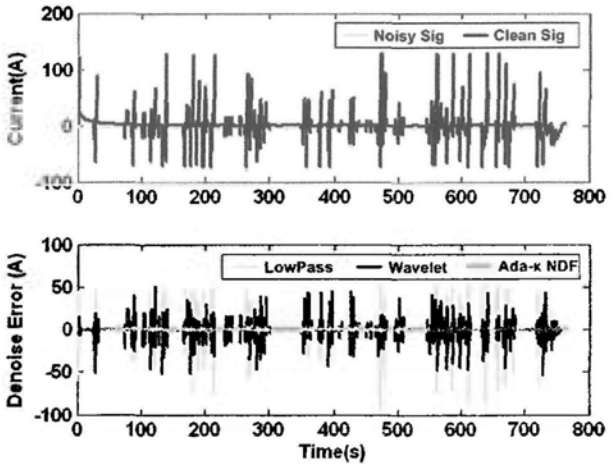


Figure 3.4: Filtering results of HWFET current profile corrupted by noise with 15dB SNR.

efficiently estimates the equivalent SNR in each case and hence calculates a suitable $\kappa$ to achieve satisfactory denoising.

## 3.3 Current Zero-Drift Reduction using Learning

Although the nonlinear diffusion filter has the ability to remove the oscillatory noise, it cannot handle the zero-drift problem which causes the baseline shift. Zero-drift, actually the non-zero mean of noise, is the source of divergent results in coulomb counting, which negatively affects the performance of other estimators.

In this section, we propose a self-learning strategy to estimate the zero-drift of current measurement. To establish the self-learning system, it is necessary to know the estimation error, equally the real SoC. In practice, the true value of the SoC can be obtained when (1) the battery is fully charged,

Table 3.1: Reduced RMS of denoising errors based on different filters.

| SNR [dB] | Highway(HWFET) | | | | | | Suburban(WVUSUB) | | | | | | Urban(MANHATTAN) | | | | | |
|---|---|---|---|---|---|---|---|---|---|---|---|---|---|---|---|---|---|---|
| | Lowpass | | Wavelet | | Ada-$\kappa$ NDF | | Lowpass | | Wavelet | | Ada-$\kappa$ NDF | | Lowpass | | Wavelet | | Ada-$\kappa$ NDF | |
| | [A] | [%] | [A] | [%] | [A] | [%] | [A] | [%] | [A] | [%] | [A] | [%] | [A] | [%] | [A] | [%] | [A] | [%] |
| 0 | -2.05 | -21.98 | 2.98 | 31.95 | **5.53** | **59.41** | 0.00 | -0.04 | 4.82 | 52.09 | **6.68** | **72.15** | -0.14 | -1.22 | 5.57 | 49.58 | **6.76** | **60.23** |
| 2 | -2.62 | -35.47 | 1.57 | 21.26 | **4.11** | **55.53** | -0.24 | -3.29 | 3.85 | 52.35 | **5.33** | **72.53** | -0.43 | -4.83 | 4.33 | 48.50 | **5.77** | **64.69** |
| 4 | -3.14 | -53.41 | 0.41 | 7.02 | **2.82** | **47.93** | -0.44 | -7.58 | 3.07 | 52.52 | **4.04** | **69.25** | -0.70 | -9.85 | 3.27 | 46.15 | **4.32** | **60.94** |
| 6 | -3.77 | -80.85 | -0.58 | -12.34 | **1.86** | **39.84** | -0.67 | -14.52 | 2.42 | 52.15 | **2.99** | **64.44** | -0.99 | -17.66 | 2.35 | 41.75 | **3.10** | **55.14** |
| 8 | -4.24 | -114.45 | -1.42 | -38.27 | **1.08** | **29.03** | -0.91 | -24.73 | 1.88 | 51.01 | **2.18** | **59.30** | -1.33 | -29.67 | 1.53 | 34.28 | **2.11** | **47.13** |
| 10 | -4.73 | -160.50 | -2.11 | -71.68 | **0.71** | **24.00** | -1.16 | -39.61 | 1.44 | 49.30 | **1.58** | **54.08** | -1.63 | -45.89 | 0.86 | 24.24 | **1.44** | **40.53** |
| 12 | -5.16 | -220.51 | -2.67 | -114.30 | **0.70** | **29.84** | -1.40 | -60.15 | 1.06 | 45.47 | **1.29** | **55.32** | -1.96 | -69.49 | 0.28 | 10.00 | **1.06** | **37.72** |
| 14 | -5.51 | -296.75 | -3.12 | -168.11 | **0.94** | **50.74** | -1.63 | -88.11 | 0.72 | 39.25 | **1.20** | **64.90** | -2.24 | -100.18 | -0.21 | -9.19 | **0.93** | **41.54** |
| 16 | -5.81 | -393.55 | -3.49 | -236.44 | **0.80** | **54.51** | -1.84 | -125.45 | 0.43 | 29.53 | **0.93** | **63.17** | -2.52 | -141.40 | -0.63 | -35.24 | **1.00** | **56.34** |
| 18 | -6.07 | -517.99 | -3.78 | -322.74 | **0.63** | **53.77** | -2.03 | -174.06 | 0.18 | 15.67 | **0.73** | **62.35** | -2.76 | -195.17 | -0.96 | -67.62 | **0.76** | **53.99** |
| 20 | -6.28 | -674.39 | -4.02 | -431.19 | **0.49** | **52.57** | -2.20 | -237.73 | -0.02 | -2.45 | **0.57** | **62.03** | -2.96 | -263.57 | -1.23 | -109.44 | **0.59** | **52.19** |

(2) OCV is available, or (3) a more accurate result is somehow obtained. In these calibration-available moments, we can not only reset SoC estimation but also calculate zero-drift using the error of coulomb counting, as deduced in the following.

### 3.3.1 Estimation of Current Zero-Drift

The discrete recursive equation of coulomb counting is described as:

$$\widehat{SoC}_1(k) = \widehat{SoC}_1(k-1) + \frac{I_d(k)\eta(k)T_s}{Q_{full}} \tag{3.10}$$

where $\widehat{SoC}_1(k)$ is the estimated SoC at time $k$, $I_d(k)$ is the "denoised" current, $Q_{full}$ is the charge stored in the fully-charged battery, and $T_s$ is the sampling period. $\widehat{SoC}_1(0)$ is initialized by the SoC-OCV mapping table or other advanced methods at each start time, or is reset to the true value at each calibration-available time.

$\eta(k)$ is the coulombic efficiency or ampere-hour efficiency. Strictly speaking, it is a time-variant parameter, depending on temperature, SoC and other relative states. The basic way of determining coulombic efficiency is to establish its value table according to the manufacturers' datasheets or testing data [81]. The mass utilization of coulomb counting in practical applications has demonstrated its feasibility and validity. In addition, adaptive learning and on-line estimation strategies can strengthen the accuracy of coulombic efficiency estimation [52,53,75]. Moreover, since the accuracy of the coulomb counting primarily depends on measurement of the battery current and estimation of the initial SoC [53], the error of coulombic efficiency will not be

covered in this paper.

To analyze the zero-drift of current measurement, we denote the true value of current as $I(k)$, the residual noise affecting the coulomb counting estimator as $I_n(k)$, and the true value of SoC as $SoC(k)$. The "denoised" current accumulated in the coulomb counting method is expressed by

$$I_d(k) = I(k) + I_n(k) \tag{3.11}$$

and

$$\begin{aligned}
\widehat{SoC}_1(k) &= \widehat{SoC}_1(k-1) + \frac{I_d(k)\eta(k)T_s}{Q_{full}} \\
&= \widehat{SoC}_1(0) + \frac{\sum_{i=0}^{k} I_d(k)\eta(i)T_s}{Q_{full}} \\
&= \widehat{SoC}_1(0) + \frac{T_s\left(\sum_{i=0}^{k} I(i)\eta(i) + \sum_{i=0}^{k} I_n(i)\eta(i)\right)}{Q_{full}} \\
&= \left(\widehat{SoC}_1(0) + \frac{T_s\sum_{i=0}^{k} I(i)\eta(i)}{Q_{full}}\right) + \frac{T_s\sum_{i=0}^{k} I_n(i)\eta(i)}{Q_{full}}
\end{aligned} \tag{3.12}$$

Since $\widehat{SoC}_1(0)$ is initialized at each start time by the SoC-OCV mapping table or advanced algorithms, or is reset to the "true" value at each calibration-available moment, its error is small enough to be ignored within the tolerance range. Therefore we have

$$\widehat{SoC}_1(0) = SoC(0) \tag{3.13}$$

$$\widehat{SoC}_1(k) = SoC(k) + \frac{T_s\sum_{i=0}^{k} I_n(i)\eta(i)}{Q_{full}} \tag{3.14}$$

$$E\left(\widehat{SoC}_1(k) - SoC(k)\right) = E\left(\frac{T_s \sum_{i=0}^{k} I_n(i)\eta(i)}{Q_{full}}\right) = \frac{T_s \sum_{i=0}^{k} \eta(i)}{Q_{full}} E\left(I_n(i)\right) \tag{3.15}$$

At each calibration-available time $k^*$, the true value $SoC(k^*)$ is available, thus

$$\widehat{SoC}_1(k^*) - SoC(k^*) = \frac{T_s \sum_{i=0}^{k^*} \eta(i)}{Q_{full}} E\left(I_n(i)\right) \tag{3.16}$$

The zero-drift of current measurement $\widehat{I_{zd}}$ is the mean of noise:

$$\widehat{I_{zd}} = E\left\{I_n(i)\right\} = \frac{Q_{full}\left[\widehat{SoC}_1(k^*) - SoC(k^*)\right]}{T_s \sum_{i=0}^{k^*} \eta(i)} \tag{3.17}$$

At each calibration available moment, $\widehat{I_{zd}}$ is updated by equation (3.17), which enables online tracking of zero-drift.

### 3.3.2 Performance Comparison

To demonstrate availability and efficacy, simulations based on Advisor have been conducted to track SoC when the Prius drives on the cycles HWFET, WVUSUB, MANHATTAN, NEDC, US06, and NYCC, successively. After completion of each cycle, a half-hour stop allows the battery OCV to be determined. When the vehicle starts a new driving cycle, SoC is reset to the real value and the algorithm re-estimates zero-drift. The SNR of current measurement is set to 0dB. The zero-drift $I_{zd}$ is set to 0.5A in the 1st-3rd cycles and 1A in the 4th-6th cycles. BMS firstly de-noises the current by ada-$\kappa$ NDF and then removes the zero-drift by subtracting the estimation

value $\widehat{I_{zd}}$.

Fig. 3.5 shows the SoC tracking results, comparing performance either using or not using the zero-drift self-learning strategy. Tab. 3.2 summarizes the numerical indexes of each cycle, including the average (ave) of absolute SoC estimation errors and the standard deviation (std) of errors in each cycle. Since we have no prior knowledge about zero-drift, its estimation value is set to 0 in the first driving cycle, HWFET; it therefore achieves the same SoC tracking performance as the conventional method. In the following two cycles, OCV is available at each start time to calibrate the SoC and to calculate the estimation error of the previous cycle, which allows $\widehat{I_{zd}}$ to update. The estimation values of zero-drift are 0.4895A and 0.4952A respectively, which are very close to the real zero-drift of 0.5A. Thus, the estimation error of the proposed method is clearly smaller than the conventional algorithm. In the 4th cycle, the real zero-drift is changed to 1A, with the aim of testing the self-adaptive ability of the learning strategy. As the learning strategy determines zero-drift by using the error in the previous cycle, the one-cycle delay means that $\widehat{I_{zd}} = 0.4987$ cannot fully compensate the real 1A drift, resulting in nonconvergent SoC estimation. In the following cycles, the large error updates the $\widehat{I_{zd}}$ to be 0.9863 and 0.9967 in the 5th and 6th cycles respectively. The self-adaptive ability leads to satisfactory performance in the last two cycles.

Although the proposed framework significantly improves on the performance of the conventional coulomb counting method, it is inherently an open loop estimator which does not take the measurable voltage into consideration. It only self-corrects estimation results at calibration moments but can

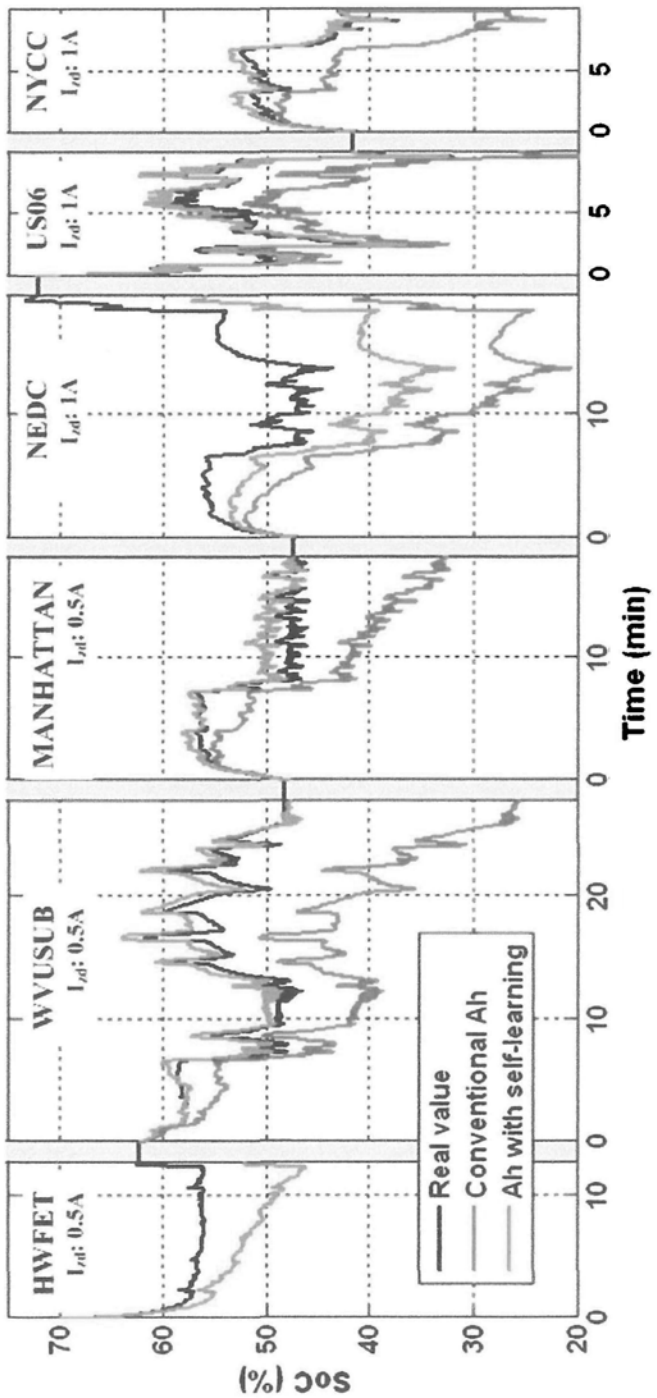


Figure 3.5: SoC estimation results based on conventional coulomb counting and the proposed coulomb counting with self-learning strategy.

The gray bars between cycles represent half-hour stops which allow OCV available. Simulation conditions: white noise with 0dB SNR, zero-drift 0.5A for the 1st-3rd cycles and 1A for the 4th-6th cycles.

Table 3 2 Numerical results of SoC tracking using or not using self-learning strategy (unit [%])

| SoC estimation methods | HWFET | | WVUSUB | | MANHATTAN | | NEDC | | US06 | | NYCC | |
|---|---|---|---|---|---|---|---|---|---|---|---|---|
| | ave | std | ave | std | ave | std | ave | std | ave | std | ave | std |
| Conventional Ah | 4 71 | 2 71 | 9 87 | 6 22 | 6 20 | 4 04 | 16 21 | 9 36 | 7 74 | 4 36 | 7 16 | 4 86 |
| Ah with self-learning | 4 71 | 2 71 | 1 34 | 0 96 | 1 23 | 0 95 | 8 24 | 4 77 | 1 42 | 1 65 | 0 96 | 0 50 |

not revise errors during the driving process.

## 3.4 Simulation: RC Model and $H_\infty$ Filter

A battery is a typical time-variant system, closely related to SoC and other battery states. Online identification is the popular strategy for solving the time-variant problem, but at the cost of high time consumption and inaccurate identification results due to noise. An alternative method is to use a robust estimation technique, which constructs a suboptimal filter with the ability to minimize the maximum estimation error caused by the noise and uncertainties of system model.

In pace with the development of $H_\infty$ control theory, researchers have shown great interest in the $H_\infty$ filter [82,83]. A good introduction and review can be found in [84]. In contrast to Kalman filter, $H_\infty$ filter is proposed to handle estimation problems under conditions of uncertain model structure, model parameters, and system noise. It has two main features: (1) it does not require any assumptions about disturbances and model uncertainties; (2) it minimizes the estimation error in the worst situation. Therefore, it is more applicable than Kalman filter in practical application.

### 3.4.1 $H_\infty$ Filter Algorithm

Denoting $x$ as the system state vector, $y$ the output vector, $u$ the input vector, $w$ the process noise, and $v$ the measurement noise, system state space equations are expressed as:

$$\begin{aligned} x_{k+1} &= A_k x_k + B_k u_k + \Gamma_k w_k \\ y_k &= C_k x_k + D_k u_k + v_k \end{aligned} \tag{3.18}$$

The suboptimal $H_\infty$ filtering problem is formalized as: given estimation error bounder $\gamma > 0$, find an estimation of $\hat{z}_k = F_f(u_0, \cdots, u_k, y_0, \cdots, y_k)$ such that

$$\inf_{F_f} \sup_{x_0, w \in H_2, v \in H_2} \frac{\|z_k - \hat{z}_k\|_2^2}{\|x_0 - \hat{x}_0\|_{P_0^{-1}}^2 + \|w_k\|_2^2 + \|v_k\|_2^2} < \gamma^2 \tag{3.19}$$

where $z_k = L_k x_k$ is the estimation goal, i.e., the linear combination of system states, $L_k$ is user-defined state weight matrix, and $\|\chi_k\|_2^2 = \sum_{i=0}^{k} \chi_i^* \chi_i$ .

The solution of the suboptimal $H_\infty$ filtering problem can be calculated by the following recursion formulas:

$$\hat{x}_{k+1,k} = A_k \hat{x}_k + B_k u_k \tag{3.20}$$

$$R_k = \begin{bmatrix} I & 0 \\ 0 & -\gamma^2 I \end{bmatrix} + \begin{bmatrix} C_k \\ L_k \end{bmatrix} P_k \begin{bmatrix} C_k^T & L_k^T \end{bmatrix} \tag{3.21}$$

$$P_{k+1} = A_k P_k A_k^T + \Gamma_k \Gamma_k^T - A_k P_k [C_k^T L_k^T] R_k^{-1} \begin{bmatrix} C_k \\ L_k \end{bmatrix} P_k A_k^T \tag{3.22}$$

$$K_{k+1} = P_{k+1} C_{k+1}^T \left[ I + C_{k+1} P_{k+1} C_{k+1}^T \right]^{-1} \tag{3.23}$$

$$\hat{x}_{k+1} = \hat{x}_{k+1,k} + K_{k+1}(y_{k+1} - C_{k+1}\hat{x}_{k+1,k} - D_{k+1}u_{k+1}) \tag{3.24}$$

$$\hat{z}_{k+1} = L_{k+1}\hat{x}_{k+1} \tag{3.25}$$

under the conditions that $[A_k \ \Gamma_k]$ has full rank and

$$P_k^{-1} + C_k^T C_k - \gamma^{-2} L_k^T L_k > 0 \qquad for \quad all \quad k \tag{3.26}$$

From the above formulas, it is clearly that if $L(k) = I$ and $\gamma \to \infty$, $H_\infty$ filter degrades to be Kalman filter. Thus, Kalman filter is a special situation of $H_\infty$ filter with infinite $H_\infty$ norm, and hence it is the least robust.

### 3.4.2 Battery RC Model

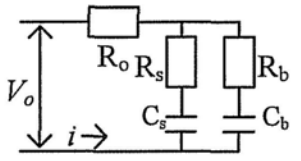


Figure 3.6: Battery RC Model.

As shown in Fig.3.6, we apply battery RC equivalent circuit model in this paper [56]. The RC model consists of a bulk capacitor $C_b$ and a surface capacitor $C_s$, which simulate energy storage and dynamic property of the battery respectively. Output resistance $R_o$, surface resistance $R_s$ and bulk

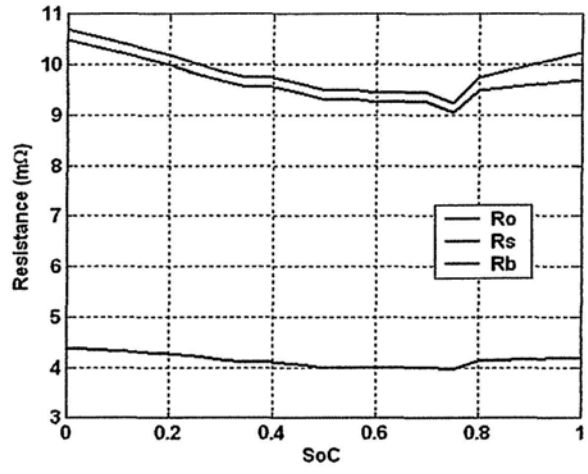


Figure 3.7: Resistance variance of resistors in RC model.

resistance $R_b$ are used to model the internal resistance of battery.

By selecting state vector as the voltages of bulk and surface capacitors $x_k = [V_{bk}, V_{sk}]'$, system input as bus current $u_k = I_k$, output as terminal voltage $y_k = V_{ok}$, and sampling time as $T_s$, the discrete state space equations (3.18) are concrete into the following matrixes.

$$A = \begin{bmatrix} 1 - \frac{T_s}{C_b(R_b+R_s)} & \frac{T_s}{C_b(R_b+R_s)} \\ \frac{T_s}{C_s(R_b+R_s)} & 1 - \frac{T_s}{C_s(R_b+R_s)} \end{bmatrix} \tag{3.27}$$

$$B = \begin{bmatrix} \frac{-R_s T_s}{C_b(R_b+R_s)} \\ \frac{-R_b T_s}{C_s(R_b+R_s)} \end{bmatrix} \tag{3.28}$$

$$C = \begin{bmatrix} \frac{R_s}{R_b+R_s} & \frac{R_b}{R_b+R_s} \end{bmatrix} \tag{3.29}$$

$$D = -R_o - \frac{R_b R_s}{R_b + R_s} \tag{3.30}$$

The SoC for the RC model was estimated by using the voltages of the two capacitors. Since $C_b$ represents the bulk energy in the battery, it contributes the majority of SoC, as expressed in the equations below.

$$\widehat{SoC}_2(k) = \frac{1}{21}\left[20\widehat{SoC}_{C_b}(k) + \widehat{SoC}_{C_s}(k)\right] \tag{3.31}$$

where

$$\widehat{SoC}_{C_b}(k) = F_{OCV-SoC}(V_{bk}) = F_{OCV-SoC}(x_k(1)) \tag{3.32}$$

$$\widehat{SoC}_{C_s}(k) = F_{OCV-SoC}(V_{sk}) = F_{OCV-SoC}(x_k(2)) \tag{3.33}$$

and $F_{OCV-SoC}(\cdot)$ is the function mapping OCV to SoC. It usually is predetermined by manufactory's datasheet or experimental testing data.

Model parameters will essentially change during the running process. A type of 6.5 Ah Prismatic Panasonic NiMH Battery has been tested at the NREL Battery Thermal Management Lab and the corresponding model parameters are provided by Advisor [85]. Fig. 3.7 shows the change in resistance of the resistors versus temperature and SoC. Taking the output resistor as an example, it is clear that the maximum resistance is $0.0216\Omega$, more than three times the minimum value $0.0071\Omega$. The significant variation in the model parameters is worth paying special attention to in the design of the SoC estimator. Other resistors and capacitors have similar properties.

Since the model error is hard to determine aforehand, we leave this difficulty to $H_\infty$ filter and estimate $\Gamma$ only according to current noise. The measured current is $u = I_c = I + I_n$, where $I$ is the clean signal and $I_n$ is the current noise. Therefore, $Bu = BI + BI_n = BI + Bw$, i.e., $\Gamma = B$.

### 3.4.3 Performance Comparison

To demonstrate the performance of $H_\infty$ filter, simulation experiments are conducted to compare the SoC estimation errors among the model output, the results of Kalman filter and the results of $H_\infty$ filter.

As demonstrated above, the adaptive-$\kappa$ nonlinear diffusion filter has the ability to remove the current noise and a self-learning strategy can compensate for zero-drift. Therefore, we fix the SNR of current noise to 10dB and zero-drift to 0.5A, which simulates the residual noise after the two noise reduction steps. The experiments aim to verify the filters' abilities to handle the modeling error, thus we apply a fixed model with the parameters set to their maximum, average, and minimum values of each cycle, respectively. The inaccurate model parameters include the resistances of $R_b$,$R_s$,$R_o$ and capacitance of $C_c$. Since $C_b$ is determined by the nominal capacity of the battery, rather than identification, no modeling error is added to it.

Battery model parameters are from the Panasonic Prismatic 6.5Ah battery. The settings for Kalman filter are experimentally optimized as initial states estimation error $P = 0.01I$, process noise variance matrix $Q = 0.001^2 I$, and measurement noise variance matrix $R = 0.01^2$. The settings for $H_\infty$ filter are $L = [1, 1]$ and $\gamma = 50$. If $\gamma$ fails to satisfy the condition equation (3.26), it will increase 10 step by step till it meets the requirement.

Fig. 3.8 shows the SoC estimation results of the Prius, driving on successive HWFET, WVUSUB, MANHATTAN, and NEDC cycles. Due to the non-zero mean of current noise and model error, the accumulated total errors are reflected in the model output, resulting in a non-convergent estimation result. After a short time of oscillation, Kalman filter gradually converges to

a stable estimation, but with stable errors. Zero-drift and model errors destroy its ability to act as an optimal filter. $H_\infty$ leads to a faster convergence process than Kalman filter and achieves fewer stable errors.

Tab. 3.3 summarizes the numerical results. $H_\infty$ filter clearly has the ability to estimate SoC of the time-variant battery based on a set of fixed parameters. It outperforms Kalman filter no matter which values the model parameters are fixed to. The robustness of $H_\infty$ filter is well demonstrated.

From the results shown in Fig. 3.5 and Fig. 3.8, it is clear that coulomb counting estimation is generally good at the beginning of the period due to small accumulated errors, while $H_\infty$ filter obtains better performance in the latter period, when it reaches convergent estimation. Therefore, one natural way to make best use of the advantages and avoid the disadvantages is to combine the results of the two estimators, weighted by time.

In the proposed framework, we design a simple data fusion unit to achieve the final SoC estimation $\widehat{SoC}(k)$ based on a linear combination of $\widehat{SoC}_1(k)$ and $\widehat{SoC}_2(k)$. The weights of the two estimators are experimentally determined by the following equations:

$$\widehat{SoC}(k) = \begin{cases} \widehat{SoC}_1(k) & t \leq 5 \\ \omega_1 \times \widehat{SoC}_1(k) + \omega_1 \times \widehat{SoC}_2(k) & 5 < t < 10 \\ \widehat{SoC}_2(k) & t \geq 10 \end{cases} \tag{3.34}$$

where $\omega_1 = -0.2t + 2$, $\omega_2 = 0.2t - 1$ and $t$ is the vehicle running time (unit [min]).

Since we have demonstrated that coulomb counting with self-learning

Table 3.3: Performance comparison of SoC estimation based on battery model using a set of fixed parameters (Unit [%]).

| Fix model parameters to | Highway (HWFET) | | | | Suburban (WVUSUB) | | | | Urban (MANHATTAN) | | | | European hybrid (NEDC) | | | |
|---|---|---|---|---|---|---|---|---|---|---|---|---|---|---|---|---|
| | Kalman Filter | | $H_\infty$ filter | | Kalman Filter | | $H_\infty$ filter | | Kalman Filter | | $H_\infty$ filter | | Kalman Filter | | $H_\infty$ filter | |
| | ave | std | ave | std | ave | std | ave | std | ave | std | ave | std | ave | std | ave | std |
| Max. of parameters | 4.38 | 1.41 | 2.92 | 2.03 | 3.99 | 1.44 | 1.71 | 1.59 | 4.00 | 1.98 | 1.35 | 2.32 | 3.57 | 1.22 | 1.60 | 1.61 |
| Ave. of parameters | 4.34 | 2.22 | 2.47 | 1.21 | 3.56 | 1.48 | 1.94 | 2.20 | 3.71 | 1.88 | 1.55 | 1.42 | 3.82 | 1.85 | 1.93 | 1.83 |
| Min. of parameters | 3.77 | 3.73 | 1.50 | 1.15 | 3.20 | 1.20 | 1.78 | 2.01 | 3.92 | 2.24 | 2.15 | 2.19 | 3.90 | 1.58 | 2.22 | 2.34 |

The inaccurate model parameters include resistances of $R_e$, $R_t$, $R_o$ and capacitance of $C_c$, and are fixed to the their maximum, average and minimum values in each driving cycle respectively. White noises with 10dB SNR and 0.5A zero-drift are also added to the real current profile

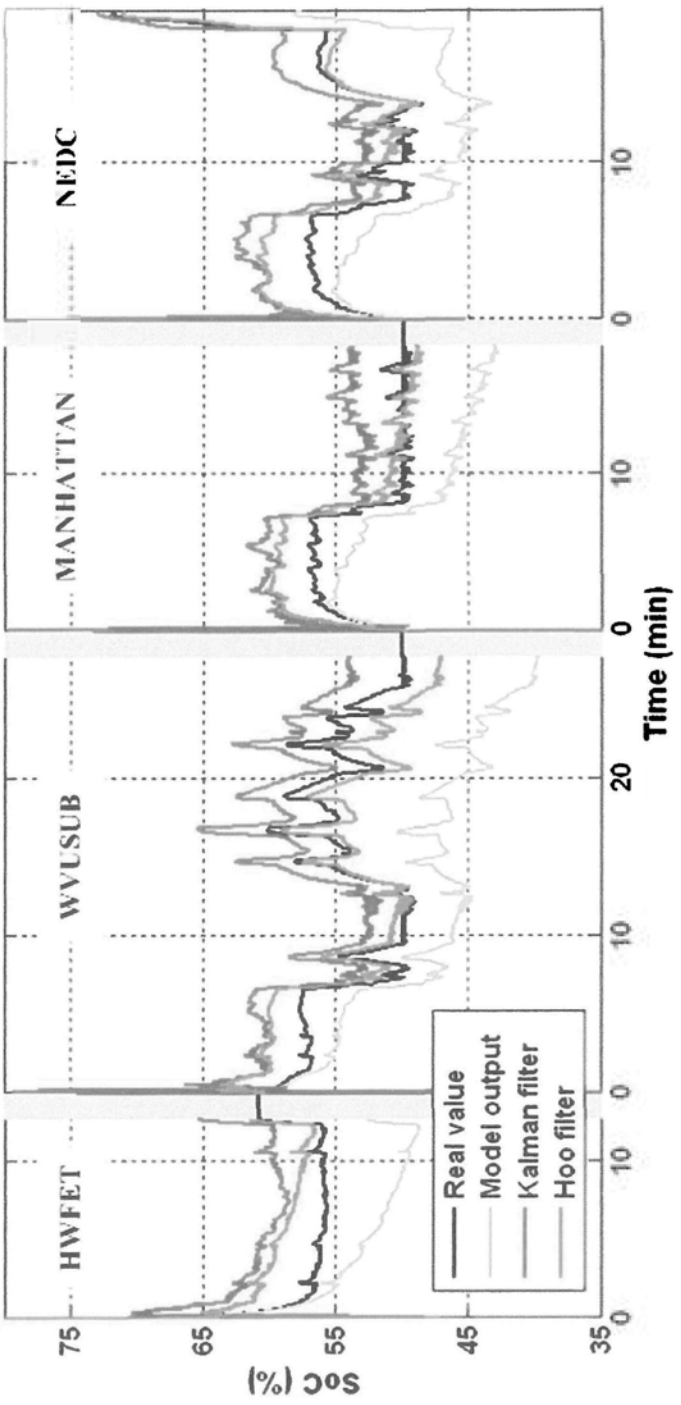


Figure 3.8: SoC estimation results based on inaccurate battery model using the fixed average values of real time-variant parameters.

The gray bars between cycles represent half-hour stops which allow OCV available.
Simulation conditions: white noise with 10dB SNR and 0.5A zero-drift.

strategy outperforms conventional method and $H_\infty$ filter achieves a more robust estimation than Kalman filter in a real vehicle driving environment, verification of the availability and efficacy of the overall framework only requires comparison of its performance with the two single estimators.

The simulation environment is the same as described above. The SNR of white current noise is fixed to 5dB and the zero-drift is set to 0.5A for the first three cycles and changed to 1A for the remainder. To further test the robustness of the whole framework, we introduce the model error ($E_m$), defined as $E_m = p_m/p_r$, where $p_m$ is the model parameter, $p_r$ is the real parameter, $p$ presents the arbitrary parameters of $R_o$, $R_s$, $R_b$ and $C_c$. The $E_m$ varies from 1.2 in the first cycle to 0.7 in the last cycle.

The estimation results are shown in Fig.3.9 and Fig.3.10 gives the averages of absolute estimation errors and their standard deviations in each cycle.

In the first cycle of HWFET, the zero-drift in measurement of current, as well as the model error, results in a large error in the coulomb counting and $H_\infty$ filter. The fusion of the two approaches can reduce this error. In the following two cycles, the self-learning strategy estimates the zero-drift and effectively compensates for the error. Although the other two approaches also show good performance, the hybrid approach outperforms them. In the fourth cycle, the drift is increased. The errors of $H_\infty$ filter and coulomb counting are greatest in the first third and latter two-thirds respectively, while the hybrid approach has the least error. In the last two cycles, self-learning estimates the zero-drift again. Consequently, performance of the Ah method is improved. Even though the model error is increased, due to it robustness the $H_\infty$ filter converges to a small error after passing through a

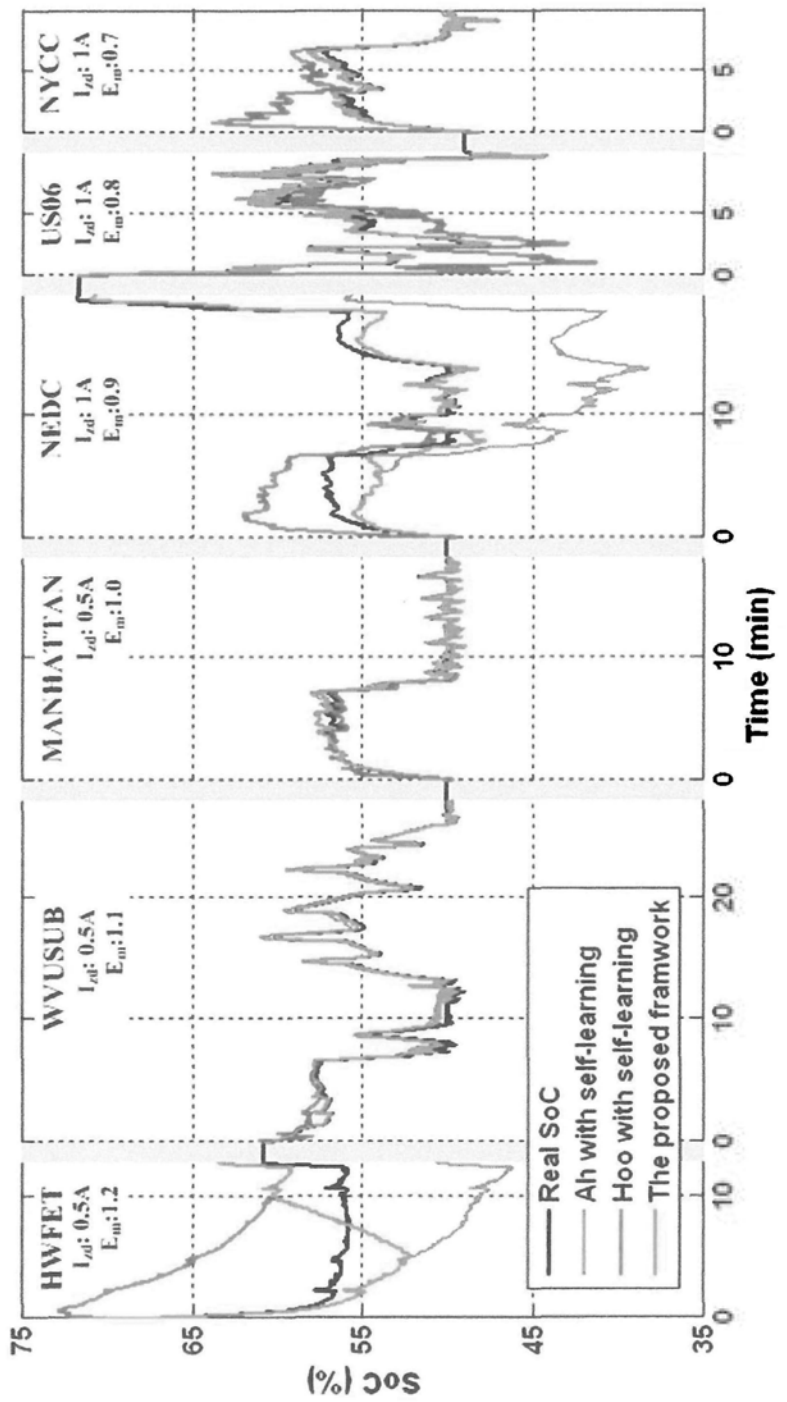


Figure 3.9: SoC estimation results of self-learning coulomb counting, $H_\infty$ filter and the overall framework. The gray bars between cycles represent half-hour stops which allow OCV available. Simulation conditions: white noise with 5dB SNR, zero-drift 0.5A for the 1st-3rd cycles and 1A for the 4th-6th cycles, model error changes from 1.2 to 0.7.

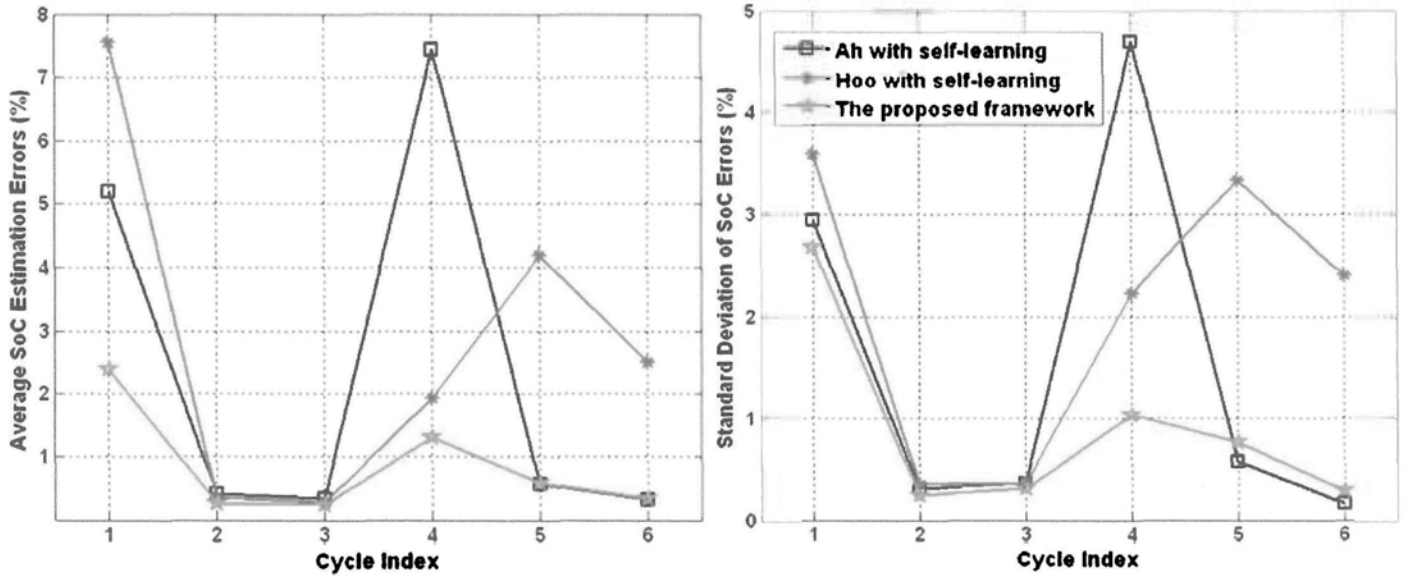


Figure 3.10: Numerical indexes of SoC estimation results of self-learning coulomb counting, $H_\infty$ filter and the overall framework.

The left subfigure shows average absolute estimation error while the right subfigure illustrates their standard deviation. Simulation conditions: white noise with 5dB SNR, zero-drift 0.5A for the 1st-3rd cycles and 1A for the 4th-6th cycles, model error changes from 1.2 to 0.7.

short period of large error, so that the combined results still result in good performance.

As a summary, the performance of coulomb counting and $H_\infty$ filter are dependent on the model error, noise and zero-drift. Although their individual performance is slightly better in some regions, the overall performance of the hybrid method is superior overall.

## 3.5 Experiment and Application: Modified ESC Model and Extended Kalman Filter

### 3.5.1 Modified ESC Model

In experiments and application, we select and revise the nonlinear battery model "enhanced self-correcting model (ESC)" proposed in [57] for two reasons: (1) it is more accurate to model the LiFePO4 battery with a clear physical background; (2) to demonstrate the proposed framework in various situations.

The ESC model is expressed as:

$$\begin{bmatrix} f_{k+1} \\ h_{k+1} \\ SoC_{k+1} \end{bmatrix} = \begin{bmatrix} diag(\alpha) & 0 & 0 \\ 0 & F(I_k) & 0 \\ 0 & 0 & 1 \end{bmatrix} \begin{bmatrix} f_{k+1} \\ h_{k+1} \\ SoC_{k+1} \end{bmatrix} + \begin{bmatrix} 1 & 0 \\ 0 & 1 - F(I_k) \\ -\frac{\eta_i T_s}{C_n} & 0 \end{bmatrix} \begin{bmatrix} I_k \\ M(SoC, \dot{SoC}) \end{bmatrix} \tag{3.35}$$

$$V_k = OCV(SoC_k) - RI_k + h_k + Gf_k \tag{3.36}$$

The model first estimates SoC based on coulombic counting method and then establishes the relationship between SoC and simultaneous terminal voltage. Since terminal voltage is measurable during the vehicle running process, it is applied as the system output to establish the closed-loop estimation.

The mapping from SoC to terminal voltage consists of four parts: (1) OCV, (2) voltage decrease or increase due to the internal resistance during charge and discharge, (3) hysteresis, which represents the hysteresis phenomenon, and (4) the current filter, which expresses the dynamic behavior of battery.

In this thesis, we have established the ESC model of the batteries used in experiments, with modification to the implementation of the current filter.

### SoC vs. OCV

The mapping from SoC to OCV $V_{OCV}(k) = OCV(SoC(k))$ is established using a curve fitting method based on the real data. As shown in Fig. 3.11, we measure the OCV at each concerned SoC point and then apply a nonlinear model to fit the curve.

As suggested in [57], the OCV function is designed as the equation below, to enable its derived function to be calculated easily.

$$OCV(SoC(k)) = a_0 - \frac{a_1}{SoC(k)} - a_2 SoC(k) + a_3 \ln(SoC(k)) + a_4 \ln(1 - SoC(k)) \tag{3.37}$$

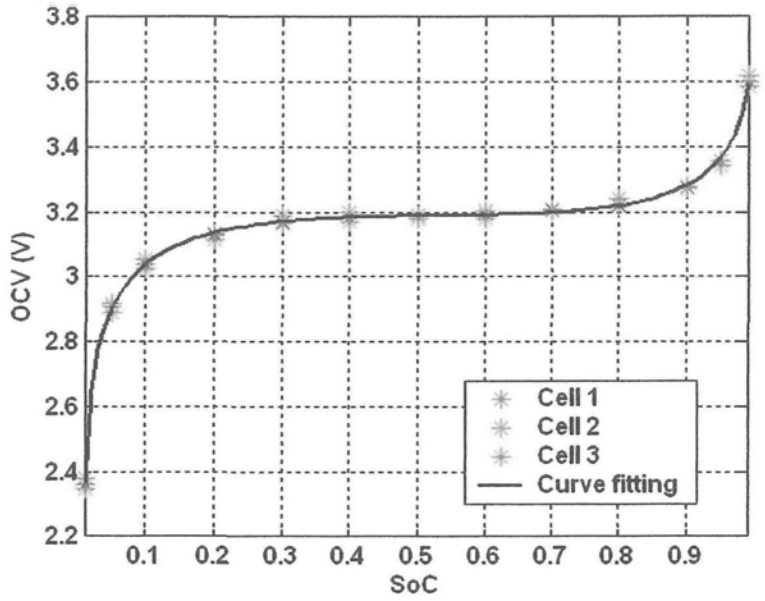


Figure 3.11: SoC vs. OCV samples and curve fitting results.

where $a = [3.545, 0.00338, 0.6605, 0.1828, -0.1539]$, identified by curve fitting.

It is worth noting that the above equation cannot solve the situations $SoC = 1$ and $SoC = 0$, therefore we use $SoC = 0.01$ and $SoC = 0.99$ to present the empty and full states. In the following, we use the same equation to model internal resistance and hysteresis.

### Ohmic drop/rise

When the battery is operating, discharge or charge current will cause the terminal voltage to rise or fall due to its internal resistance R, as expressed by $RI(k)$.

In a strict sense, the internal discharging and charging resistances of the

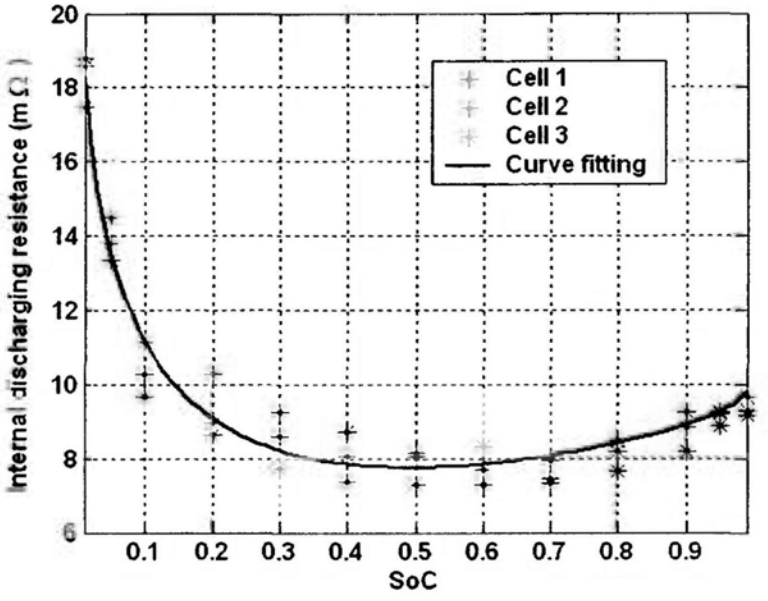


Figure 3.12: SoC vs. internal discharging resistances of cells.

battery are variables that change along with SoC, as shown in Fig. 3.12 and Fig. 3.13. Although in [57], internal resistance is modeled as a constant, we find it is not accurate enough for our application, where the highest internal resistance is more than twice that of the lowest. Thus, we use the same equation to fit the curve for internal resistance.

For discharging resistance, we have

$$R_{dis}(SoC(k)) = a_0 - \frac{a_1}{SoC(k)} - a_2 SoC(k) + a_3 \ln(SoC(k)) + a_4 \ln(1 - SoC(k)) \tag{3.38}$$

where $a = [0.5291, 0.0247, -8.164, -4.341, -0.2616]$, identified by curve fitting.

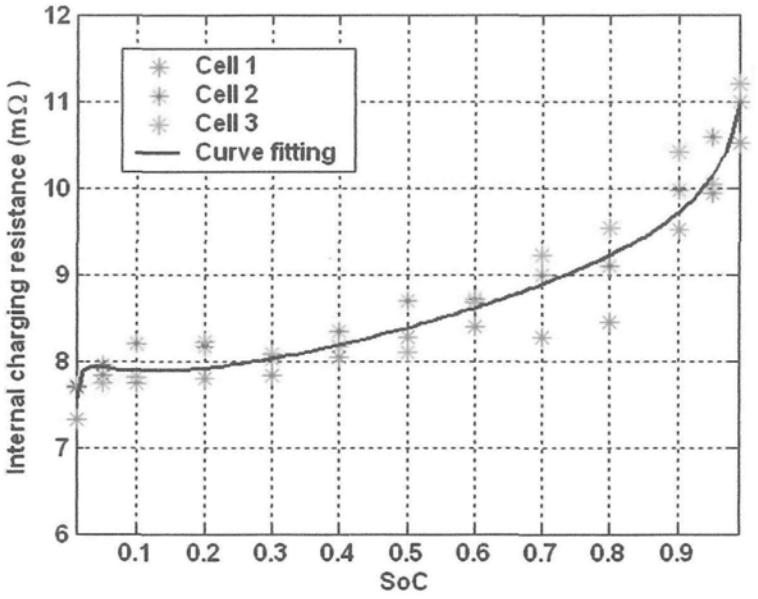


Figure 3.13: SoC vs. internal charging resistances of cells.

For charging resistance, we also have

$$R_{chg}(SoC(k)) = a_0 - \frac{a_1}{SoC(k)} - a_2 SoC(k) + a_3 \ln(SoC(k)) + a_4 \ln(1 - SoC(k)) \tag{3.39}$$

where $a = [6.837, 0.01123, -1.901, -0.3976, -0.4924]$, also identified by curve fitting.

### Hysteresis

Ideally, after operation of the battery, terminal voltage will gradually converge to the OCV. However, in practice, the convergence value after a discharge process is always smaller than OCV, while that after a charge is always bigger. This phenomenon is called hysteresis.

To model the hysteresis, the cells are firstly discharged using a C/20

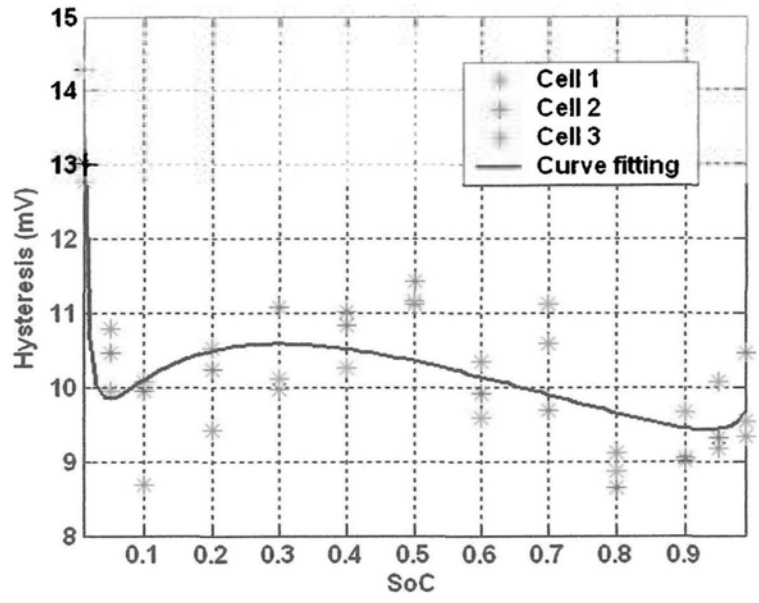


Figure 3.14: SoC vs. hysteresis of cells.

current from full to empty and then charged to full using the same current rate, at 25°C. The two discharge and charge curves, indexed by SoC, are not coincidental. The voltage difference consists of the ohmic voltage and hysteresis. Since the current is very small, the ohmic voltage is only about $2.8mV$. Therefore, the remaining voltage difference is caused by hysteresis. Fig. 3.14 shows the half voltage difference caused by the hysteresis effect, with $RI(k)$ subtracted. In this work, we use the same equation to fit the hysteresis curve .

$$M(SoC(k)) = a_0 - \frac{a_1}{SoC(k)} - a_2 SoC(k) + a_3 \ln(SoC(k)) + a_4 \ln(1 - SoC(k)) \tag{3.40}$$

where $a = [14.39, -0.08124, 6.033, 1.963, -0.2637]$, identified by curve fitting.

In application, $h(k) = s_H(k)M$, where $s_H(k)$ represents the sign of the

current and is expressed as

$$s_H(k) = \begin{cases} 1 & I(k) > \epsilon \\ -1 & I(k) < -\epsilon \\ s_H(k-1) & |I(k)| < \epsilon \end{cases} \tag{3.41}$$

### Dynamics of Current

The above modeling components do not take into consideration the dynamic response of the battery. In fact, battery takes some time for its terminal voltage to reach a stable value if given a step signal.

As shown in Fig. 3.15, the above model without the consideration on time constant is unable to simulate the dynamics of battery. The original method used to simulate the system proposed in ESC applies a state-space form $V_f(k) = Gf(k) = GA_f f(k-1) + GB_f I(k-1)$, where $A_f = diag(\alpha)$ is the state-transition matrix, $B_f$ is the arbitrary input matrix, and G is the output which make the $Gf(k) \rightarrow 0$, during the constant-current period.

However, the design of $A_f$, $B_f$, and hence $G$ is not based on any obvious physical meaning. The time constant and gain of the current filter is also not explicitly expressed in the matrix parameters. Since the transitional period is very similar with a exponential decay function, we propose a new design method to realize the modeling of battery dynamics.

Given a step function $u(t)$, the desired response of battery is an exponential decay $y(t) = e^{-\frac{t}{\tau}}$, therefore, the transfer function can be implemented

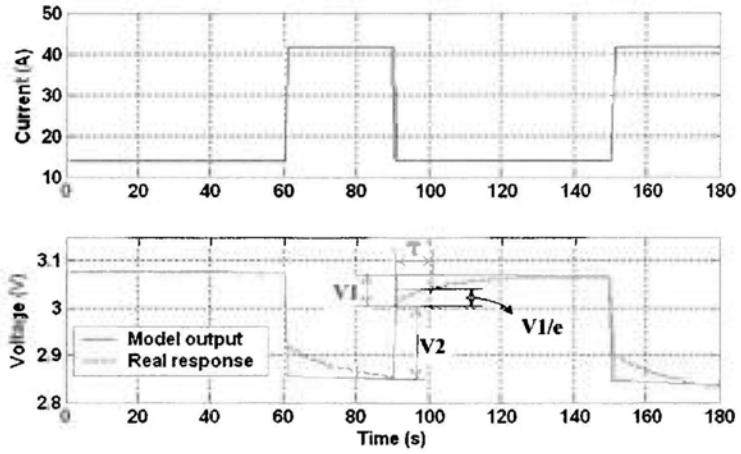


Figure 3.15: Battery dynamic response to step discharge current and model output without dynamic consideration.

using the Laplace transform:

$$G(s) = \frac{I_f(s)}{I(s)} = \frac{Ks}{s+\tau} \tag{3.42}$$

where $K$ is the gain and $\tau$ is the exponential time constant representing the time needed for the initial value to be reduced by a factor of $e$.

As shown in Fig. 3.15, $K$ is determined by $K = \frac{V1}{V1+V2}$ and $\tau$ is measured directly from the duration of time when the initial value $V1$ decays to $V1/e$. In this thesis, $K = 0.287$ and $\tau = 12.5s$.

In application, the continuous transfer function is discretized at the sampling period $T_s$. In this work, discretization is implemented based on a triangle approximation. The discrete time form is expressed by:

$$G(z) = \frac{I_f(z)}{I(z)} = \frac{n_1 z + n_2}{d_1 z + d_2} \tag{3.43}$$

where $n_1 = 0.2758, n_2 = -0.2758, d_1 = 1, d_2 = -0.9231$ in this work when $T_s = 1s$.

Finally the whole battery model is given by:

$$\begin{bmatrix} I_f(k) \\ SoC(k) \end{bmatrix} = \begin{bmatrix} -d_2/d_1 & 0 \\ 0 & 1 \end{bmatrix} \begin{bmatrix} I_f(k-1) \\ SoC(k-1) \end{bmatrix} + \begin{bmatrix} n_2/d_1 & n_1/d_1 \\ 0 & -\eta T_s/C_n \end{bmatrix} \begin{bmatrix} I(k-1) \\ I(k) \end{bmatrix} \tag{3.44}$$

$$\begin{aligned} V(k) = OCV(SoC(k)) - s_{dis}(k)R_{dis}(SoC(k))(I(k) - I_f(k)) \\ -s_{chg}(k)R_{chg}(SoC(k))(I(k) - I_f(k)) - s_H(k)H(SoC(k)) \end{aligned} \tag{3.45}$$

where $s_{dis} = 1, s_{chg} = 0$ when $I(k) - I_f(k) \geq 0$ and $s_{dis} = 0, s_{chg} = 1$ when $I(k) - I_f(k) < 0$.

### 3.5.2 Extended Kalman Filter Algorithm

Unlike the linear RC model used in simulations, the above modified ESC model is a nonlinear model which cannot be applied in the linear $H_\infty$ filter mentioned above. Therefore, in experiments and application, we utilize extended Kalman filter to implement the closed loop component in our proposed framework.

Consider a discrete-time nonlinear system with state vector $x_k$, input vector $u_k$ and observation vector $y_k$ at the time instance $k$. The dynamic

state space model can be represented in the form:

$$\begin{aligned} x_{k+1} &= f\left(x_k, u_k, w_k\right) \\ y_k &= g(x_k, v_k) \end{aligned} \tag{3.46}$$

where $f(\cdot)$ is the state evolution function and $g(\cdot)$ is the observation function. $w_k$ and $v_k$ stand for process and measurement noise vectors respectively, with associated covariance matrices $Q = E\left\{w_k w_k^T\right\}$ and $R = E\left\{v_k v_k^T\right\}$. To iterate the evolution process, an initial state vector should be estimated ahead, denoted by $x_0$. Then the expectation of initial estimates of states and covariance matrix are given by $\bar{x}_0 = E\left\{x_0\right\}$ and $P_0 = E\left\{(x_0 - \bar{x}_0)(x_0 - \bar{x}_0)^T\right\}$.

For application of EKF, it is also necessary to derive the linearized state and observation equations with respect to states and noises near a desired reference point $(\hat{x}_k, u_k, \bar{w}_k, \bar{v}_k)$:

$$\begin{aligned} x_{k+1} &\approx f(\hat{x}_k, u_k, \bar{w}_k) + A_k(x_k - \hat{x}_k) + F_k(w_k - \bar{w}_k) \\ y_k &\approx g(\hat{x}_k, \bar{v}_k) + C_k(x_k - \hat{x}_k) + G_k(v_k - \bar{v}_k) \end{aligned} \tag{3.47}$$

where

$$\begin{aligned} A_k &= \frac{\partial f(x, u_k, \bar{w}_k)}{\partial x}\Big|_{x=\hat{x}_k} \\ F_k &= \frac{\partial f(\hat{x}_k, u_k, w)}{\partial w}\Big|_{w=\bar{w}_k} \\ C_k &= \frac{\partial g(x, \bar{v}_k)}{\partial x}\Big|_{x=\hat{x}_k} \\ G_k &= \frac{\partial g(\hat{x}_k, v)}{\partial v}\Big|_{v=\bar{v}_k} \end{aligned} \tag{3.48}$$

$\bar{w}_k = E\left\{w_k\right\}$ and $\bar{v}_k = E\left\{v_k\right\}$ are the expectations of input noise vector and measurement noise vector respectively, $\hat{x}_k$ is the estimate of state vector at

time instance $k$.

The Kalman filter has two distinct phases: prediction and update. The first utilizes the state estimate based on the previous information to produce an estimate of states at the current time. In the update phase, measurement information at the current time is applied to refine this prediction and obtain a revised, and hopefully more accurate result, again for the current time instance.

(1) Predict equations:

$$\begin{aligned} \hat{x}_{k|k-1} &= f(\hat{x}_{k-1|k-1}, u_k, \bar{w}_k) \\ P_{k|k-1} &= A_k P_{k-1|k-1} A_k^T + F_k Q_k F_k^T \end{aligned} \tag{3.49}$$

(2) Innovation equation:

$$\begin{aligned} e_k &= y_k - g(\hat{x}_{k|k-1}, \bar{v}_k) \\ S_k &= C_k P_{k|k-1} C_k^T + G_k R_k G_k^T \end{aligned} \tag{3.50}$$

(3) Update equations:

$$\begin{aligned} K_k &= P_{k|k-1} C_k^T {S_k}^{-1} \\ \hat{x}_{k|k} &= \hat{x}_{k|k-1} + K_k e_k \\ P_{k|k} &= P_{k|k-1} - K_k C_k P_{k|k-1} \end{aligned} \tag{3.51}$$

where $\hat{x}_{k|k-1}$ and $P_{k|k-1}$ are the prediction output based on past measurement and corresponding error covariance matrix, $e_k$ and $S_k$ is the innovation information obtained from current measurement and corresponding innova-

tion covariance matrix, $\hat{x}_{k|k}$ and $P_{k|k}$ are the refined estimate results based on the Kalman gain $K_k$ derived from innovation information.

In the modified ESC model, the above procedure is realized by

$$A_k = \begin{bmatrix} -d_2/d_1 & 0 \\ 0 & 1 \end{bmatrix} \tag{3.52}$$

$$F_k = I \tag{3.53}$$

$$C_k = \begin{bmatrix} \frac{\partial V(k)}{\partial I_f(k)}\Big|_{SoC(k)} & \frac{\partial V(k)}{\partial SoC(k)}\Big|_{I_f(k)} \end{bmatrix} \tag{3.54}$$

$$G_k = 1 \tag{3.55}$$

### 3.5.3 Performance Demonstration

In experiments, the "real" SoC is calculated based on coulombic counting according to measurement of the electric loader and charger, with both discharging and charging efficiencies of 1.

A combined pulse discharge test is conducted based on the electric loader. A discharge cycle consists of 2C discharge for 60 seconds and 3C discharge for 30 seconds. As shown in Fig. 3.16, the initial SoC is intended to be different from the real value. In the first round, the current sensor with a measurement range from [-200A 200A] actually has a bias of around +2A, causing a gradual increase in the estimation error of the coulomb counting method. EKF has the ability to follow the real SoC trajectory based on the voltage feedback. The average SoC estimation error is 6.235%, while the maximum error, with the exception of the errors affected by the initial error, is 11.273%. In the

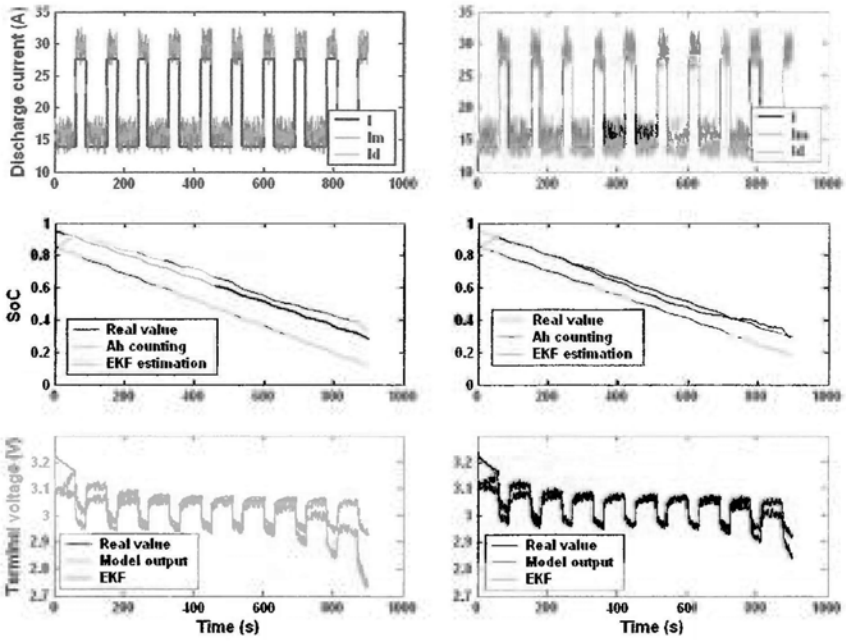


Figure 3.16: Discharge experiment results based on electric loader.

second round, based on the error of the coulomb counting method, the zero-drift of current measurement is estimated as 1.908A, without the effect of the initial SoC error. By removing the zero-drift, estimation results are greatly improved, with an average error of 4.673% and maximum error of 7.632%.

In the same manner, a charge test is conducted using a combined pulse with 2C for 60s and 3C for 30s. As shown in Fig. 3.17, in the first round we also assume the zero-drift is unknown. The average error is 5.863% and the maximum is 9.736%. In the second round, the estimated zero-drift is 1.836A, average error is 4.352%, and the maximum error is 7.018%.

Since the above results verify that the model based on EKF estimation outperforms the coulombic counting method in every process, the data fusion unit in the real application is designed to trust the results of EKF, and the

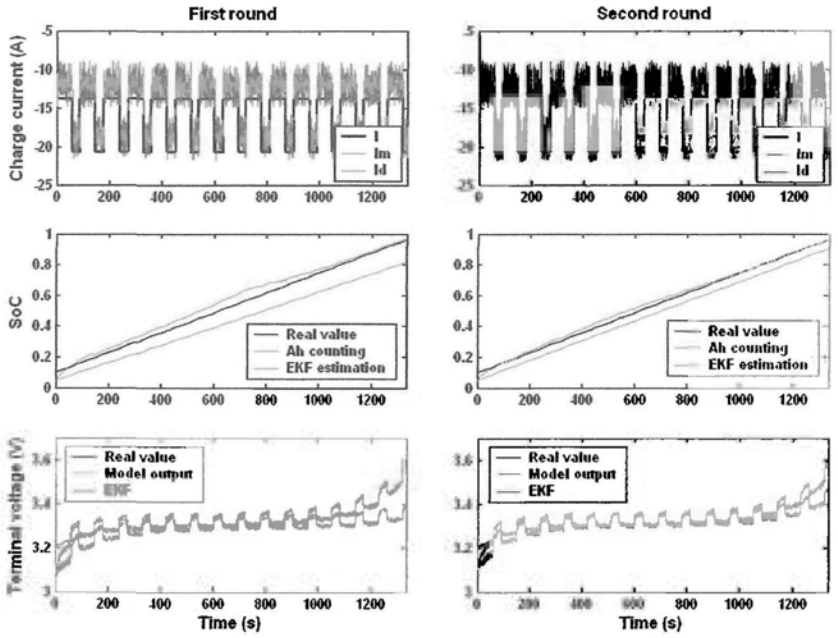


Figure 3.17: Charge experiment results based on electric charger.

estimation results of coulombic counting are only applied to estimate zero-drift. As shown in Fig. 3.18, the battery pack has been tested in a real application. To keep the vehicle speed at 20km/h, we initially operate the vehicle in pure electric mode, then turn on the engine to provide the driving torque and charge the battery. The procedure is then repeated once.

SoC of each extended cell is measured online, with the known zero-drift of 1.875A estimated in the experimental platform. Since the number of extended cells is too large to show each one, only the estimated results for the highest cell, the lowest cell, and the average value are shown. Results for the other cells are similar. In real application, the true SoC of each extended cell is unknown online. Only when the vehicle is stopped and the corresponding OCV becomes available, we can get the "real" value of the

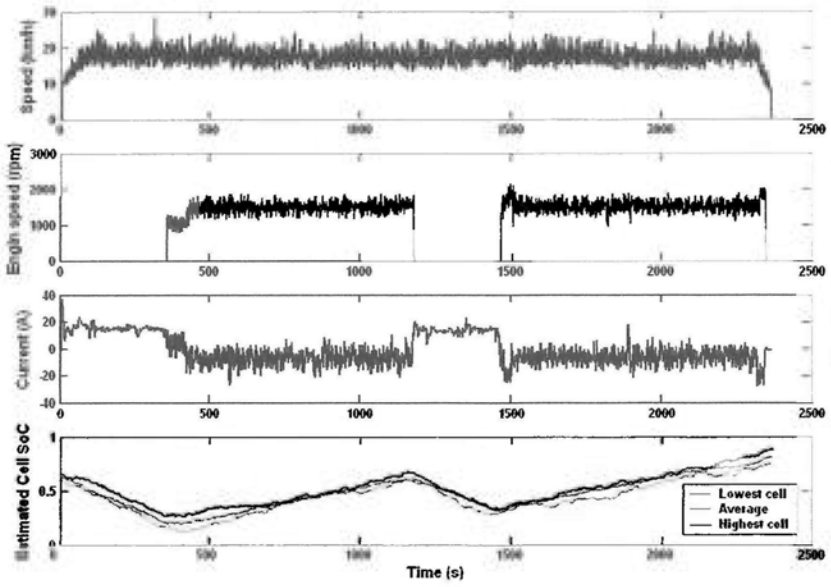


Figure 3.18: Cell SoC estimation in a hybrid electric vehicle.

final SoC. The maximum SoC estimation error at the end of the running process is 7.635%, the minimum is 3.263%, and the average is 5.893%. The estimation results satisfy the requirement of 8% in China's newly published development goal [86].

## 3.6 Summery

oise produced by different sources of interference in the vehicle driving environment, and zero-drift caused by sensors and measurement circuits, fail to satisfy the prerequisites of the typical SoC estimation methods, such as coulomb counting and Kalman filter, to realize their theoretically optimal performance. Therefore, it is necessary to study the anti-noise and self-adaption abilities of SoC estimation, and enhance estimation robustness in the presence of non-ideal conditions.

In this chapter, we propose a framework to implement a robust estimation of SoC in the application of EVs. Firstly, the proposed adaptive-$\kappa$ nonlinear diffusion filter is able to estimate the SNR of the noisy signal and reduce noise according to the degree of change. Since it captures the main difference between the real signal and measured noise, it outperforms the linear digital filter and wavelet based filter. The zero-drift in the measurement of current is then estimated using the estimation error of coulomb counting at each SoC calibration available moment. This self-learning strategy works simply because the accumulated error is mainly attributed to the non-zero mean of noise.

In simulation, $H_\infty$ filter is introduced to realize the robust estimation using a fixed RC model. Although the fixed model cannot fully predict the dynamics of a time-variant battery, the inherent robustness of $H_\infty$ filter successfully handles the model's uncertainty and the estimation gradually converges to stable tracking with small errors. In experiment and application, we propose the modified ESC model to establish a model of the real applied LiFePO4 battery, and then apply EKF to estimate SoC. The availabilities and effectiveness of the individual components and overall framework have been demonstrated by simulations, experiments, and application. Its performance satisfies the national development goal of China.

---

□ **End of chapter.**

# Chapter 4

# State of Charge based Cell Equalization

## 4.1 Introduction

The existing technologies in battery design and production cannot retain the consistency of cell parameters, such as internal resistance, charge and discharge efficiencies, speed of aging and degradation, and so forth. The differences will result in the imbalance of cells in the same battery package and force cells to have different states of charge and terminal voltages. Therefore, monitoring and control at the battery level are insufficient to manage a battery, especially a vehicular battery.

The most significant problem caused by cell imbalance is the SoC difference among cells. The battery behavior is a typical cask effect, where the cell with the lowest SoC determines the discharge capacity and the highest determines the charge capacity. Therefore, to maximize the capacity of the

whole battery and avoid overcharge and overdischarge damage, it is necessary to keep the SoC differences within a tolerably small range. This function, known as battery equalization or cell equalization, has become one of the most difficult and important issues in battery management systems (BMS), especially for EVs.

The study of battery equalization mainly focuses on the equalizing circuit design and equalizing current control. The equalizing circuit design is generally categorized into discharging equalization, charging equalization, and transferring equalization.

Discharging equalization is a dissipative method which discharges the cells with higher SoC via bypass resistors [87]. Although this method is easy to implement at a low cost, it reduces the capacity of the battery to the lowest level determined by the weakest cell and requires special thermal management to handle the heating of the bypass resistors.

Charging equalization balances cells by feeding them with different amounts of charge. One strategy is to charge the whole battery pack, with each cell parallel connected with a shunt resistor. A MOSFET series connected with each shunt resistor is controlled to tune the shunt current [88]. A simple design based on this principle directly disconnects the fully-charged cells from the battery pack [89]. Another way is to route a boost current to the weaker cells through a selective relay matrix [90, 91]. The disadvantage of charging equalization is that it only works when used with a charger, thus it cannot work in hybrid electric vehicles and during the vehicle running process.

Transferring equalization is an advanced equalization method that delivers the charge from higher SoC cells to lower ones to achieve a balance.

This method results in little energy loss and can work without any external components, thus it has attracted a lot of research interest in recent years. The charge transfer can be implemented by a capacitor, inductor, and transformer. Capacitor or inductor based transfer is usually utilized in cell-to-cell equalization. The higher voltage cell firstly discharges the electric energy to be stored in the capacitor or inductor, which then releases the stored energy to charge the lower voltage cells. The time sequence is controlled by MOSFET according to a pulse-width modulation (PWM) signal [92–94]. Transformer based equalization is often employed in battery pack or module pack cell equalization, in which the selected cells, usually the weakest cells, are charged using the energy of the whole battery pack. The transformer is applied to convert the high voltage of the battery to the low voltage of the cell. The equalizing current is also controlled by a MOSFET according to the PWM signal [95, 96]. Further details on equalizing circuit design are reviewed in [88, 89, 97].

Compared with the intensive designs of equalizing circuits, control of the equalizing current has still not been comprehensively studied. The equalizing current determines the duration of equalization and is usually designed to be large when the difference in terminal voltage between the selected or neighbored pair of cells is large, and to be small when the difference is small. It also takes into consideration the terminal voltage - the higher it is, the smaller the current. Based on these general concepts, a fuzzy control system is proposed in [98] to tune the equalizing current in real-time. However, the state that causes the difference in terminal voltage, and that should really be equalized, is the SoC. Although the open circuit voltage (OCV) can indirectly

represent SoC, a small difference in OCV may be caused by a large difference in SoC, due to the nonlinear and flat voltage-SoC relationship. Therefore, [99] has recently proposed an equalization control method directly based on SoC estimation; nevertheless, the SoC is only utilized as a threshold to turn the equalization process on and off, rather than to tune the equalizing current.

In this chapter, we apply the well-studied modified bi-directional Cûk-converter as the equalizing circuit [98, 100] and propose an online SoC estimation based fuzzy controller to tune the equalizing current, with the aim of accelerating equalization speed, enhancing energy efficiency, and protecting cells. In Section 4.2, the equalizing circuit is introduced and formulized using an analytic method. To emphasize the nonlinear property of the OCV-SoC relationship, the cell is modeled as a SoC-dependent voltage source with a series-connected SoC-dependent internal resistor. Based on online SoC estimation, a fuzzy controller is proposed to determine the equalizing current in Section 4.3. To demonstrate the availability and efficacy of the proposed method, in Section 4.4, simulations and experiments are conducted to evaluate overall performance. Conclusions are provided in Section 4.5.

## 4.2 Equalizing Circuit and Analysis

### 4.2.1 Battery Modeling

To analyze the dynamics of the equalizing circuit, it is necessary to model the cell. One method is to use a capacitor which simulates energy storage and a series-connected resistor which simulates internal resistance [98]. This cell model leads to a linear relationship between the residual charge and OCV,

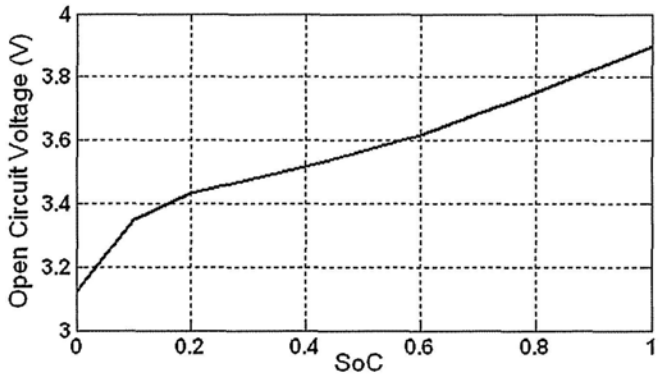


Figure 4.1: Typical OCV-SoC curve of a Saft 6Ah Li-ion cell at $25^oC$, provided by Advisor.

as expressed by $Q = CV$. However, in reality, the SoC-OCV relationship is typically a nonlinear curve, especially for Lithium-ion batteries, as shown in Fig.4.1. The internal resistance is also a changeable variable, along with SoC, as shown in Fig.4.2. Therefore, a capacitor-resistor model is insufficient to model the cell dynamics in battery equalization.

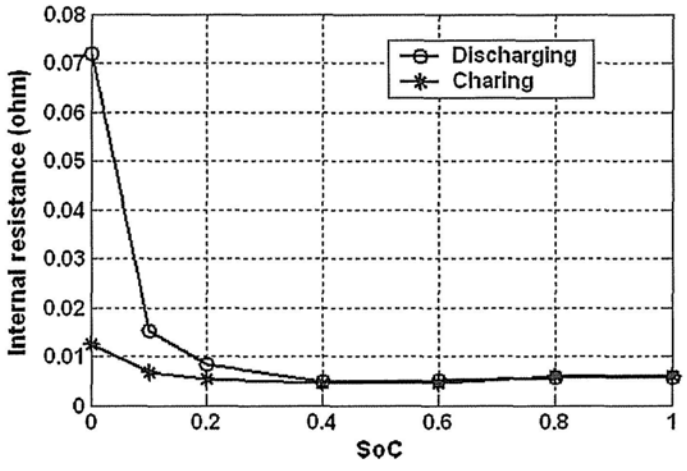


Figure 4.2: Typical internal resistance vs. SoC curve of a Saft 6Ah Li-ion cell at $25^oC$, provided by Advisor.

Considering that in a MOSFET control cycle only a very few charges are transferred, the variation in cell voltage will be small enough to be ignored. Thus, we model the cell as a voltage source with a series-connected resistor. The voltage of the voltage source and the resistance of the resistor are both determined by the SoC, according to the cell characteristic curves obtained either by testing or from the manufacturing datasheet.

### 4.2.2 Equalizing Circuit and Principle

As shown in Fig.4.3, the framework of battery equalization in this paper is based on individual cell equalizers (ICEs), which balance each pair of neighboring cells [98]. A battery pack containing $n$ cells requires $(n-1)$ ICEs.

Since an ICE works on a cell-to-cell level, only *Cell 1* and *Cell 2* are used to facilitate the following illustration and analysis, as shown in Fig.4.4(a). The implementation of each ICE has multiple options, as reviewed in Section 4.1. In this study, we choose the modified bi-directional Cûk-converter, as shown in Fig.4.4(b).

The equalizer has a symmetrical structure; therefore, without loss of generality, we assume the SoC of *Cell 1* is larger than that of *Cell 2*. The circuit is driven by a PWM signal which controls MOSFET $Q_1$ to be on or off.

Denoting $V_1$ and $V_2$ as the voltages of voltage sources, $V_{L_1}$ and $V_{L_2}$ as the voltage of $L_1$ and $L_2$, $V_C$ as the voltage of $C$, the positive direction of $i_1$ and $i_2$ as shown in Fig.4.4(c), $f_s$ and $D$ as the control frequency and duty cycle to $Q_1$, $T_0 = D/f_s$ as the timing to tune off $Q_1$, and $T_s = 1/f_s$ as the period of a control cycle, the circuit dynamics in each $Q_1$ control period are analyzed

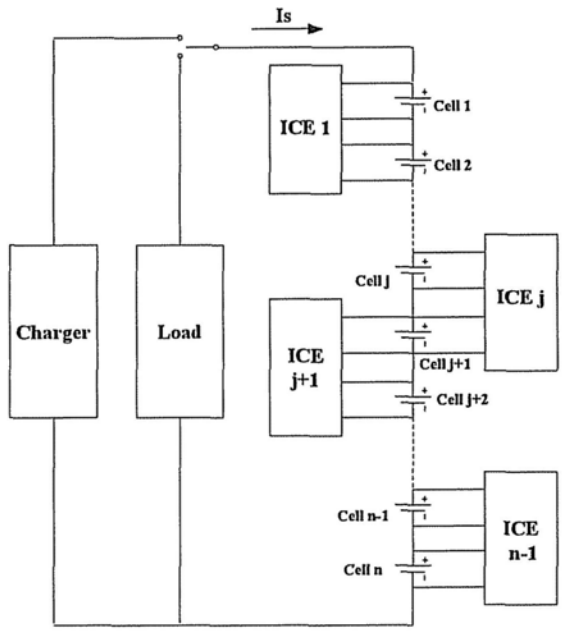


Figure 4.3: The framework of individual cell equalization system.

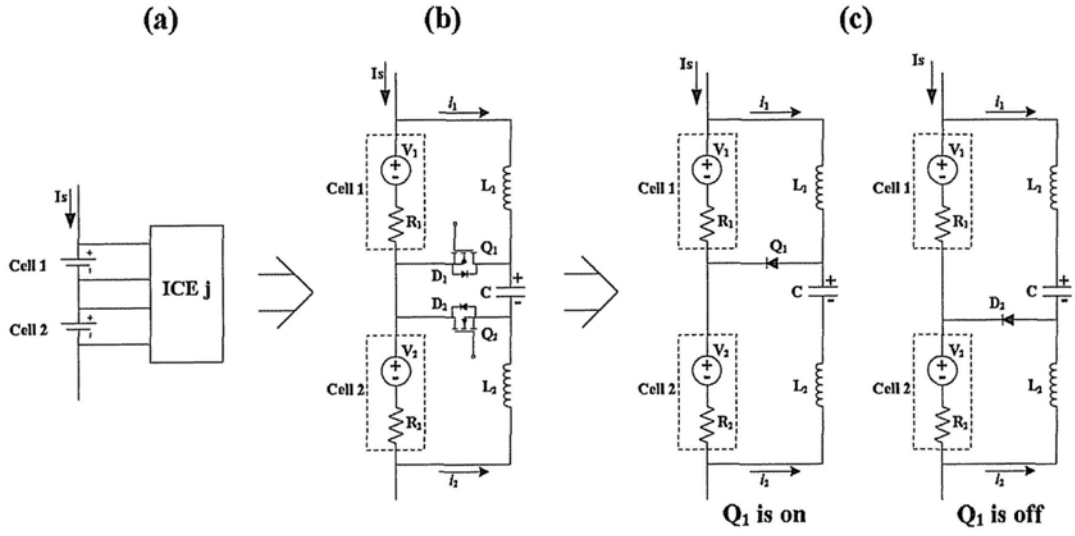


Figure 4.4: Circuit design and analysis of individual cell equalization.

as follows:

In the initial state, there is no current in the whole circuit, $i_1 = i_2 = 0$, and the voltage of the medium capacitor equals to $V_C = V_1 + V_2$.

In the period $(0, T_0]$, $Q_1$ is on and the equivalent circuit is shown in Fig.4.4(c) left. On the *Cell 1* side, $i_1 > 0$, *Cell 1* discharges to $L_1$ and $L_1$ stores the energy. On the *Cell 2* side, $i_2 > 0$, the medium $C$ discharges to *Cell 2* and $L_2$ also stores some of the energy.

In the period $(T_0, T_s]$, $Q_1$ is off and the equivalent circuit is shown in Fig.4.4(c) right. On the *Cell 1* side, since the inductor $L_1$ has the ability to maintain the direction of $i_1$, the $L_1$ will charge $C$ using its stored energy. In this period, *Cell 1* is still discharging. The $D_2$ limits the direction of $i_1$, thus when $i_1 = 0$ the circuit reaches a stable state. In the same manner, on the *Cell 2* side, $L_2$ also charges continuously *Cell 2* until the stored energy is totally transferred. When $i_2$ reduces to 0, the circuit reaches a steady state.

Through careful selection of $L_1$, $L_2$, $C$, $f_s$ and $D$, the final states of $L_1$, $L_2$ and $C$ after a $Q_1$ control cycle can be reset to the same as their initial states. In this case, the equalization behavior will repeat in the following cycles and the charges are transferred from *Cell 1* to *2* gradually. The quantitative analysis of this circuit will be presented in the following section.

### 4.2.3 Quantitative Analysis

**(1) Governing equations of $i_1$:**

When $i_1 \geq 0$, it is governed by

$$\begin{cases} L_1 i_1'(t) + R_1 i_1(t) - V_1 = 0 & t \in [0, T_0] \\ CL_1 i_1''(t) + CR_1 i_1'(t) + i_1(t) = 0 & t \in (T_0, T_s] \end{cases} \tag{4.1}$$

once $i_1 < 0$, it will limited to 0 by $D_2$. The initial and jumping conditions are given by

$$\begin{aligned} & i_1(0) = 0 \\ & i_1'(0) = V_1/L_1 \\ & i_1'(T_0 + 0^+) = \left[V_1 - R_1 i_1(T_0) - V_C(T_0)\right]/L_1 \end{aligned} \tag{4.2}$$

**(2) Governing equations of $i_2$:**

When $i_2 \geq 0$, it is governed by

$$\begin{cases} CL_2 i_2''(t) + CR_2 i_2'(t) + i_2(t) = 0 & t \in [0, T_0] \\ L_2 i_2'(t) - R_2 i_2(t) + V_2 = 0 & t \in (T_0, T_s] \end{cases} \tag{4.3}$$

once $i_2 < 0$, it will limited to 0 by $D_2$. The initial and jumping conditions are given by

$$\begin{aligned} & i_2(0) = 0 \\ & i_2'(0) = V_1/L_2 \\ & i_2'(T_0 + 0^+) = \left[R_2 i_2(T_0) - V_2\right]/L_2 \end{aligned} \tag{4.4}$$

**(3) Governing equations of $V_C$:**

$$V_C(t) = \begin{cases} V_C(0) - \frac{\int_0^t i_2(x)dx}{C} & t \in [0, T_0] \\ V_C(T_0) + \frac{\int_{T_0}^t i_1(x)dx}{C} & t \in (T_0, T_s] \end{cases} \tag{4.5}$$

with the initial condition

$$V_C(0) = V_1 + V_2 \tag{4.6}$$

Considering generally $R_1, R_2 \sim 10^{-2}\Omega$, $L_1, L_2 \sim 10^{-4}H$, and $C \sim 10^{-4}F$, the solutions of the above governing equations are given as:

**(1) Solution of $i_1$:**

$$i_1(t) = \begin{cases} \frac{V_1}{R_1} - \frac{V_1}{R_1} e^{-\frac{R_1}{L_1}t} & t \in [0, T_0] \\ e^{\alpha_1 t}\left[b_1 \cos(\beta_1 t) + b_2 \sin(\beta_1 t)\right] & t \in (T_0, T_{11}] \\ 0 & t \in (T_{11}, T_s] \end{cases} \tag{4.7}$$

where

$$\begin{aligned} \alpha_1 &= -\frac{R_1}{2L_1} \\ \beta_1 &= \frac{\sqrt{4CL_1 - R_1^2C^2}}{2CL_1} \\ b_1 &= \frac{\beta_1 i_1(T_0)\cos(\beta_1 T_0) - i_1'(T_0)\sin(\beta_1 T_0) + \alpha_1 i_1(T_0)\sin(\beta_1 T_0)}{\beta_1 e^{\alpha_1 T_0}} \\ b_2 &= \frac{\beta_1 i_1(T_0)\sin(\beta_1 T_0) + i_1'(T_0)\cos(\beta_1 T_0) - \alpha_1 i_1(T_0)\cos(\beta_1 T_0)}{\beta_1 e^{\alpha_1 T_0}} \\ T_{11} &= \frac{1}{\beta_1}\arctan(\frac{-b_1}{b_2}) \end{aligned} \tag{4.8}$$

**(2) Solution of $i_2$:**

$$i_2(t) = \begin{cases} e^{\alpha_2 t}\frac{V_1}{\beta_2 L_2}\sin(\beta_2 t) & t \in [0, T_0] \\ \frac{V_2}{R_2} + Ae^{\frac{R_2}{L_2}t} & t \in (T_0, T_{12}] \\ 0 & t \in (T_{12}, T_s] \end{cases} \tag{4.9}$$

where

$$\begin{aligned} \alpha_2 &= -\frac{R_2}{2L_2} \\ \beta_2 &= \frac{\sqrt{4CL_2 - R_2^2C^2}}{2CL_2} \\ A &= e^{-\frac{R_2}{L_2}T_0}\left[i_2(T_0) - \frac{V_2}{R_2}\right] \\ T_{12} &= T_0 + \frac{L_2}{R_2}\ln\frac{-V_2}{R_2 i_2(T_0) - V_2} \end{aligned} \tag{4.10}$$

**(3) Necessary conditions:**

The above solutions are subjected to the following necessary conditions. When design a controller, $D$ and $f_s$ must satisfy them.

a. To assure *Cell 2* is charged in $Q_1$ on period: $T_0 \leq \pi/\beta_2$;

b. To assure *Cell 1* is still discharged after $T_0$: $T_{11} > T_0$;

c. To assure *Cell 2* is still charged after $T_0$: $T_{12} > T_0$;

d. To assure $i_1(T_s) = 0$: $T_s \geq T_{11}$;

e. To assure $i_2(T_s) = 0$: $T_s \geq T_{12}$.

### 4.2.4 Implementation of an Equalizing Circuit

To implement an equalizing circuit for the mentioned 6Ah cells, we select equalizing parameters $L_1 = L_2 = 100\mu H$, $C = 470\mu F$ and $D = 0.45$. Although the internal resistances of cells will change along with their SoCs, in

this subsection, $10m\Omega$ is used as a typical value to facilitate the following discussion.

The control frequency $f_s$ is utilized as the control variable of the equalization system. Given $f_s = 5kHz$, the typical current and voltage curves in two successive $Q_1$ control cycles are shown in Fig.4.5. It is clear that the dynamics of the equalization system satisfy the theoretical analysis. One remarkable feature of the dynamics is the small difference between $i_1$ and $i_2$, which causes the current curves not to overlap completely. The difference is due to the energy lost on the internal resistors of cells. The charge drawn from *Cell 1* is always larger than that transferred into *Cell 2*. Therefore, the ratio of $i_2$ to $i_1$ can be used as an indicator of equalizing efficiency. As shown in Fig.4.6, the smaller the control frequency, the larger the equalizing current . Hence, the energy loss on internal resistors increases, resulting in lower energy efficiency. In practice, capacitors, inductors, and MOSFETs also cause energy loss and so energy efficiency is less than that given in the simulations.

## 4.3 State of Charge based Fuzzy Control

Based on the equalizing circuit with the parameters given above, the equalizing process can be driven by the control frequency to MOSFET. Besides the speed of the equalizing process, the performance of an equalizer is also evaluated by the equalizing efficiency and the protection of cells. Therefore, a fixed control frequency is insufficient to achieve a satisfactory overall performance. Given the states of cells, how to tune the control frequency,

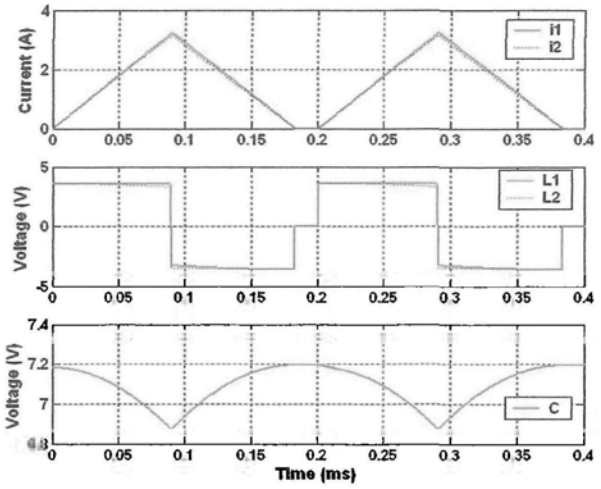


Figure 4.5: The current and voltage curves in two successive MOSFET control cycles ($f_s = 5kHz$, $SoC_1 = 0.6$, $SoC_2 = 0.5$).

and equally how to tune the equalizing current, becomes the key issue in equalizing system design.

### 4.3.1 Selection of Inputs

Generally, the selection of inputs of a controller should reflect the relevant factors, based on which the controller can determine an optimal, or at least a suitable, value of control variable. The relevant factors affecting equalizing performance in this study are equalizing speed, efficiency and cell protection. Therefore, three corresponding cell states are utilized as the inputs.

#### The difference in SoC ($\Delta SoC = |SoC_1 - SoC_2|$)

The aim of battery equalization is for all cells to possess the same SoC. Cell imbalance is essentially the SoC imbalance rather than a voltage imbalance. A large $\Delta SoC$ indicates a serious situation and requires a comparatively

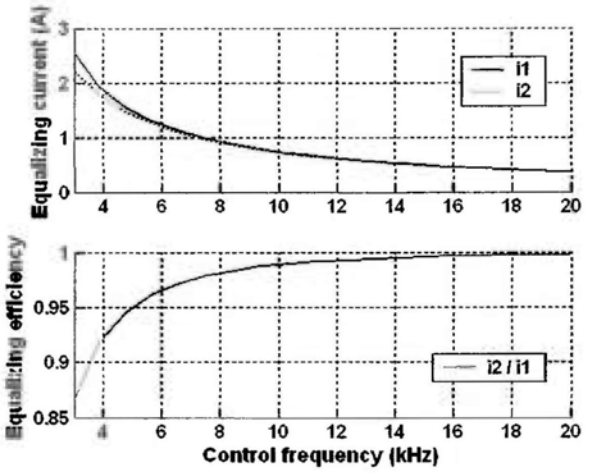


Figure 4.6: The average equalizing currents and equalizing efficiencies of various control frequencies ($SoC_1 = 0.6$, $SoC_2 = 0.5$). The energy efficiency only consider the energy loss on resistors.

large equalizing current to accelerate the equalizing speed. A difference in SoC larger than 30% is treated as a malfunction and at least one cell has to be replaced. In contrast, a small difference represents a slight imbalance that does not need to be equalized urgently. In this situation, the equalizing process can focus more on equalizing efficiency. In practice, limited by the accuracy of SoC estimation, a difference in SoC less than 2% is small enough to be recognized as equal. In other words, this input mainly determines the equalizing speed.

### The average of SoC ($\overline{SoC} = \frac{1}{2}(SoC_1 + SoC_2)$)

The transferring equalization method is to charge one cell by discharging the other one, therefore discharging ability should be taken into consideration. An overlarge equalizing current, intended to accelerate the equalizing speed, may cause damage to a discharging cell with a low SoC. The average SoC

represents the level of residual capacity. Therefore, it is used to indicate whether a large equalizing current is allowed. Usually, if the average SoC is less than 0.15, cells are in a very low state and a large equalizing current is strictly forbidden. Simply speaking, the second input chiefly focuses on the protection of cells.

**The total internal resistance ($\Sigma R = R_1 + R_2$)**

As shown in Fig.4.2, the internal resistance varies according to the SoC. Meanwhile, as discussed previously, the resistance causes energy loss in the equalizing process. Therefore, a simple way of enhancing the equalizing efficiency is to apply a large current when the total internal resistance is small, and apply a small current in the opposite situation. Thus, the third input focuses on energy efficiency.

### 4.3.2 Implementation of Fuzzy Controller

Based on the inputs proposed above, a controller should map the input vector to a control frequency, i.e. establish a function $F : f_s = F(\Delta SoC, \overline{SoC}, \Sigma R)$. However, due to the lack of quantitative analysis and modeling of the relationships among these variables, it is hard to design a controller based on traditional methods. In contrast, the inputs can easily be qualitatively classified into different levels and expressed as linguistic variables, such as large, small, and so on. There is, therefore, a strong rationale for applying fuzzy control to determine the equalizing current.

In general, a fuzzy controller consists of the membership functions of inputs and outputs, a rule database, and inference methods [101]. The infer-

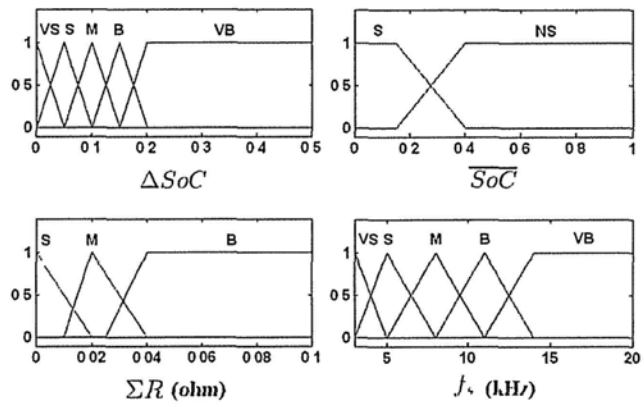


Figure 4.7: The membership functions of input and output variables in the proposed fuzzy controller

Table 4.1: Rules database in the proposed fuzzy controller.

| $f_s$ | $\overline{SoC}$ | S | | | NS | | |
|---|---|---|---|---|---|---|---|
| | $\Sigma R$ | S | M | B | S | M | B |
| $\Delta SoC$ | VS | VB | VB | VB | M | B | VB |
| | S | B | VB | VB | S | M | B |
| | M | M | B | VB | VS | S | M |
| | B | S | M | B | VS | VS | S |
| | VB | VS | S | M | VS | VS | VS |

ence methods are the same as the default settings in the fuzzy logic toolbox given by Matlab. As shown in Fig.4.7, the membership functions of inputs and outputs are based on the experiences and basic knowledge of cell equalization, where VS=very small, S=small, M=middle, B=big, VB=very big, and NS=not small. The rule database is provided in Tab.4.1 and hence the typical decision surfaces when $\overline{SoC} = 0.15$ and $\overline{SoC} = 0.4$ are shown in Fig.4.8.

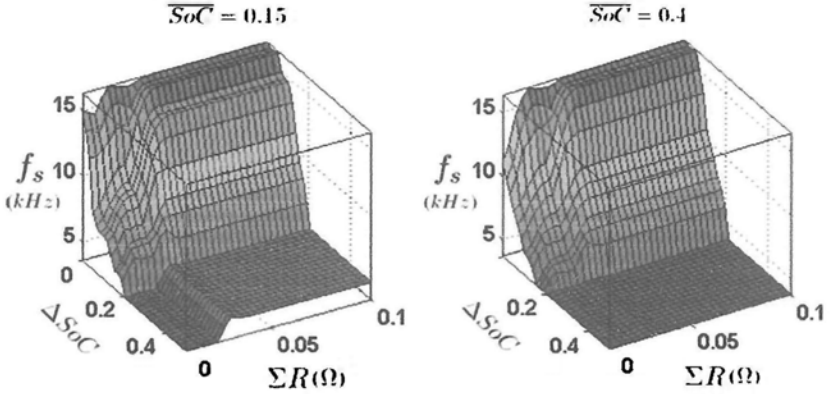


Figure 4.8: The decision surface in the proposed fuzzy controller. Left: fix $\overline{SoC}$ to absolute S; right: fix $\overline{SoC}$ to absolute NS.

## 4.4 Performance Demonstration

### 4.4.1 Simulation Results

To demonstrate the availability and efficacy of the proposed equalizing system, simulations are conducted using the 6Ah battery model with features as shown in Fig.4.1 and 4.2. The control period of the fuzzy controller is set to one second. During each second, the variation in cell states is small enough to be ignored so that only one MOSFET control cycle needs to be calculated, based on the given $f_s$, and the following $f_s - 1$ cycles will repeat the same dynamics. Thus, the total quantity of electricity transferred in one second equals $f_s$ times that in any one cycle. Based on the accumulated variations, the SoC can be updated every second and cell terminal voltages and internal resistances are changed according to their respective characteristic curves, as indexed by SoC. In the fuzzy controller, the inputs $\Delta SoC$, $\overline{SoC}$, and $\Sigma R$ are also calculated every second. Consequently, the MOSFET control frequency $f_s$ will be tuned to realize an adaptive control and reach a satisfactory overall

equalizing performance. The simulation temperature is fixed to $25^oC$. Considering the accuracy of SoC estimation in practice, the equalizing process will terminate when the SoC difference is smaller than 2%.

Four typical equalizing processes are illustrated in Fig.4.9.

The first two rows show the results under the initial conditions of $SoC_1 = 0.2$, $SoC_2 = 0.1$ and of $SoC_1 = 0.9$, $SoC_2 = 0.8$. Both of them are initialized with a comparatively small SoC difference. Although the $\Delta SoC$ is the same in the beginning, the large total resistance and the limited discharging ability of low SoC cells restrict the equalizing current smaller than that in the situation of high SoC level. Therefore, the equalizing period in the low SoC situation is longer, but with the benefit of high energy efficiency.

The last two rows increase the SoC differences to 30% and test whether the proposed controller is able to quickly alleviate the large imbalance, which, without proper equalization, risks damaging the cells by overcharging or overdischarging. From the curves, it is clear that the equalizer initially applies a large equalizing current (around 0.4C for the high SoC situation, 0.3C for the low SoC situation) to balance cells as quickly as possible. At this stage, energy efficiency is not a consideration because it is less of a priority than the safety and performance of the cells. Along with the reduction in SoC difference, the current gradually becomes smaller to emphasize energy efficiency. Therefore, the later phases are similar to the equalizing process shown in the first two rows.

Although only four situations are shown in this paper, we actually conducted a large number of simulations to test the performance of the proposed equalizer. The four situations illustrate the extreme results, while tests under

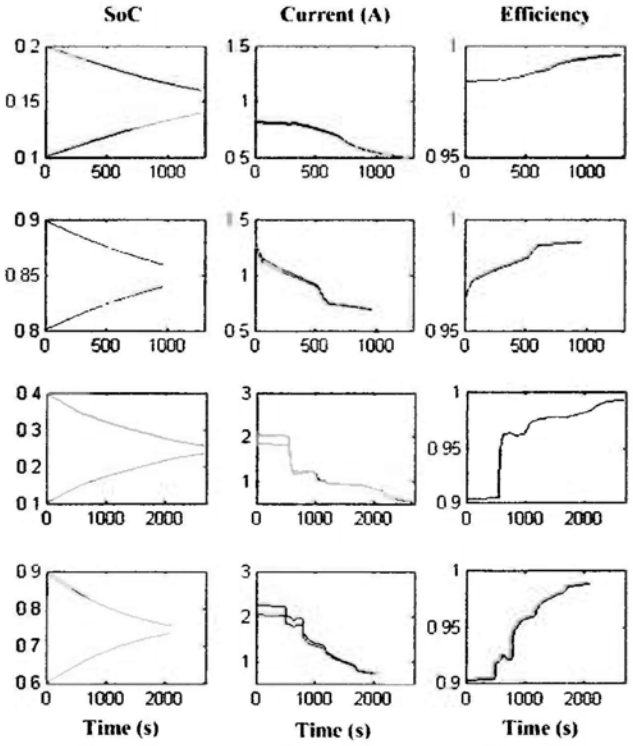


Figure 4.9: The simulation results under various initial conditions. Each row shows curves of SoC, equalizing current and energy efficiency under the same initial conditions.

average conditions obtained moderate results. The self-adaptive ability and multiple considerations of equalizing speed, efficiency, and cell protection are well verified by the finding that any imbalance less than a 30% SoC difference can be equalized in less than one hour, and the average energy efficiencies are almost all above 0.95. The worst result among our tests was 0.9493.

### 4.4.2 Experiment Results

In experiments, we also applied the equalization method to equalize two capacity-extended cells. The SoC of each cell is estimated using the method

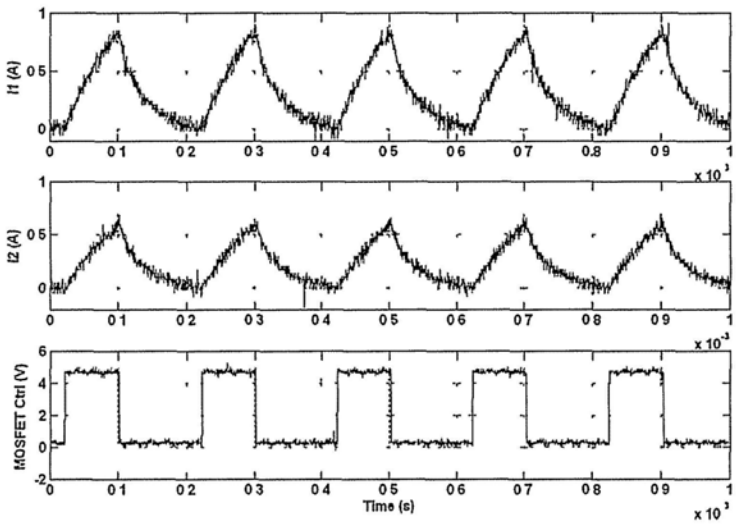


Figure 4.10: Equalizing cycles when control frequency of MOSFET is 5k

proposed in Chapter 3. Charging and discharging resistances are also modeled in Chapter 3.

Fig. 4.10 and Fig. 4.11 show the equalizing cycles when the control frequencies of MOSFET are 5k and 20k respectively, obtained by oscillograph. Compared with the theoretical situation, the equaling current and equalizing efficiency are both smaller. Fig. 4.12 illustrates the average equalizing currents and equalizing efficiencies of various control frequencies in the experiments.

In the experiments, we applied three extended cells to test the performance under different initial conditions. Fig. 4.13 and Fig. 4.14 show the equalizing processes of high and low initial SoC conditions respectively. The SoC curve is estimated by the method proposed in Chapter 3. Limited by the accuracy of SoC estimation in the experiment, we stop the equalization process when the largest SoC difference is below 5%. It is clear that, because

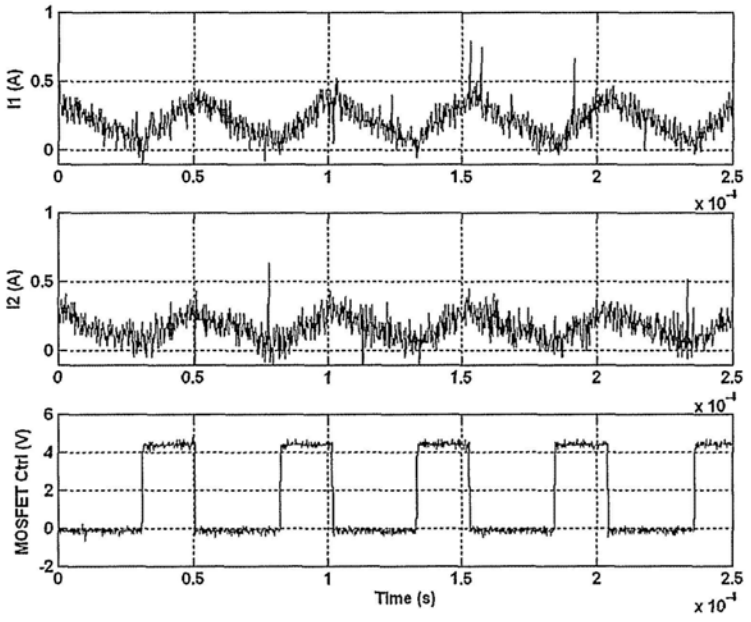


Figure 4.11: Equalizing cycles when control frequency of MOSFET is 20k.

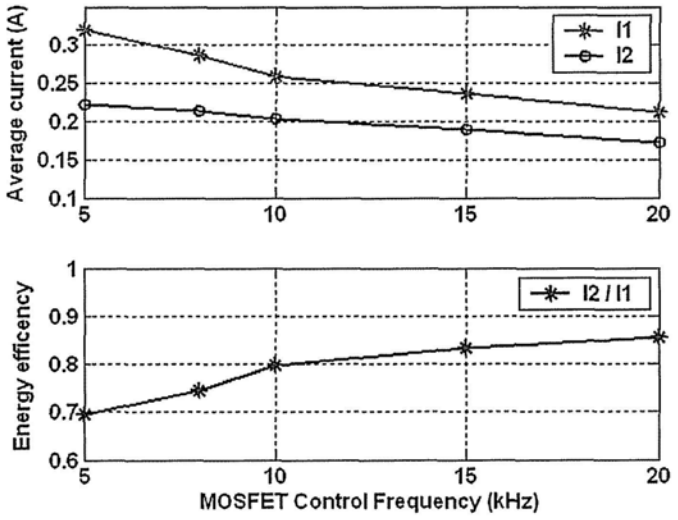


Figure 4.12: The average equalizing currents and equalizing efficiencies of various control frequencies in experiments.

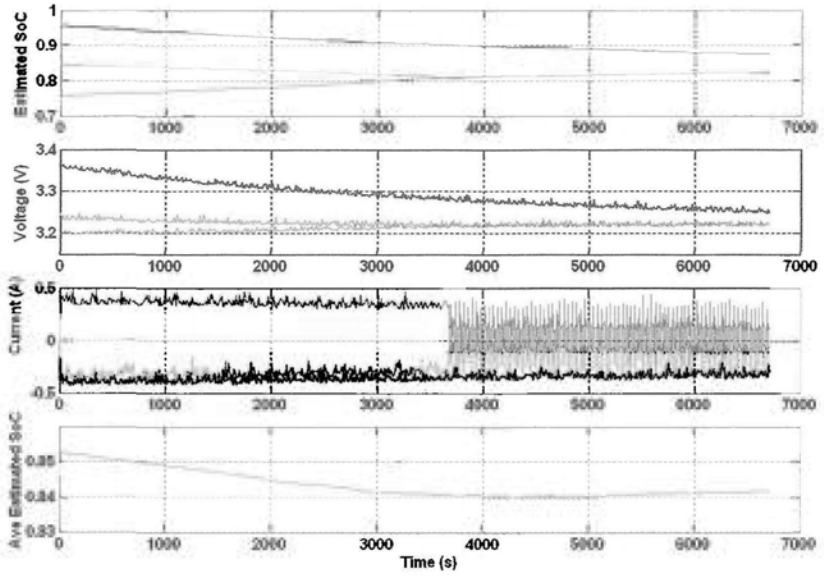


Figure 4.13: Equalization process in experiment with high SoC initial condition (SoC=0.95,0.75,0.85).

the total internal resistance in the low SoC condition is greater than that in the high SoC condition, and the discharge ability of the cell with a low SoC is worse than that of a high SoC cell, the equalizing current is smaller in the low SoC situation so as to generate less heat and protect cells.

The more significant performance is shown in Fig. 4.15, which illustrates the equalizing process in middle SoC condition. Since LiFePO4 has a very flat SoC vs. OCV relationship, the large 20% SoC imbalance only causes around 20mV difference in voltage. Along with the equalizing process, the voltage difference gradually becomes smaller than the error of the voltage measurement, which is around 8mV in the experiment. Such a small voltage difference cannot be handled by the existing voltage-based fuzzy controllers. Our method applies the SoC rather than the voltage as the input to the fuzzy controller and successfully solves the equalization problem for the LiFePO4

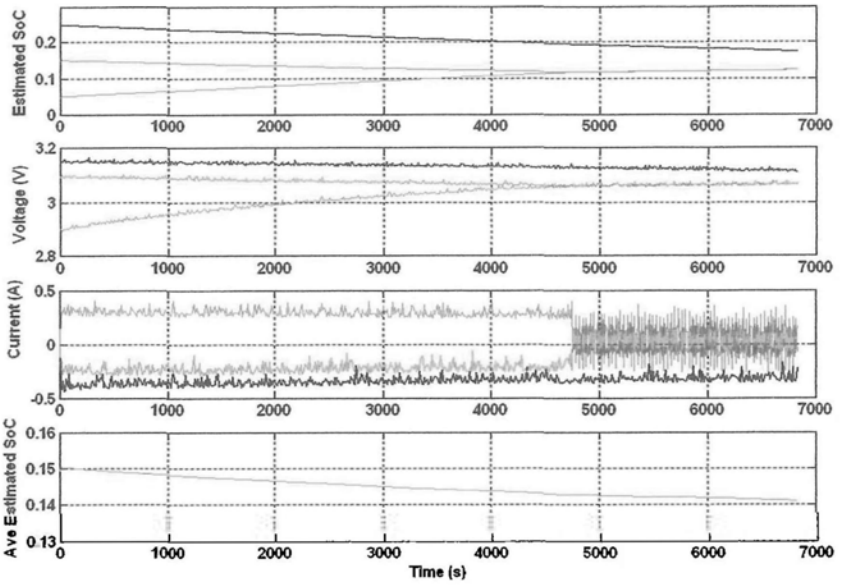


Figure 4.14: Equalization process in experiment with high SoC initial condition (SoC=0.25,0.05,0.15).

battery.

## 4.5 Summery

Based on the analysis of the equalizing circuit implemented by the *Cûk* converter, we have established a fuzzy controller to adaptively tune the MOSFET control frequency and to tune the equalizing current. The overall performance of the proposed equalizer is evaluated by its equalizing speed, efficiency, and cell protection, indicated by the three controller inputs - SoC difference, total internal resistance, and average SoC, respectively. The membership functions and rules database are established based on experience and the knowledge of experts, as well as the characteristics and abilities of cells. Simulations under various initial conditions are conducted to demonstrate

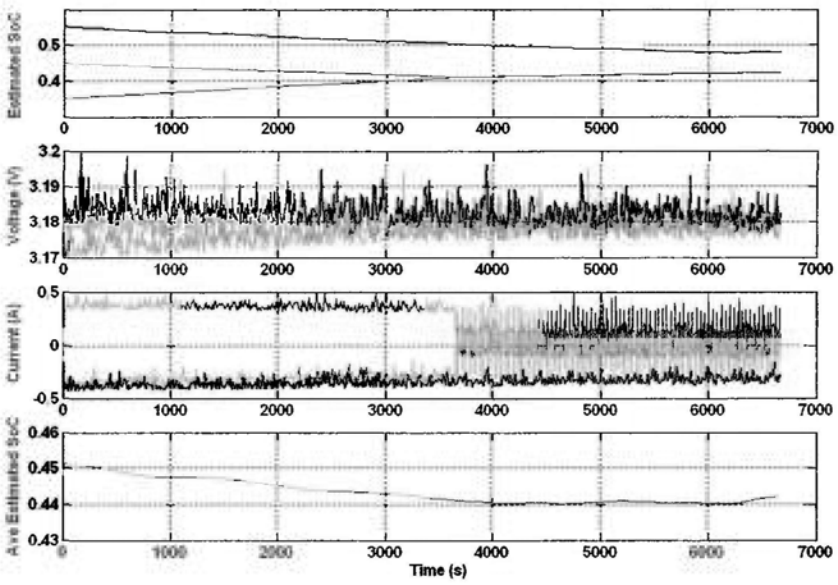


Figure 4.15: Equalization process in experiment with middle SoC initial condition (SoC=0.55,0.35,0.45).

the availability and efficacy of the proposed equalizer. The results verify that it can self-adaptively achieve satisfactory overall performance, within a limited equalizing period and with high energy efficiency. Experimental results also demonstrate that the proposed method is able to equalize the LiFePO4 battery, which has a very flat SoC vs. OCV relationship.

---

**□ End of chapter.**

# Chapter 5

# Model Predictive Control based Fast Charge

## 5.1 Introduction

It is necessary to refuel vehicles after a period of travel. For conventional fuel-driven vehicles, the fuel can be replenished fast and safely at filling stations, with an ignorable out-of-service time and without energy loss. However, the replenishment of energy in electric vehicles requires to charge the battery pack. In general applications, such as MP3 players, shavers, cell phones, the charging process lasts for several hours, leading to a long out-of-service time. The charging method is also crucial; an unsuitable method leads to high temperature increase in battery and even runs the risks of fire and explosion.

Therefore, charging control is another significant issue in battery management systems, with the aim of feeding external energy into batteries in a fast, safe, and efficient way. Fast charging helps to reduce out-of-service

time and promote the commercialization of EVs. Safe charging not only assures the safety of users by preventing battery burning and explosion during the charging process, but also prolongs the battery life by preventing overcharging and overheating damage. Efficient charging can convert as much electrical energy as possible from a charger to electrochemical energy stored in a battery to enhance energy efficiency.

### 5.1.1 Literature Review

Charging methods have been studied since the invention of rechargeable batteries. The earliest and simplest method is to charge using a constant trickle current (CTC) [102]. This method has a simple circuit structure and very low cost and so has been adopted in most electronic products for many years. However, due to the very small current, charging time is extremely long so it usually works overnight. An easy way to reduce the charging time is to increase the constant current (CC). Charging with 1C current can fill an empty battery in one hour. However, this method requires a very precise state of charge (SoC) estimator to determine when the battery is fully charged and stop the charging process. Another disadvantage is that CC charging cannot avoid overvoltage to the battery. A battery can be simply modeled with an open circuit voltage (OCV) source and a series-connected resistor. The voltage on the resistor during CC charging will cause the terminal voltage to be always higher than the OCV, finally leading to overvoltage when the OCV approaches its full value. Taking a Li-ion battery as an example, the overvoltage during charging will degrade the crystallographic structure of the cathode and cause oxidative decomposition of the electrolytic solvents [103].

To overcome the disadvantages of CC charging, the constant current constant voltage (CCCV) method has been proposed. In the following CV period, after the charging voltage reaches a predetermined value in the CC period, the charging voltage is fixed to a cutoff value and the charging current will be automatically reduced along with an increase in the SoC. However, the CV period usually requires a long charging period [104]. Various combinations of CC and CV periods have also been proposed to improve charging performance, such as CCCVCV [105], $(CCCV)^2$ [106], and so forth.

In recent years, microprocessor control units (MCUs) have been applied in battery management systems, allowing the monitoring and estimation of battery states, based on which intelligent methods can be implemented to control the charging process. The first kind of intelligent charger controls the charging process based on the detection of tuning points. The tuning points are selected as the threshold points, stationary points, and inflection points of battery voltage, temperature, and lapsed time [107–109]. These methods only change the charging behavior at tuning points and the periods between tuning points are still in open-loop control. Fuzzy control has been also utilized to solve the charging control problem. In [104], the fuzzy controller replaces the usual CV mode in the CCCV charging method. Neural networks and genetic algorithms are also introduced to design the membership functions and inference rules of the fuzzy controller [110–112]. Optimization methods, including an ant colony algorithm and evolutionary algorithm, have also been introduced to optimize a best multi-stage CC charging profile [113,114]. The optimization aims to find a best charging profile covering the whole charging process and does not regulate the realtime charging current according to

instant system measurements. Therefore, its performance is seriously dependent on the accuracy of the model used in optimization and its robustness is weak, suffering from system noise and the time-variant properties of the battery. A grey-predicted control system is employed to increase the charging speed without taking temperature increases into consideration [115]. In addition, only a one-step prediction is utilized in that study. The smallest predictive horizon weakens the prediction of future system behavior.

### 5.1.2 Overview of Proposed Charging Controller

In recent years, much effort has been devoted to establishing battery models, some of which are demonstrated to be accurate and efficient at modeling the behavior of batteries [54–58]. These models make it possible to apply model predictive control (MPC) to management of the battery charging process.

MPC is a typical advanced control method and is widely utilized in many fields [116,117]. It is based on the principle of using a system model to predict system responses to possible future control inputs, and find the best future control sequence to optimize the user-defined objective function. Only the first step of the control sequence is applied at each time. The system states are then sampled again and the calculations are repeated at the next control time. The prediction horizon is constantly shifted forward. Since the receding horizon strategy updates predictions based on the instant measurement of system inputs and outputs at each control time, its robustness has been demonstrated to be strong [118]. Depending on the linearity of the system models and constraints, MPC may be categorized as either linear MPC or nonlinear MPC. For linear MPC, the best control sequence can be analyt-

ically obtained by solving Diophantine equations. However, for nonlinear MPC, the best control sequence can generally be numerically calculated only under an optimization framework [119].

As shown in Fig.5.1, the fast charging control framework proposed in this work consists of the following components:

1. a SoC predictor, predicting the SoC of battery when feeded by a sequence of future charging current;

2. a temperature predictor, predicting the future battery temperature under the sequence of charging current;

3. a fitness evaluator, evaluating the performance of the sequence of charging current;

4. an optimizer, finding the best sequence of charging current using genetic algorithm (GA).

## 5.2 Predictive Models

To utilize predictive control, battery models are needed to predict future states exerted by a sequence of future charging current. The relevant battery states in this study are SoC and temperature. The former indicates the charging speed and whether overcharge damage is possible, while the latter represents the safety of the charging process and the amount of lost energy converted to heat. Charging control is necessary to, (1) maximize charging speed, (2) minimize temperature increases, and (3) restrict temperature to a safe range.

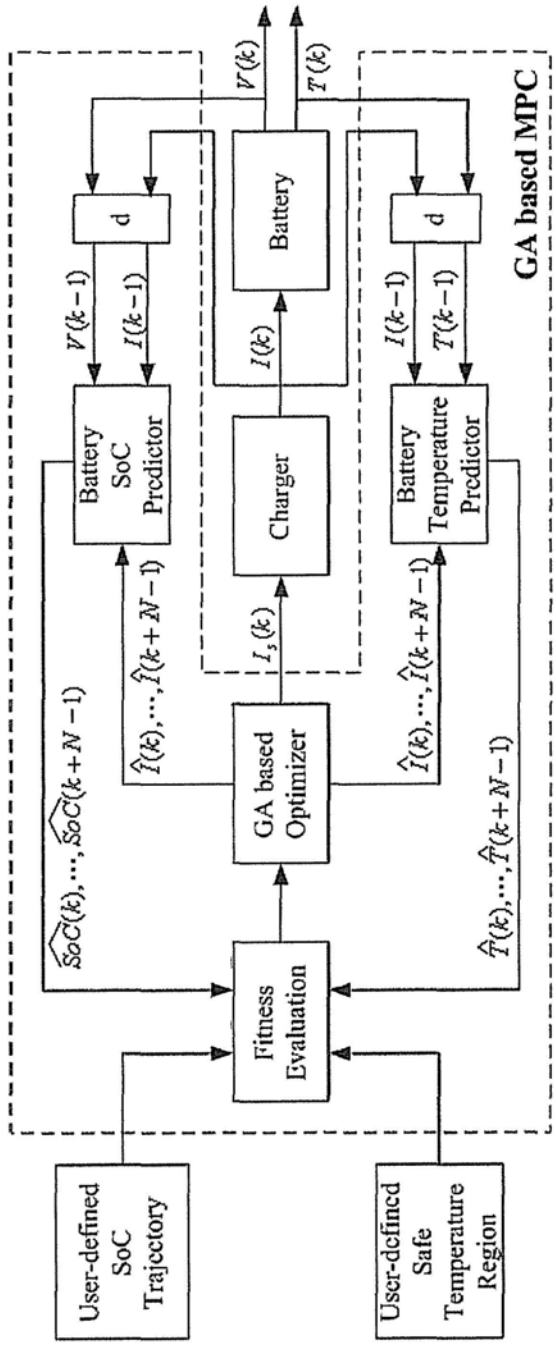


Figure 5.1: Fast charging control framework based on model predictive control.

The RC model and modified ESC model both have the ability to predict the battery's SoC based on a given future current. Therefore, we directly apply them in our simulation and experiment, respectively.

### 5.2.1 Thermal Model in Simulation

A simple, single-node lumped-parameter thermal model has been established in [120]. It models the thermal process in three stages. In the first stage, the Joule effect generates heat in the battery. In the second, the battery's heat is conducted and convected to the surrounding air. Finally, the surrounding air exchanges heat with the ambient.

In the RC model, the heat generation is expressed by:

$$Q_g(k) = T_s \left[ I_o^2(k) R_o(k) + I_s^2(k) R_s(k) + I_b^2(k) R_b(k) \right] \tag{5.1}$$

where

$$\begin{aligned} I_o(k) &= I(k) \\ I_b(k) &= \frac{V_b(k) - V_s(k) + R_s(k) I(k)}{R_s(k) + R_b(k)} \\ I_s(k) &= I_b(k) - I(k) \end{aligned} \tag{5.2}$$

Meanwhile, the heat passing from the battery to the surrounding air is expressed by:

$$Q_p(k) = \frac{T(k-1) - T_{air}(k-1)}{R_{eff}} \tag{5.3}$$

where the $T_{air}$ is the effective temperature of surrounding air and $R_{eff}$ is the effective thermal resistance.

Based on the assumption that that 50% of the heat from the battery is

spent to warm the air, $T_{air}$ is expressed by

$$T_{air}(k-1) = T_{amb} - \frac{0.5 \times Q_p(k-1)}{\dot{m}_{air} C_{air}} \tag{5.4}$$

where $T_{amb}$ is the ambient temperature, $Q_p(k-1)$ is the passing heat in previous step, $\dot{m}_{air}$ is the airflow rate, and $C_{air}$ is its heat capacity.

Strictly speaking, $R_{eff}$ will vary depending on the thermal control method; for example, it will become smaller if the cooling fans are open. However, in this study, we assume the charging process is conducted in an environment with only natural convection and no thermal control device. In this case, $R_{eff}$ is fixed as a constant with the value calculated by:

$$R_{eff} = \frac{1}{hA} + \frac{t}{kA} \tag{5.5}$$

where $h$ is the heat transfer coefficient in the natural environment, $A$ is the total module surface area exposed to the air, $t$ is the thickness of the module case, and $k$ is the thermal conductivity of the module case material.

$Q_g(k)$ indicates the heat generation which heats the battery, while $Q_p(k)$ represents the heat loss which cools the battery by heating the surrounding air. Therefore, the battery temperature $T(k)$ can be calculated by:

$$T(k) = T(k-1) + \frac{Q_g(k) - Q_p(k)}{m_{bat} C_{bat}} \tag{5.6}$$

where $m_{bat}$ is the battery mass and $C_{bat}$ is its heat capacity.

### 5.2.2 Thermal Model in Experiment

The simulation model requires many physical parameters for the battery and working environment. However, in practice, these parameters cannot usually be obtained accurately. Meanwhile, the theoretical model only considers the ideal situation, which may not be suitable for the complex and nonlinear electrochemical process inside the battery. Furthermore, heat generation is only caused by heating of the resistors, which does not fully represent the actual situation. In reality, heat generation during charge is also affected by the charging acceptance rate. [106] pointed out that "close-to-fully discharged batteries can be recharged with very high currents for a short period of time." and [121] concluded that for A123, a kind of LiFePO4, "at a low state of charge, nearly all the charging current is absorbed by the chemical reaction. Above 80% of SOC, more and more energy goes into heat".

Fig. 5.2 shows the temperature curves of our experimental cell during charge processes with different charging rates. The increasing temperature trend agrees with the two results reported in the literature above. Another two extended cells are also tested, resulting in similar curves.

Besides the SoC, increasing temperature obviously has a close relationship with the charging rate. High charging rates will cause high temperature rises. Therefore, in practice, we select the SoC, charging rate, and current temperature to predict the future temperature, based on a neural network (NN) trained by the data from three extended cells.

Fig. 5.3 shows the structure of the NN implemented to predict temperature. The training method is back propagation (BP) learning. When the time step is set to 30s, the average prediction error is 3.36% and the maximum is

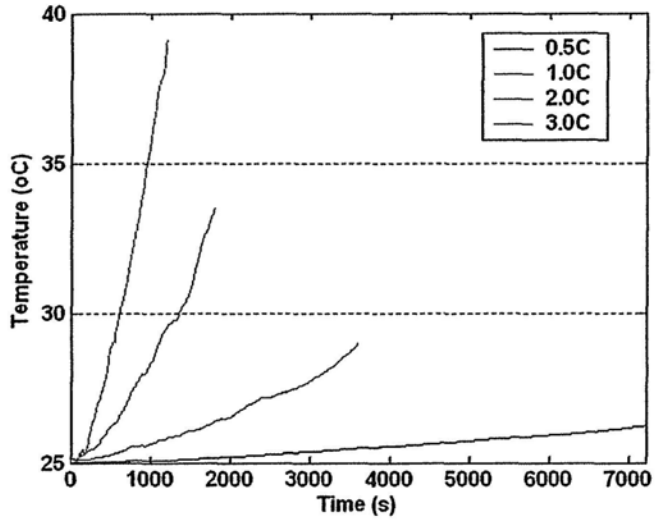


Figure 5.2: Temperature rising during various charging rates.

5.43%.

### 5.2.3 Model based Prediction

In addition to the models above, to predict battery states under a given sequence of future charging current, two problems still need to be solved: (1) how to initialize the prediction at time $k$, and (2) how to realize the multi-step prediction using a one-step predictive model.

To initialize the prediction at time $k$, the RC model requires the last system state $x(k-1)$, last input $u(k-1)$, and the model parameters at time $k$. Since $u(k-1)$ and $y(k-1)$ are both available from the current sensor and voltage measurement respectively, $x(k-1)$ can be estimated by closed-loop estimators such as the extended Kalman filter [59], sigma-point Kalman filter [63, 64], $H_\infty$ filter [122], and the robust SoC estimation framework proposed in Chapter 3. The closed-loop filters are able to eliminate

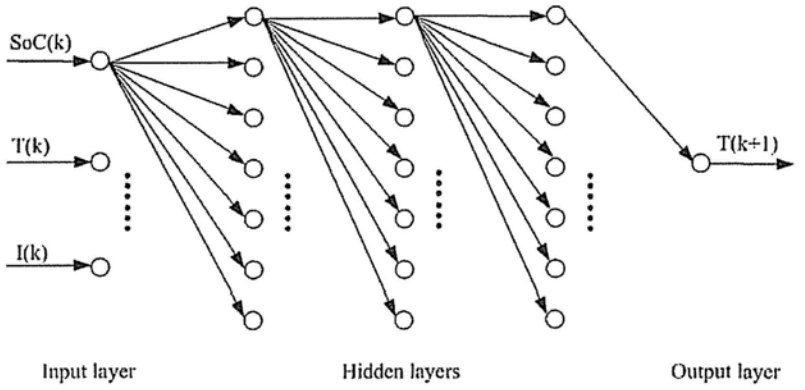


Figure 5.3: Neural network for predicting battery temperature.

accumulated errors and the estimation result will gradually converge to the real value, or to a limited error range. The model parameters are stored in a look-up table indexed by SoC and temperature. The slow change in both SoC and temperature is the reason for updating the model parameters at time $k$ according to $SoC(k-1)$ and battery temperature $T(k-1)$, especially when the $T_s$ is comparatively small. $SoC(k-1)$ is estimated by the method proposed in Chapter 3 and $T(k-1)$ is measured directly from a temperature sensor fixed on the surface of the battery.

The above preparation allows a one-step prediction of $SoC(k)$ and $T(k)$, given the value of $I(k)$. However, a single-step prediction is usually insufficient to predict system behavior over a long process. Generally, the prediction horizon in MPC is more than one step. Therefore, a multi-step predictor is necessary to predict system states exerted by a sequence of future charging current. A simple way to realize the multi-step predictor is an iterative prediction, using the predictive future system states at time $k+j$ as the initial state for the next time $k+j+1$.

In summary, at control time $k$, the SoC model and temperature model can iteratively map a sequence of future charging current $[I(k), I(k+1), \cdots, I(k+P-1)]$ to future battery states $[SoC(k), SoC(k+1), \cdots, SoC(k+P-1)]$ and $[T(k), T(k+1), \cdots, T(k+P-1)]$. The multi-step prediction uses an open-loop method in which each step suffers from the prediction error of the previous step and finally reverts to the errors in the initial values at time $k-1$. Fortunately, these initial values are estimated in a closed-loop manner so that initial errors are limited to be small. In reality, any battery management system requires such an estimator to obtain the realtime SoC and measure the battery temperature. The results can be used as the initial values.

## 5.3 Formulation under MPC Framework

Given a series of control inputs, the length of which is denoted as the prediction horizon $P$, the future system states can be predicted based on a dynamic system model. The future system behavior under the sequence of inputs can then be evaluated based on a performance index. At each control time $k$, the basic idea of MPC is to find an optimal sequence of control inputs $[\hat{u}(k), \hat{u}(k+1), \cdots, \hat{u}(k+P-1)]$, which optimizes the performance index, and apply the first element of the input sequence $\hat{u}(k)$ to the system as the current control variable.

In the charging control problem, MPC optimizes a sequence of future charging current $[\hat{I}(k), \hat{I}(k+1), \cdots, \hat{I}(k+P-1)]$, which has the best performance index based on the predicted battery states $[\widehat{SoC}(k), \widehat{SoC}(k+$

$1), \cdots, \widehat{Soc}(k+P-1)]$ and $[\hat{T}(k), \hat{T}(k+1), \cdots, \hat{T}(k+P-1)]$.

### 5.3.1 Performance Indexes

The performance index reflects the control objectives. The first objective is to maximize charging speed. However, since it is impossible to directly predict the total charging duration in a limited prediction horizon, we turn to the tracking of a user-defined SoC trajectory instead. A fast-rising SoC trajectory requires a fast charging speed while a flat one requires a slow speed.

The expected SoC trajectory can directly copy from any real charging trajectory controlled by any charging scheme. In addition, the expected trajectory can be set as a real trajectory with revisions based on certain special considerations. For example, for a CCCV trajectory, we may increase the charging speed when the SoC is in the middle and internal resistance is small. In addition, the expected trajectory can be designed entirely on the demands of the charging system.

To track the expected trajectory, a part of the performance index $J_1$ is expressed by

$$J_1 = |\widehat{SoC}(k+P-1) - SoC^*(k+P-1)| \tag{5.7}$$

where $SoC^*$ is the expected SoC trajectory. Evaluation of the SOC tracking performance is only based on the final prediction state because the SoC only needs to achieve the expected point in the final step. How this is achieved is not very important from the point of view of the charging process.

The second objective of charging control is to minimize the increase in temperature, which partially reflects energy efficiency and system safety. Assuming that the expected trajectory is copied from a CCCV charging process, without consideration of temperature, the best charging current sequence is the same sequence applied in the CCCV process. However, if we include evaluation of performance based on temperature, as expressed in $J_2$, the MPC will try to achieve the expected SoC point in the final step, by the process in which temperature rising is minimized.

$$J_2 = \max\{\hat{T}(k+j) - T(k-1) | j = 0, 1, \cdots, P-1\} \tag{5.8}$$

### 5.3.2 Constraints

Constraints in the charging process are designed to prevent a charging sequence that may cause damage to the battery or lead to dangerous events. The first constraint is that the SoC must not exceed 100%, to avoid overcharge damage. In practice, to reserve some tolerance, 98% SoC is treated as the full charging state. The second constraint is that temperature must be kept in a user-defined range to avoid overheating caused by overcharge or by a large charging current which exceeds the instant charging acceptance level. The two constraints are expressed by:

$$C_1: \quad \widehat{SoC}(k+j) \leq 98\% \tag{5.9}$$

and

$$C_2: \quad \hat{T}(k+j) \leq \bar{T}(k+j) \tag{5.10}$$

where $j = 0, 1, \cdots, P-1$ and $\bar{T}$ is the user defined safe range, which is designed either as a constant, indicating the highest temperature during the whole charging process, or as a time indexed function specifying the temperature limitation along with charging duration.

## 5.4 Optimization Using Genetic Algorithm

The MPC charging control problem is formulized to minimize the performance indexes $J_1$ and $J_2$, subject to the constraints $C_1$ and $C_2$. Essentially, the control problem is transformed into a constrained multi-objective optimization problem.

Generally, a multi-objective optimization problem can either be solved by multi-objective optimizers directly, or by first transforming it into a single-objective problem that is then solved by single-objective optimizers [123]. In this work, we apply the latter method because SoC tracking is more important than temperature management in the charging process, so the two objectives can be merged into one index by summing with different weights. To solve the optimization problem, a genetic algorithm (GA) is applied due to its strong global searching ability, without the requirement for derivative information of objective function. Since the two constraints should be strictly satisfied in the charging process to assure the safety and health of the battery, solutions that fail to satisfy any one of the constraints will be assigned the worst fitness.

Based on the above discussion, the fitness function to be minimized in

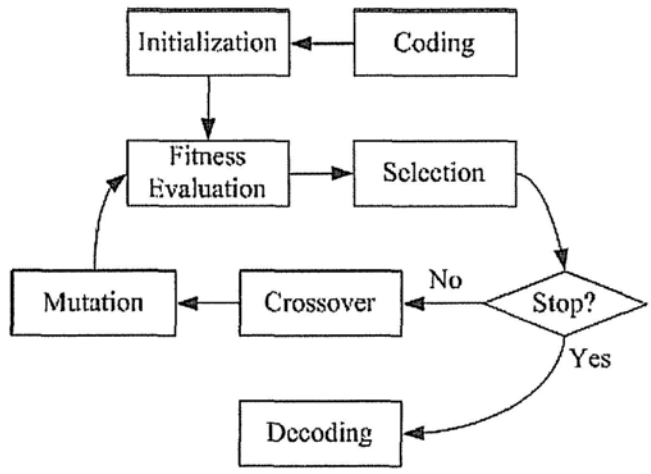


Figure 5.4: Scheme of the standard GA.

GA is expressed by

$$F = \begin{cases} \omega_1 J_1 + \omega_2 J_2 & (C_1 \textit{ and } C_2 \textit{ are held}) \\ +\infty & (\textit{otherwise}) \end{cases} \tag{5.11}$$

where $\omega_1$ and $\omega_2$ are the weights of $J_1$ and $J_2$

The minimization problem is solved by a standard GA. the scheme of which is illustrated in Fig. 5.4 and briefly described in the following steps.

*Coding.* The standard GA generally codes a candidate solution as a string of characters which are usually binary digits, referred to as a chromosome. The candidate solution is termed an individual. Accordingly, the set made up of a number of individuals is termed a population. In this chapter, we apply a real-value coding method, which codes a candidate solution as a set of floating decision variables. The real-value coding method is proven to have superior performance to the binary-coded method in control optimization problems [124].

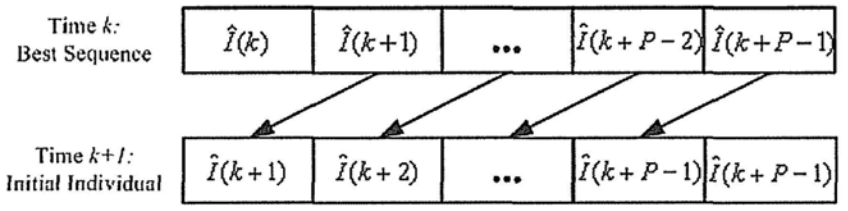


Figure 5.5: Initialization of one special individual by introducing the best control sequence optimized in last step into the present step.

*Initialization.* The standard GA starts with the generation of an initial population. Usually, individuals in the initial population are produced randomly. In MPC, the initialization process is executed at each control point to start the GA. Since the best control sequence optimized at time $k$ contains good candidates from $k+1$ to $k+P-1$, as shown in Fig. 5.5, one initial individual is specially designed by shifting it one time step and filling the last charging current with the same value as $\hat{I}(k+P-1)$. This individual introduces historical best charging sequence into the current optimization process, thus it is helpful to improve optimization performance to be at least very similar with the previous prediction.

*Fitness evaluation.* We can evaluate the fitness of each individual in each generation according to the equation (5.11). The smaller the fitness, the better the individual. However, to facilitate the following selection steps, the raw fitness is usually scaled to assign suitable selection pressure to each individual. In this work, the scale function is expressed as:

$$F_{scale} = \frac{1}{1+F^r} \tag{5.12}$$

where $r$ is power of raw fitness. A large $r$ will quickly increase the selection

pressure to a worse individual, accelerate the convergence speed, and increase the risk of premature especially for multi-peak landscape, and vice versa.

*Selection.* Individuals are selected from the last generation to the next generation based on the scaled fitness $F_{scale}$ following the *survival of the fittest* rule. Many selection methods have been developed to avoid genetic drift and premature phenomena. In this work, the roulette wheel selection method is adopted [125]. The elitism strategy is also applied in selection to assure that the best solution will never be lost.

*Crossover.* In the crossover step, the standard GA exchanges information between two parent individuals and produces two child individuals. In this work, the arithmetical crossover method is used. Given two parents $x_1$ and $x_2$, the children $y_1$ and $y_2$ are produced by linear combinations of parents with a random coefficient $\lambda \in R_\lambda$:

$$\begin{aligned} y_1 &= \lambda x_1 + (1-\lambda)x_2, \\ y_2 &= \lambda x_2 + (1-\lambda)x_1. \end{aligned} \tag{5.13}$$

*Mutation.* After the crossover step, a subset of individuals is selected with a mutation probability of $P_m$. To explore the search space, we use Gaussian mutation, which adds a random value from a Gaussian distribution with variance $\sigma$ to each item of the selected individual.

*Termination.* Many terminating conditions have been proposed to stop the iteration process, For example, when the distances among individuals are smaller than a predetermined value, an individual satisfies a minimum criterion, or the maximum number of generations is reached. The last method

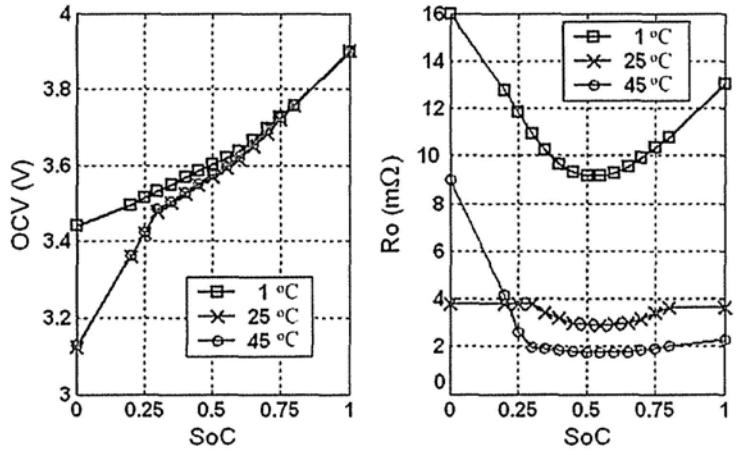


Figure 5.6: Battery time-variant properties. Taking OCV and $R_o$ as examples. Data source: Advisor.

is applied here.

## 5.5 Performance Demonstration

### 5.5.1 Settings

To evaluate the proposed MPC based charging control strategy, simulation experiments are conducted based on a well established *"7 Ah Saft Lithium Ion battery"* provided in Advisor. RC model parameters and OCV all are time-variant variables depending on SoC and temperature. The curves of OCV and $R_o$ are shown in Fig. 5.6 as examples. Interpolating method is applied to create the continuous values space. The constant parameters in this simulation environment are given in Tab. 5.1.

In this work, we select the control period $T_s$ to be 30 seconds using trial and error method according to experimental results. The shorter period

Table 5.1: Simulation and experiment parameters setting.

| | Symbol | Description | Value | Unit |
|---|---|---|---|---|
| Battery (simulation) | $C$ | Battery nominal capacity | 7 | $Ah$ |
| | $m_{bat}$ | Battery mass | 0.37824 | $kg$ |
| | $C_{bat}$ | Battery heat capacity | 795 | $J/kgK$ |
| | $R_{eff}$ | Effective thermal resistance | 7.8146 | $K/W$ |
| | $T_{amb}$ | Ambient temperature | 20 | $^oC$ |
| | $\dot{m}_{air}$ | Airflow rate | 5.8333 | $g/s$ |
| | $C_{air}$ | Air heat capacity | 1009 | $J/kgK$ |
| MPC | $T_s$ | Control period | 30 | $s$ |
| | $P$ | Prediction horizon | 5 | |
| | $\omega_1$ | Weight of SoC tracking $J_1$ | 100 | |
| | $\omega_2$ | Weight of temperature rising $J_2$ | 1 | |
| GA | $MaxGen$ | Maximum generation number | 30 | |
| | $PopSize$ | Population size | 50 | - |
| | $r$ | Power of raw fitness in scaling | 2 | - |
| | $R_\lambda$ | The range of crossover coefficient | $[0.1, 0.9]$ | |
| | $P_m$ | Mutation probability | 0.2 | - |
| | $\sigma$ | Variance of Gaussian mutation | 1 | - |

Remark: The typical value of $J_1$ is around 0.08 while that of $J_2$ is around 2. Therefore, the real weight ratio of $J_1$ to $J_2$ is around 4:1.

requires the charger to change the charging current more frequently. It will increase working load to the charger and lead to more energy loss caused by switch circuits. The longer period will decrease the frequency to tune charging current in the charging process so that the performance of MPC will be limited. In addition, the long control period implies that the prediction based on the model is over a long time which essentially requires a more accurate battery model. Finally, the 30 seconds control period is long enough to allow GA to finish the optimization process.

### 5.5.2 Evaluation Method

Fast charging speed and low heat generation are both objectives in charging control. However, the two goals conflict with each other. Fast charging essentially requires large current and hence leads to high heat generation, and vice versa. From the viewpoint of multi-objective optimization, the conflicting objectives are usually evaluated by Pareto curve. For charging control, the x-axis is set as the charging duration and the y-axis as the final temperature increase $T(end)-T(0)$. As shown in Fig. 5.7, the curve with the circle marks represents the Pareto front of the CCCV family, where the CC period applies 1.5C to 6C current for fast charging. The CCCV Pareto front splits the objective space into two sections. Any charging result located in the upper right section is worse than the CCCV family for both objectives, while any result in the bottom left section is better than CCCV for both objectives. Therefore, we evaluate the performance of the charging controller according to the location of results.

### 5.5.3 Simulation Results

To facilitate comparison with the conventional CCCV family, we set the expected SoC trajectory by multiplying by 1.05. The new trajectory is intended to accelerate the charging speed. Since the working temperature of Li-ion batteries, especially for vehicular batteries, is from 20°C to 40°C, the ambient temperature is set as 20°C and the safe range of temperature is set below 40°C. The search space of the charging current is fixed from 0C to 6C.

The MPC is applied to track the modified SoC trajectories from 1.5C

to 4.5C. A faster charging speed cannot keep the rising temperature in the safe range. The Pareto front of the MPC is illustrated in Fig. 5.7 by the curve marked with stars. The results for the MPC clearly dominate those of the CCCV family. Only the result of the trajectory revised from 1.5C has a similar performance to CCCV. The reason is that a 1.5C current is comparatively so small that it limits the applicable current sequence to a small range. If the fixed search range can be accordingly reduced, e.g. from 0C to 3C, the result will be improved.

As an example, the charging processes of CCCV and MPC are compared in the case of 3C, shown in Fig. 5.8. At the beginning of charge, the internal resistance is large when the SoC is very low. In this process, the rising temperature dominates the fitness function. The optimized charging profile applies a smaller current than CCCV. However, the increase in the SoC tracking error gradually requires a higher current to speed up. Meanwhile, internal resistance is reduced significantly along with the increase in SoC. Therefore, in the middle period, the charging current for MPC is larger than for CCCV. In the final stage, the current in the CV period is decreased to prevent overvoltage of the terminal voltage. Since the trajectory of the MPC is modified from the CCCV, the same trend is retained in MPC, keeping the terminal voltage under 4V.

### 5.5.4 Experiment Results

Since the maximum charging current of the programmable electric charger is 9A, in the experiment we use a single cell with 2.3Ah to demonstrate the fast charge performance of MPC. Correspondingly, the charge resistance model

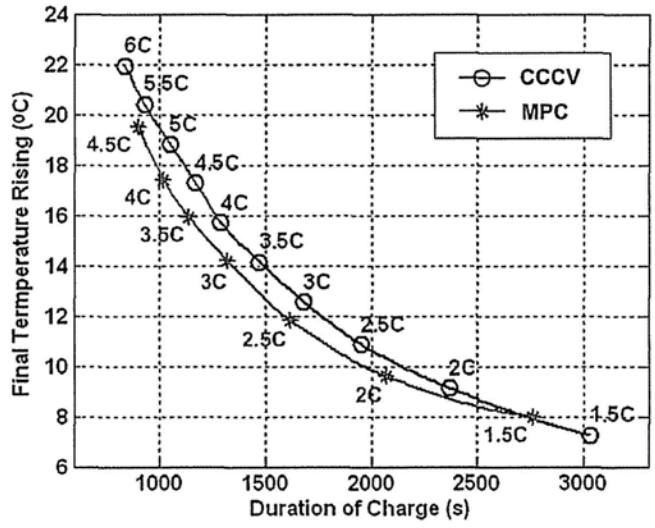


Figure 5.7: Pareto fronts of CCCV and MPC charging methods in simulation. The expected trajectories of MPC are modified from CCCV by multiplying 1.05.

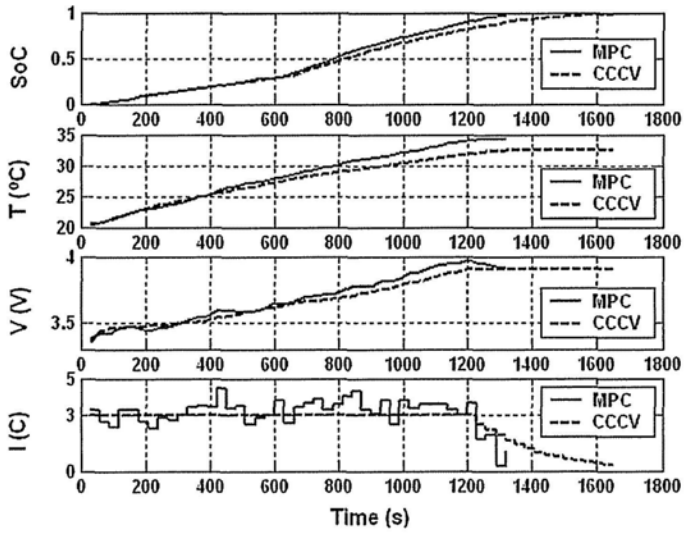


Figure 5.8: Curves during CCCV and MPC charging processes using modified 3C profile.

of a 6.9Ah cell is multiplied by three. To protect the cells, we limit the charging current to below 3C, i.e. 6.9A. The ambient temperature is 25°C. The expected SoC trajectories of MPC are 1.10 times those of the CCCV results.

Fig. 5.9 shows the Pareto-fronts of the CCCV and MPC charging results in experiments. All the results for MPC are superior to those for CCCV. Fig. 5.10 illustrates the details of the 2C charging processes. Unlike the simulation model, where the temperature is high in the lower SoC range of the specified battery type, the real LiFePO4 cell has good charging acceptance at low SoC. Therefore, a high charging current is utilized to increase the charging speed. Before reaching around 80% SoC, another high charging period occurs. This is because MPC predicts the high temperature increase beyond 80%, so it applies a high charging current at this stage and switches to a low charging current when SoC is close to 1.

## 5.6 Summery

To accelerate charging speed and reduce the temperature increase, we introduce the MPC framework to the charging control process. Given a future charging sequence, the RC model and proposed modified ESC model in Chapter 3 are applied to predict the SoC in simulation and experiment, respectively. Meanwhile, besides the single-node lumped-parameter thermal model used in simulation, we also establish a neural network to model the thermal behavior of the applied battery in the experiment. A standard genetic algorithm is applied to optimize the charging current under the multi-

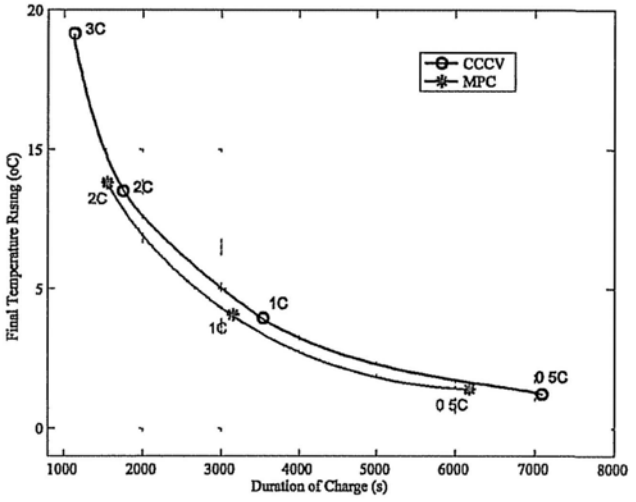


Figure 5.9 Pareto fronts of CCCV and MPC charging methods in experiments. The expected trajectories of MPC are modified from CCCV by multiplying 1.10.

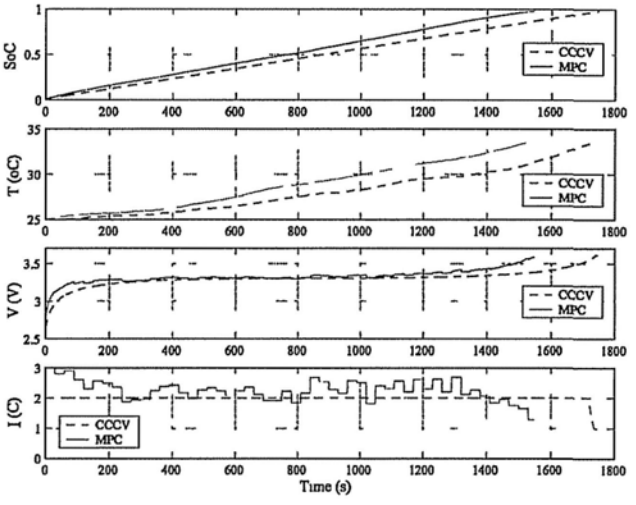


Figure 5.10 Experimental curves during CCCV and MPC charging processes using modified 2C profile.

objectives and constraints. The simulation and experimental results strongly demonstrate the availability and efficacy of MPC, with the conclusion that the Pareto front of the MPC dominates that of CCCV.

---

□ **End of chapter.**

# Chapter 6

# Conclusion

## 6.1 Contributions

- Developed a practicable BMS with the following features: (1) a self-power design to increase module independence and allow off-line self-testing and self-diagnosis; (2) selection of newly developed automobile sensors and ICs to increase the accuracy of signal measurement; (3) redistribution of tasks in module control and central control to allow the SoC estimation of each cell for Li-ion battery. The BMS has been applied and demonstrated in a series HEV and has worked steadily for several months already, successfully implementing all the designed functions and protections.

- Proposed and implemented an anti-noise SoC estimation framework to increase the availability in a real vehicle environment. This involved: (1) an adaptive-$\kappa$ nonlinear diffusion filter to denoise the measurement of current; (2) a self-learning mechanism to remove zero-drift online in

the measurement of current; (3) a modified ESC model to model the FeLiPO4 cells in experiment and application. Simulation, experiment and application results all demonstrate that the proposed estimation framework can handle the interferences in a real vehicle running environment and achieve more accurate and robust estimation results than conventional methods. Furthermore, the estimation result satisfies the requirement of the newly published development goal of China.

- Proposed and implemented a SoC based fuzzy controller to equalize cells, due to the lack of electrochemical theories and models to explain the cell equalization process. The selection of inputs consists of (1) the difference in SoC, representing the degree of imbalance, (2) the average of SoC, representing the average discharge ability, and (3) total internal resistance, partially representing the equalizing efficiency. Simulation and experimental results both show that the proposed controller has the ability to incorporate the experiences and knowledge of experts, and intelligently tune the charging current along with the instantaneous battery states to balance the multi-objectives represented by the three inputs. Especially for LiFePO4 battery, a large SoC imbalance may cause only a very small difference in voltage, causing the failure of traditional voltage based methods. Therefore, SoC based equalization is more suitable for equalizing these types of batteries.

- Proposed and implemented a fast charge framework using model predictive control, with two objectives: (1) to reduce charging duration, and (2) to reduce temperature rising. In the experiments, a neural

network was established to model the temperature increase during the charging process, and the modified ESC model was utilized to predict the future SoC given a future charging sequence. Both simulation and experimental results shows that the MPC based method can simultaneously reduce the charging duration and limit temperature increase. The Pareto front of the proposed method has been demonstrated to dominate that of the most popular CCCV method.

## 6.2 Future Works

- Electric vehicle manufacturing is a new industry in the world. The standards and test methodologies of key components as well as the whole vehicle,are currently at an immature stage. In future, the proposed BMS system should be further tested according to national and international standards, if published.

- The current design of BMS does not take the cost into consideration. In future, for commercialization purpose, the cost of BMS must be reduced.

- The performance of the proposed robust SoC estimation framework has been demonstrated in simulations, experiments and real application in this thesis. In the future, we will use theoretical analysis to demonstrate the robustness of the proposed framework, based on the statistical properties of noise, zero-drift, and model errors in a vehicle driving environment.

- Cell equalization is one of the main sources of temperature imbalance in the battery pack. In the future, we will study heat generation in the proposed equalization method and also find a way to keep the temperature field balanced.

- Experiments in fast charge are based on the programable electric charger for universal purpose. In the future, we will develop a charger for electric vehicles and integrate the proposed fast charge framework.

---

□ **End of chapter.**

# Appendix A

# Publications in Ph.D Study

## A.1 Journal

1. Jingyu Yan, Yan Lu, Jia Liu, Xinyu Wu, and Yangsheng Xu. Intelligent Diagnosis of Cardiovascular Diseases Utilizing ECG Signals. *International Journal of Information Acquisition*, 2010. (Accepted)

2. Jingyu Yan, Yan Lu, Jia Liu, Xinyu Wu, and Yangsheng Xu. Self-adaptive Model-based ECG Denoising Using Features Extracted by Mean Shift Algorithm. *Biomedical Signal Processing and Control*, Vol.5, No.2, pp.103-113, 2010.

3. Wei Chen, Jingyu Yan, Mei Chen, and Xin Li. Diversity of Pareto Front: A Multiobjective Genetic Algorithm based on Dominating Information. *Journal of Control Theory and Applications*, Vol.8, No.2, pp.222-228, 2010.

4. Jia Liu, DM Simpson, Jingyu Yan, Pandeng Zhang, and Robert Allen.

Tracking time-varying cerebral autoregulation in response to changes in respiratory PaCO2. *Physiological Measurement.* (Accepted)

## A.2 Conference

5. Jingyu Yan, Guoqing Xu, Huihuan Qian, and Yangsheng Xu. Battery Fast Charging Strategy Based on Model Predictive Control. *Vehicle Electronics Workshop, IEEE Vehicular Technology Conference*, Ottawa, Canada, 6 - 9 September, 2010. (Accepted)

6. Jingyu Yan, Zhu Cheng, Guoqing Xu, Huihuan Qian, and Yangsheng Xu. Fuzzy Control for Battery Equalization Based on State of Charge. *Vehicle Electronics Workshop, IEEE Vehicular Technology Conference*, Ottawa, Canada, 6 - 9 September, 2010. (Accepted)

7. Jingyu Yan, Huihuan Qian, Guoqing Xu, and Yangsheng Xu. Robust Estimation of Battery State-of-charge for Electric Vehicle. *IFAC Conference on Control Methodologies and Technology for Energy Efficiency*, Vilamoura, Portugal, 29 - 31 March, 2010. (Accepted)

8. Jingyu Yan, Yan Lu, Jia Liu, Xinyu Wu, and Yangsheng Xu. Model-based Feature Extraction of Electrocardiogram Using Mean Shift. *Annual International Conference of the IEEE Engineering in Medicine and Biology Society*, pp.1339-1342, Minneapolis, Minnesota, USA, 2 - 6 September, 2009.

9. Jingyu Yan, Chongguo Li, Huihuan Qian, Guoqing Xu, and Yangsheng Xu. Multi-objective Parameters Optimization of Electric Assist Con-

trol Strategy for Parallel Hybrid Electric Vehicle. *IEEE/ASME Conference on Advanced Intelligent Mechatronics*, pp.1992-1997, Singapore, 14 - 17 July, 2009.

10. Jingyu Yan, Chongguo Li, Guoqing Xu, and Yangsheng Xu. A Novel On-line Self-learning State-of-charge Estimation of Battery Management System for Hybrid Electric Vehicle. *IEEE Intelligent Vehicles Symposium*, pp.1161-1166, Xian, China, 3 - 5 June, 2009.

11. Jingyu Yan, Guoqing Xu, Yangsheng Xu, and Benliang Xie. Battery State-of-charge Estimation based on $H_\infty$ Filter for Hybrid Electric Vehicle. *International Conference on Control, Automation, Robotics and Vision*, pp.464-469, Hanoi, Vietnam, 17 - 20 December, 2008.

12. Huihuan Qian, Guoqing Xu, Jingyu Yan, Yangsheng Xu, and Kun Xu Energy Management for Four-Wheel Independent Driving Vehicle, *IEEE/RSJ International Conference on Intelligent Robots and Systems*, Taipei, Taiwan, 2010. (Accepted)

13. Huihuan Qian, Jingyu Yan, Yangsheng Xu, and Guoqing Xu. Torque Distribution for Energy Efficiency Enhancement in a 4WID Electric Vehicle. *IFAC Conference on Control Methodologies and Technology for Energy Efficiency*, Vilamoura, Portugal, 29 - 31 March, 2010. (Accepted)

14. Yan Lu, Jingyu Yan, and Yeung Yam. Model-based ECG Denoising Using Empirical Mode Decomposition. *IEEE International Conference on Bioinformatics and Biomedicine*, pp.191-196, Washington DC,

USA, Nov. 1-4, 2009.

15. Yan Lu, Jingyu Yan, and Yeung Yam. A Generalized ECG Dynamic Model with Asymmetric Gaussians and its Application in Model-Based ECG Denoising. *IEEE International Conference on Biomedical Engineering and Informatics*, pp.1-5 Tianjin, China, Oct 17-19, 2009.

16. Meng Chen, Jingyu Yan, and Yangsheng Xu. Gait Pattern Classification with Integrated Shoes. *IEEE/RSJ International Conference on Intelligent Robots and Systems*, pp.833-839, St. Louis, USA, October 11-15, 2009.

17. Chongguo Li, Jingyu Yan, Jun Cheng, Xinyu Wu, and Yangsheng Xu. Chatting Robots. *IEEE International Conference on Integration Technology*, pp.679-684, Shenzhen, China, March 20-24, 2007.

18. Niansheng Liu, Huihuan Qian, Jingyu Yan, and Yangsheng Xu. Performance Analysis of Routing Protocols for Vehicle Safety Communications on the Freeway. *International Conference on Anti-counterfeiting Security and Identification in Communication*, pp.85-88, Hong Kong, August 20-22, 2009.

---

**□ End of chapter.**

# Bibliography


[1] Sandeep Dhameja. *Electric vehicle battery systems.* Woburn: Butterworth-Heinemann, 2002.

[2] USEIA. U.S. primary energy consumption by source and sector, 2008. *http://www.eia.doe.gov/emeu/aer/pecss_diagram.html*.

[3] CC Chan. The state of the art of electric and hybrid vehicles. *Proceedings of the IEEE*, 90(2):247–275, 2002.

[4] B.E. Dickinson and D.H. Swan. EV battery pack life: pack degradation and solutions. *SAE International 951949*, pages 145–154, 1995.

[5] KT Chau. *Modern electric vehicle technology.* Oxford University Press, USA, 2001.

[6] M. Ehsani et al. *Modern electric, hybrid electric, and fuel cell vehicles: fundamentals, theory, and design.* CRC Press, 2009.

[7] ZC Wang. *Model predictive power control for hybrid electric vehicle.* PhD Thesis, The Chinese Univeristy of Hong Kong, 2008.

[8] KT Chau and YS Wong. Overview of power management in hybrid electric vehicles. *Energy Conversion and Management*, 43(15):1953–1968, 2002.

[9] CC Chan and YS Wong. Electric vehicles charge forward. *IEEE Power and Energy Magazine*, 2(6):24–33, 2004.

[10] T. Markel. Plug-in hybrid electric vehicles. In *clean cities congress and exposition, Phoenix, Arizona*, volume 7, 2006.

[11] T. Markel and A. Simpson. Plug-in hybrid electric vehicle energy storage system design. In *Proceedings of the 2006 Advanced Automotive Battery and Ultracapacitor Conference*, 2006.

[12] A. Simpson et al. *Cost-benefit analysis of plug-in hybrid electric vehicle technology.* United States. Dept. of Energy, 2006.

[13] Idaho. *FreedomCAR 42V battery test manual.* Report to U.S. Department of Energy, 2003.

[14] Idaho. *FreedomCAR battery test manual for power-assist hybrid electric vehicles.* Report to U.S. Department of Energy, 2003.

[15] Idaho. *Battery test manual for plug-in hybrid electric vehicles.* Report to U.S. Department of Energy, 2008.

[16] FV Conte. Battery and battery management for hybrid electric vehicles: a review. *Elektrotechnik und Informationstechnik*, 123(10):424–431, 2006.

[17] G.L. Plett. Extended Kalman filtering for battery management systems of LiPB-based HEV battery packs:: Part 1. Background. *Journal of Power Sources*, 134(2):252–261, 2004.

[18] K. Kitoh and H. Nemoto. 100 Wh Large size Li-ion batteries and safety tests. *Journal of Power Sources*, 81:887–890, 1999.

[19] P. Biensan et al. On safety of lithium-ion cells. *Journal of Power Sources*, 81:906–912, 1999.

[20] PG Balakrishnan et al. Safety mechanisms in lithium-ion batteries. *Journal of Power Sources*, 155(2):401–414, 2006.

[21] S. Tobishima et al. Lithium ion cell safety. *Journal of Power Sources*, 90(2):188–195, 2000.

[22] D. Aurbach et al. A short review of failure mechanisms of lithium metal and lithiated graphite anodes in liquid electrolyte solutions. *Solid State Ionics*, 148(3-4):405–416, 2002.

[23] J. Vetter et al. Ageing mechanisms in lithium-ion batteries. *Journal of Power Sources*, 147(1-2):269–281, 2005.

[24] T. Stuart et al. A modular battery management system for HEVs. In *Proceedings of the SAE Future Car Congress*, 2002.

[25] M.A. Delucchi and T.E. Lipman. An analysis of the retail and lifecycle cost of battery-powered electric vehicles. *Transportation Research Part D: Transport and Environment*, 6(6):371–404, 2001.

[26] J. Kopera. Inside the nickel metal hydride battery. *Cobasys Company Technique Article*, 2004.

[27] M.J. Klein and G.L. Plett. Advances in HEV Battery Management Systems. *Society of Automotive Engineers Conference*, 2006.

[28] G.L. Plett and M.J. Klein. Advances in HEV Battery Management Systems. In *Society of Automotive Engineers Congress*, 2006.

[29] B.P. Divakar, K.W.E. Cheng, H.J. Wu, J. Xu, H.B. Ma, W. Ting, K. Ding, W.F. Choi, B.F. Huang, and C.H. Leung. Battery management system and control strategy for hybrid and electric vehicle. In *International Conference on Power Electronics Systems and Applications*, pages 1–6, 2009.

[30] J. Chatzakis, K. Kalaitzakis, NC Voulgaris, and SN Manias. Designing a new generalized battery management system. *IEEE transactions on Industrial Electronics*, 50(5):990–999, 2003.

[31] C. Chen, J. Jin, and L. He. A new battery management system for li-ion battery packs. In *IEEE Asia Pacific Conference on Circuits and Systems*, pages 1312–1315, 2008.

[32] ADI. AD7280 datasheet. *http://www.analog.com/static/imported-files/data_sheets/AD7280.pdf*.

[33] LinearTechnology. LTC6802-1 datasheet. *http://cds.linear.com/docs/Datasheet/68021fa.pdf*.

[34] T.A. Stuart and W. Zhu. Modularized Battery Management for Large Lithium Ion Cells. *Journal of Power Sources*, in press, 2010.

[35] LEM. HTFS200-P/SP2 datasheet. *http://www.lem.com/docs/products/htfs_sp2_e.pdf*.

[36] Freescale. MC9S12XEP100 reference manual covers MC9S12XE Family. *http://www.freescale.com/files/microcontrollers/doc/data_sheet/MC9S12XEP100RMV1.pdf*, 2010.

[37] TI. TPS54160 datasheet. *http://focus.ti.com/lit/ds/symlink/tps54160.pdf*.

[38] Microchip. MCP9701A datasheet. *http://ww1.microchip.com/downloads/en/DeviceDoc/21942e.pdf*.

[39] Infineon. TLE6250 datasheet. *http://www.infineon.com/cms/en/product/findProductTypeByName.html?q=tle6250*.

[40] Onsemi. NUP2105L datasheet. *http://www.onsemi.com/pub_link/Collateral/NUP2105L-D.pdf*.

[41] Epcos. B82793 datasheet. *http://www.epcos.com/inf/30/db/emc_00/02470251.pdf*.

[42] Chenyang. CYCT04-xnM20B datasheet. *http://www.cy-sensors.com/CYCT04-xnM20B.pdf*.

[43] Onsemi. NCV33152 datasheet. *http://www.onsemi.com/pub_link/Collateral/MC34152-D.PDF*.

[44] Itech. IT8215C User Manual. *http://www.itechate.com/null/IT-DOC/IT8512C-DS-EN.PDF*.

[45] Itech. IT6154 User Manual. *http://www.itechate.com/null/IT-DOC/IT6154-DS-EN.PDF*.

[46] H. Qian, Lam T, Li W, Xia C., and Xu Y. System and design of an omni-directional vehicle. In *IEEE International Conference on Robotics and Biomimetics*, pages 389–394, 2008.

[47] H. Qian, G. Xu, J. Yan, and Xu Y. Energy management for four-wheel independent driving vehicle. In *IEEE/RSJ International Conference on Intelligent Robots and Systems*, page (Accepted), 2010.

[48] V. Pop, H.J. Bergveld, D. Danilov, P.P.L. Regtien, and P.H.L. Notten. *Battery management systems: accurate state-of-charge indication for battery powered applications.* Springer Verlag, 2008.

[49] S. Piller, M. Perrin, and A. Jossen. Methods for state-of-charge determination and their applications. *Journal of Power Sources*, 96(1):113–120, 2001.

[50] S. Rodrigues, N. Munichandraiah, and AK Shukla. A review of state-of-charge indication of batteries by means of ac impedance measurements. *Journal of Power Sources*, 87(1-2):12–20, 2000.

[51] A. Hammouche, E. Karden, and R.W. De Doncker. Monitoring state-of-charge of Ni-MH and Ni-Cd batteries using impedance spectroscopy. *Journal of Power Sources*, 127(1-2):105–111, 2004.

[52] D.T. Lee, S.J. Shiah, C.M. Lee, and Y.C. Wang. State-of-charge estimation for electric scooters by using learning mechanisms. *IEEE Transactions on Vehicular Technology*, 56(2):544–556, 2007.

[53] K.S. Ng, C.S. Moo, Y.P. Chen, and Y.C. Hsieh. Enhanced coulomb counting method for estimating state-of-charge and state-of-health of lithium-ion batteries. *Applied Energy*, 86(9):1506–1511, 2009.

[54] ZM Salameh, MA Casacca, and WA Lynch. A mathematical model for lead-acid batteries. *IEEE Transaction on Energy Conversion*, 7(1):93–98, 1992.

[55] H.J. Bergveld, W.S. Kruijt, P.H.L. Notten, and P.H.L. Notten. *Battery management systems: design by modelling*. Kluwer Academic Publishers, 2002.

[56] VH Johnson. Battery performance models in ADVISOR. *Journal of Power Sources*, 110(2):321–329, 2002.

[57] G.L. Plett. Extended Kalman filtering for battery management systems of LiPB-based HEV battery packs:: Part 2. Modeling and identification. *Journal of power sources*, 134(2):262–276, 2004.

[58] A. SZUMANOWSKI and Y. CHANG. Battery Management System Based on Battery Nonlinear Dynamics Modeling. *IEEE transactions on vehicular technology*, 57(3):1425–1432, 2008.

[59] G.L. Plett. Extended Kalman filtering for battery management systems of LiPB-based HEV battery packs-Part 3. State and parameter estimation. *Journal of Power Sources*, 134(2):277–292, 2004.

[60] J. Lee, O. Nam, and BH Cho. Li-ion battery SOC estimation method based on the reduced order extended Kalman filtering. *Journal of Power Sources*, 174(1):9–15, 2007.

[61] A. Vasebi, SMT Bathaee, and M. Partovibakhsh. Predicting state of charge of lead-acid batteries for hybrid electric vehicles by extended Kalman filter. *Energy Conversion and Management*, 49(1):75–82, 2008.

[62] J. Han, D. Kim, and M. Sunwoo. State-of-charge estimation of lead-acid batteries using an adaptive extended Kalman filter. *Journal of Power Sources*, 188(2):606–612, 2009.

[63] G.L. Plett. Sigma-point Kalman filtering for battery management systems of LiPB-based HEV battery packs:: Part 1: Introduction and state estimation. *Journal of Power Sources*, 161(2):1356–1368, 2006.

[64] G.L. Plett. Sigma-point Kalman filtering for battery management systems of LiPB-based HEV battery packs:: Part 2: Simultaneous state and parameter estimation. *Journal of Power Sources*, 161(2):1369–1384, 2006.

[65] I.S. Kim. The novel state of charge estimation method for lithium battery using sliding mode observer. *Journal of Power Sources*, 163(1):584–590, 2006.

[66] I.S. Kim. Nonlinear State of Charge Estimator for Hybrid Electric Vehicle Battery. *IEEE Transactions on Power Electronics*, 23(4):2027–2034, 2008.

[67] WX Shen, CC Chan, EWC Lo, and KT Chau. A new battery available capacity indicator for electric vehicles using neural network. *Energy Conversion and Management*, 43(6):817–826, 2002.

[68] I.H. Li, W.Y. Wang, S.F. Su, and Y.S. Lee. A merged fuzzy neural network and its applications in battery state-of-charge estimation. *IEEE Transaction on Energy Conversion*, 22(3):697–708, 2007.

[69] Y.S. Lee, W.Y. Wang, and T.Y. Kuo. Soft computing for battery state-of-charge (BSOC) estimation in battery string systems. *IEEE Transactions on Industrial Electronics*, 55(1):229–239, 2008.

[70] B. Cheng et al. State of charge estimation based on evolutionary neural network. *Energy Conversion and Management*, 49(10):2788–2794, 2008.

[71] B. Cheng, Y. Zhou, J. Zhang, J. Wang, and B. Cao. Ni-MH batteries state-of-charge prediction based on immune evolutionary network. *Energy Conversion and Management*, 2009.

[72] T. Hansen and C.J. Wang. Support vector based battery state of charge estimator. *Journal of Power Sources*, 141(2):351–358, 2005.

[73] Q.S. Shi, C.H. Zhang, and N.X. Cui. Estimation of battery state-of-charge using $\nu$-support vector regression algorithm. *International Journal of Automotive Technology*, 9(6):759–764, 2008.

[74] A. Vasebi, M. Partovibakhsh, and S. Bathaee. A novel combined battery model for state-of-charge estimation in lead-acid batteries based on

extended Kalman filter for hybrid electric vehicle applications. *Journal of Power Sources*, 174(1):30–40, 2007.

[75] J. Wang, B. Cao, Q. Chen, and F. Wang. Combined state of charge estimator for electric vehicle battery pack. *Control Engineering Practice*, 15(12):1569–1576, 2007.

[76] F. Codeca, S.M. Savaresi, and G. Rizzoni. On battery State of Charge estimation: A new mixed algorithm. In *IEEE International Conference on Control Applications*, pages 102–107, 2008.

[77] J. Qiang, G. Ao, J. He, Z. Chen, and L. Yang. An adaptive algorithm of NiMH battery state of charge estimation for hybrid electric vehicle. In *IEEE International Symposium on Industrial Electronics, 2008*, pages 1556–1561, 2008.

[78] V. Pop, HJ Bergveld, PHL Notten, JHG Op het Veld, and PPL Regtien. Accuracy analysis of the State-of-Charge and remaining runtime determination for lithium-ion batteries. *Measurement*, 42(8):1131–1138, 2009.

[79] P. Perona and J. Malik. Scale-space and edge detection using anisotropic diffusion. *IEEE Transactions on pattern analysis and machine intelligence*, 12(7):629–639, 1990.

[80] L. Birgé and P. Massart. From model selection to adaptive estimation. *Festschrift for Lucien Le Cam: Research papers in probability and statistics*, pages 55–87, 1997.

[81] K. Kutluay, Y. Cadirci, YS Ozkazanc, and I. Cadirci. A new online state-of-charge estimation and monitoring system for sealed lead-acid batteries in telecommunication power supplies. *IEEE Transactions on Industrial Electronics*, 52(5):1315–1327, 2005.

[82] B. Hassibi, A.H. Sayed, and T. Kailath. Linear estimation in Krein spaces-part I: Theory. *IEEE Transactions on Automatic Control*, 41(1):18–33, 1996.

[83] B. Hassibi, AH Sayed, and T. Kailath. Linear estimation in Krein spaces. II. Applications. *IEEE Transactions on Automatic Control*, 41(1):34–49, 1996.

[84] D. Simon. *Optimal state estimation: Kalman, $H_\infty$ and nonlinear approaches*. John Wiley and Sons, 2006.

[85] T. Markel, A. Brooker, T. Hendricks, V. Johnson, K. Kelly, B. Kramer, M. O'Keefe, S. Sprik, and K. Wipke. ADVISOR: a systems analysis tool for advanced vehicle modeling. *Journal of Power Sources*, 110(2):255–266, 2002.

[86] Investment guidance of technological upgrading and transformatioin in automotive industry. In *http://www.autoinfo.gov.cn/autoinfo_cn/xwzx/tbgz/webinfo/2010/05/1274923210160000.htm*. Ministry of Industry and Information Technology of PRC, 2010.

[87] B. Lindemark. Individual cell voltage equalizers (ICE) for reliable batteryperformance. In *International Telecommunications Energy Conference*, pages 196–201, 1991.

[88] S.W. Moore and P.J. Schneider. A review of cell equalization methods for lithium ion and lithium polymer battery systems. In *Society of Automotive Engineers*, 2001.

[89] M. Ferdowsi. Battery Charge Equalization- State of the Art and Future Trends. In *Society of Automotive Engineers*, 2005.

[90] A. Hande and TA Stuart. A selective equalizer for NiMH batteries. *Journal of Power Sources*, 138(1-2):327–339, 2004.

[91] W. Zhu, G. Landrum, and T.A. Stuart. Fast Equalization for Large Lithium Ion Batteries, 2008.

[92] Y.S. Lee, C.Y. Duh, SC Yang, and GT Chen. Battery equalization using bi-directional Cuk converter in DCVM operation. In *IEEE Power Electronics Specialists Conference*, volume 36, pages 765–771, 2005.

[93] Y.S. Lee and G.T. Cheng. Quasi-resonant zero-current-switching bidirectional converter for battery equalization applications. *IEEE Transactions on Power Electronics*, 21(5):1213–1224, 2006.

[94] Y.S. Lee, M.W. Cheng, S.C. Yang, and C.L. Hsu. Individual cell equalization for series connected lithium-ion batteries. *IEICE Transactions on Communications*, 89(9):2596–2607, 2006.

[95] M. Tang, T. Stuart, D.D.E. Co, and IN Kokomo. Selective buck-boost equalizer for series battery packs. *IEEE Transactions on Aerospace and Electronic Systems*, 36(1):201–211, 2000.

[96] H.S. Park, C.H. Kim, and G.W. Moon. Charge equalizer design method based on battery modularization. In *IEEE International Conference on Sustainable Energy Technologies*, pages 558–563, 2008.

[97] H.S. Park, C.E. Kim, C.H. Kim, G.W. Moon, and J.H. Lee. A modularized charge equalizer for an HEV lithium-Ion battery string. *IEEE Transaction on Industrial Electronics*, 56(5):1464–1476, 2009.

[98] Y.S. Lee and M.W. Cheng. Intelligent control battery equalization for series connected lithium-ion battery strings. *IEEE Transactions on Industrial Electronics*, 52(5):1297–1307, 2005.

[99] Carmelo Speltino, Domenico Di Domenico, Giovanni Fiengo, and Anna G. Stefanopoulou. Cell equalization in battery stacks through state of charge estimation polling. In *American Control Conference*, 2010.

[100] Z. Zhang and S. Cuk. A high efficiency 1.8 kW battery equalizer. In *Applied Power Electronics Conference*, pages 221–227, 1993.

[101] K.M. Passino and S. Yurkovich. *Fuzzy control*. Citeseer, 1998.

[102] RC Cope, Y. Podrazhansky, A.C. Technol, and GA Norcross. The art of battery charging. In *The 14th Annual Battery Conference on Applications and Advances*, pages 233–235, 1999.

[103] SS Zhang, K. Xu, and TR Jow. Study of the charging process of a LiCoO2-based Li-ion battery. *Journal of Power Sources*, 160(2):1349–1354, 2006.

[104] G.C. Hsieh, L.R. Chen, and K.S. Huang. Fuzzy-controlled Li-ion battery charge system with active state-of-charge controller. *IEEE Transactions on Industrial Electronics*, 48(3):585–593, 2001.

[105] YS Wong, WG Hurley, and WH Wolfle. Charge regimes for valve-regulated lead-acid batteries: Performance overview inclusive of temperature compensation. *Journal of Power Sources*, 183(2):783–791, 2008.

[106] PHL Notten, JHG Veld, and JRG Beek. Boostcharging Li-ion batteries: A challenging new charging concept. *Journal of Power Sources*, 145(1):89–94, 2005.

[107] S.Y. Park, H. Miwa, B.T. Clark, D.S.K. Ditzler, G. Malone, N.S. D'souza, and J.S. Lai. A universal battery charging algorithm for Ni-Cd, Ni-MH, SLA, and Li-Ion for wide range voltage in portable applications. In *IEEE Power Electronics Specialists Conference*, pages 4689–4694, 2008.

[108] T. Ikeya, N. Sawada, J. Murakami, K. Kobayashi, M. Hattori, N. Murotani, S. Ujiie, K. Kajiyama, H. Nasu, H. Narisoko, et al. Multi-step constant-current charging method for an electric vehicle nickel/metal hydride battery with high-energy efficiency and long cycle life. *Journal of Power Sources*, 105(1):6–12, 2002.

[109] J. Diaz, JA Martin-Ramos, AM Pernia, F. Nuno, and FF Linera. Intelligent and universal fast charger for Ni-Cd and Ni-MH batteries in portable applications. *IEEE Transactions on Industrial Electronics*, 51(4):857–863, 2004.

[110] Z. Ullah, B. Burford, and S. Dillip. Fast intelligent battery charging: neural-fuzzy approach. *IEEE Aerospace and Electronic Systems Magazine*, 11(6):26–34, 1996.

[111] A. Khosla, S. Kumar, and KK Aggarwal. Fuzzy controller for rapid nickel-cadmium batteries charger through adaptive neuro-fuzzy inference system (ANFIS) architecture. In *International Conference of the North American Fuzzy Information Processing Society*, pages 540–544, 2003.

[112] RA Aliev, RR Aliev, B. Guirimov, and K. Uyar. Dynamic data mining technique for rules extraction in a process of battery charging. *Applied Soft Computing*, 8(3):1252–1258, 2008.

[113] Y.H. Liu, J.H. Teng, and Y.C. Lin. Search for an optimal rapid charging pattern for lithium-ion batteries using ant colony system algorithm. *IEEE Transactions on Industrial Electronics*, 52(5):1328–1336, 2005.

[114] H. Saberi and FR Salmasi. Genetic optimization of charging current for lead-acid batteries in hybrid electric vehicles. In *International Conference on Electrical Machines and Systems*, pages 2028–2032, 2007.

[115] L.R. Chen, RC Hsu, and C.S. Liu. A design of a grey-predicted Li-ion battery charge system. *IEEE Transactions on Industrial Electronics*, 55(10):3692–3701, 2008.

[116] EF Camacho and C. Bordons. *Model predictive control*. Springer Verlag, 2004.

[117] S.J. Qin and T.A. Badgwell. A survey of industrial model predictive control technology. *Control engineering practice*, 11(7):733–764, 2003.

[118] A. Bemporad and M. Morari. Robust model predictive control: A survey. *Robustness in identification and control*, pages 207–226, 1999.

[119] JY Yan, Q Ling, and W Chen. Nonlinear model predictive control based on evolutionary algorithms: framework, theory and application. In A Giordano and G Costa, editors, *Soft Computing: New Research*.

[120] A.A. Pesaran. Battery thermal models for hybrid vehicle simulations. *Journal of Power Sources*, 110(2):377–382, 2002.

[121] M. Chow, S. Lukic, L Wang, and A. Govindaraj. Research repot on A123 battery modeling. *http://www.adac.ncsu.edu/res_proj/battery_model/Docs/ResearchRepotonA123BatteryModeling.ppt*.

[122] J. Yan, G. Xu, Y. Xu, and B. Xie. Battery state-of-charge estimation based on H8 filter for hybrid electric vehicle. In *International Conference on Control, Automation, Robotics and Vision*, pages 464–469, 2008.

[123] K. Deb. *Multi-objective optimization using evolutionary algorithms.* Wiley, 2001.

[124] B. Jiang and BW Wang. Parameter estimation of nonlinear system based on genetic algorithm. *Control Theory and Applications*, 17(1):150–152, 2000.

[125] D.E. Goldberg and K. Deb. A comparative analysis of selection schemes used in genetic algorithms. *Foundations of genetic algorithms*, 1:69–93, 1991.